

UNIVERSITÉ LIBRE DE BRUXELLES

FACULTÉ DES SCIENCES

DÉPARTEMENT DE PHYSIQUE

SERVICE DE PHYSIQUE DES SYSTÈMES COMPLEXES ET MÉCANIQUE STATISTIQUE

Année académique 2019-2020

Interaction-induced strain for ultracold mixtures in optical lattices

Auteur: Maxime JAMOTTE

Directeur: Nathan GOLDMAN *Co-Directeur:* Marco DI LIBERTO



MÉMOIRE PRÉSENTÉ EN VUE DE L'OBTENTION DU DIPLÔME DE
MASTER EN SCIENCES PHYSIQUES.

Remerciements

Tout d'abord, je tiens à remercier Marco Di Liberto et Nathan Goldman pour la supervision de ce mémoire, leur relecture attentive et leurs conseils. I would like to particularly thank Marco Di Liberto, with whom I worked regularly, for his kindness and patience all along this project.

Ensuite je tiens à remercier Cédric Schoonen pour la relecture de ce travail. Je le remercie également pour ces années d'amitié et pour son aide si précieuse qui a grandement contribué à ma compréhension de la physique en général.

Je remercie enfin mes parents et mes amis pour leur soutien inconditionnel qui m'a permis de m'épanouir pleinement pendant ces cinq années. Je remercie Rene Vanherk pour notre profonde amitié depuis toutes ces années.

Contents

1	Topological states and quantum simulation	10
1.1	Overview of topological matter	10
1.1.1	Topologically protected states	10
1.1.2	Quantum Hall effect	12
1.1.3	Examples of topological systems	17
1.2	Quantum simulation	20
1.2.1	Ultracold atoms	20
1.2.2	Optical lattices and Hubbard models	21
1.2.3	Gauge fields simulation	22
2	Relativistic Landau levels in strained honeycomb lattice	24
2.1	The honeycomb lattice	25
2.1.1	Honeycomb Hamiltonian in momentum space	26
2.1.2	Effective Dirac Hamiltonian	27
2.1.3	Time-reversal symmetry	29
2.1.4	Periodic boundary condition along y	30
2.2	Relativistic Landau levels	32
2.3	Pseudo gauge field in honeycomb lattices	35
2.4	Strain along x	37
2.5	Strain on other platforms	42
3	Weakly interacting Bose-Einstein condensate in optical lattice	46
3.1	Bose-Einstein condensation in continuum	46
3.1.1	The ideal Bose gas	46
3.1.2	Mean-field approximation	49
3.1.3	Weakly interacting gas and Gross-Pitaevskii equation in con- tinuum	51
3.1.4	Thomas-Fermi regime in the harmonic trap	53
3.1.5	Virial theorem and relations between the energy contributions	56
3.1.6	Depletion of the condensate by quantum fluctuations	57
3.2	Weakly interacting Bose-Einstein condensate in optical lattice	60
3.2.1	Bose-Einstein condensate on a 1D lattice	61

3.2.2	Numerical solution of Gross-Pitaevskii equation in a 1D lattice	64
3.2.3	Comparison of the imaginary-time and the self-consistent methods with analytical results	67
4	Relativistic Landau levels from a Fermi-Bose mixture	73
4.1	Numerical solution of Gross-Pitaevskii equation in a honeycomb lattice with a ribbon geometry	73
4.2	Correlated hoppings and the Landau levels	77
4.3	Landau levels away from the Thomas-Fermi regime	82
4.3.1	Presence of unstrained zones	84
4.3.2	Boundaries of the cloud and edge modes	86
5	Conclusions and perspectives	92
A	Enforcing y-periodicity	94

Résumé

L'un des principaux objectifs de la physique des atomes froids est d'exploiter l'adaptabilité de cette plate-forme pour simuler des phénomènes de matière condensée ou même explorer de nouveaux états exotiques de la matière. Les *champs de jauge* fournissent un ingrédient nécessaire de la simulation quantique, par exemple pour la réalisation de l'*effet Hall quantique entier*. Cependant, les atomes sont des objets neutres et ne se couplent pas aux champs comme le font les électrons dans les matériaux. Une approche possible pour contourner cette limitation, développée ces dernières années, est la simulation de champs de jauge *artificiels* (ou synthétiques) reposant sur l'ajout d'une phase de type Aharonov-Bohm à la fonction d'onde atomique faisant que les atomes se comportent comme s'ils étaient soumis à un champ magnétique.

Des travaux majeurs sur le graphène ont montré que les déformations de son réseau peuvent se comporter comme un champ pseudo-magnétique. En effet, lorsque les bandes d'énergie sont à moitié remplies, les électrons du graphène sont décrits par une relation de dispersion relativiste (Dirac) autour de deux points inéquivalents dans l'espace des impulsions, connus sous le nom de *vallées* ou *points de Dirac*. Certaines déformations du réseau apparaissent mathématiquement dans l'équation de Dirac comme le ferait un champ magnétique, mais dont le signe diffère en fonction de la vallée. En conséquence, chaque vallée peut donner naissance à un *effet Hall quantique de vallée* qui se manifeste par la quantification du spectre en niveaux discrets d'énergie, appelés *niveaux de Landau relativistes*.

Le but de ce mémoire est de proposer un modèle reproduisant l'effet de déformation dans les réseaux optiques afin d'observer l'effet Hall quantique de vallée. Dans le cas du graphène, il est possible de rendre dépendants de l'espace les coefficients décrivant l'effet tunnel sur son réseau. Nous commençons par passer en revue les principaux concepts des phases topologiques de la matière et des simulations quantiques dans le chapitre 1. Dans le chapitre 2, nous continuons avec l'analyse des déformations appliquées à un réseau en nous appuyant sur la littérature existante et ce, afin de calculer analytiquement et numériquement les niveaux d'énergie de Landau correspondants. À cette fin, nous avons développé des codes pour diagonaliser le hamiltonien sur un réseau en nid d'abeilles. En conséquence, nous avons reproduit plusieurs résultats de la littérature et comparés aux prévisions analytiques attendues, trouvant un excellent accord.

Dans la deuxième partie de cette thèse, nous discutons une stratégie pour implémenter la déformation de réseaux optiques avec des atomes froids. Les réseaux optiques

sont des systèmes rigides, des déformations leur sont donc difficilement applicables. Notre stratégie pour simuler la déformation consiste à utiliser un mélange d’atomes fermioniques et bosoniques, ces derniers formant un condensat de Bose-Einstein. Les deux espèces interagissent par le biais de coefficients d’effet tunnel dépendant de la densité (ou corrélés), qui peuvent être générés dans les atomes froids. En conséquence, dans l’approximation de champ moyen, une densité gradient d’une espèce obtenu à travers le piège externe se traduira par un houblonnage dépendant des autres espèces qui peuvent être exploitées pour simuler la déformation. Afin de traiter ce problème, nous abordons d’abord la physique des atomes piégés et faiblement interactifs dans le chapitre 3. En particulier, nous montrons comment résoudre numériquement l’équation de Gross-Pitaevskii, qui est le principal outil utilisé dans le régime à faible interaction, permettant de calculer la densité du condensat. Pour cela nous utilisons d’une part une méthode auto-consistante et d’autre la méthode d’évolution à temps imaginaire. Dans le chapitre 4, nous appliquons l’équation de Gross-Pitaevskii dans le cas d’un condensat sur un réseau en nid d’abeilles. Une fois calculée, la densité est utilisée pour calculer les coefficients d’effet tunnel. Près du régime de Thomas-Fermi, ceci induit la déformation linéaire du réseau. En conséquence, nous obtenons le spectre d’énergie des atomes fermioniques et les niveaux de Landau attendus. L’analyse est ensuite conclue en discutant les écarts par rapport au régime de Thomas-Fermi obtenus avec l’équation GP.

Dans le chapitre 5, nous tirons les conclusions de ce travail et discutons les perspectives possibles des simulations de déformation avec des systèmes d’atomes froids implémentant notre stratégie.

Abstract

One of the main goals of cold atom physics is to exploit the tunability of this platform to simulate condensed matter phenomena or even explore novel exotic states of matter. Gauge fields provide a necessary ingredient of quantum simulation, or for instance, in view of studying quantum Hall physics. However, atoms are neutral objects and do not couple to gauge fields as electrons in materials do. One possible approach to circumvent this limitation that has been developed in the last years is the simulation of artificial (or synthetic) gauge fields. This approach relies on engineering and externally imposing an Aharonov-Bohm-like phase on the atomic wavefunction that acts as if the atoms were subject to a magnetic field.

Pioneering works on graphene have shown that deformations of the lattice can also behave as a pseudo-magnetic field. Indeed, around half filling, the graphene electrons are described by a relativistic (Dirac) energy dispersion around two inequivalent points in momentum space, known as valleys or Dirac points. Certain

deformations of the lattice, or strain, mathematically appear in the Dirac equation as a magnetic field would, but with signs that differ on each valley. As a consequence, each valley can give rise to a quantum valley Hall effect that manifests through the quantization of the spectrum in discrete energies, known as relativistic Landau levels. The aim of this thesis is to propose a scheme to reproduce the effect of strain in optical lattices in order to observe the valley Hall effect. Strain can be described by spatially-dependent hopping coefficients for the graphene Hamiltonian in the honeycomb lattice. After reviewing the main concepts of topological phases of matter and quantum simulation in chapter 1, the thesis project starts by the analysis of strain from the published literature in order to analytically and numerically calculate the corresponding Landau energy levels in chapter 2. To this purpose, we developed codes to diagonalize the Hamiltonian matrix describing a single particle on the honeycomb lattice with different boundary conditions and strain configurations. As a result, we have reproduced several results from the literature and compared to the expected analytical predictions, finding an excellent agreement.

In the second part of this thesis we discuss the strategy to implement strain in optical lattices with cold atoms. Optical lattices are rigid systems and deformations are not easily implemented. Our strategy to simulate strain is to consider a mixture of bosonic and fermionic atoms and letting the bosons form a condensate. The two species interact through density-dependent (or correlated) hopping coefficients, which can be generated in cold-atoms by externally driving the system. As a consequence, and within a mean-field picture, a density gradient of one species obtained through the external trap will result into a spatially-dependent hopping for the other species that can be exploited to simulate strain. In order to treat this problem, we first discuss the physics of trapped and weakly interacting atoms in chapter 3. In particular we show how to numerically solve a generic Gross-Pitaevskii (GP) equation, which is the major mean-field tool employed in the weakly-interacting regime, by using a self-consistent method and the imaginary-time evolution method. In chapter 4, we apply the Gross-Pitaevskii equation to compute the density of a condensate on a honeycomb lattice. The resulting density is used by the correlated-hopping models in order to obtain the corresponding tunneling coefficients that simulate the effect of linear strain on the fermionic atoms near the Thomas-Fermi regime for the condensate. As a result, we obtain the energy spectrum of the fermionic atoms and the expected Landau levels. The analysis is then concluded by discussing the deviations from the Thomas-Fermi regime obtained with the GP equation.

In Chapter 5, we draw the conclusions of this work and we discuss the outlook and perspective of the strategy investigated in this thesis to simulate strain with cold atoms.

Chapter 1

Topological states and quantum simulation

1.1 Overview of topological matter

Topology in materials is a tool to classify different types of phases that are not described by the Landau-Ginzburg theory, which requires local order and a local order parameter. Instead, topological phases require the existence of a global order and the term *topological* is connected to the existence of a bulk invariant usually an integer or a rational number or set of numbers. In Mathematics two objects are *topologically equivalent* as long as we can continuously transform one into the other without crossing any singularity. Analogously, phases of matter have a topological nature when a deformation of the system does not modify observable quantized properties that manifest in transport measurements or in the presence of edge states and that rely on topological invariants obtained from the eigenstates of the Hamiltonian. A well-known example of topological class is the one of a sphere to which also belongs a bowl but not a doughnut since it has a hole in it. This last one is equivalent to a cup [1]. In this section we introduce a few concepts to grasp the physics of topological systems and briefly describe some of the most relevant ones.

1.1.1 Topologically protected states

An important notion for topological materials is *robustness*. This indicates that a topological phase and its properties will be unchanged if disorder or impurities are reasonably added into the system. This is understandable from the fact that the topological properties are related to discrete values of certain topological numbers or invariants. As explained in [1] suppose we take a belt and we twist it before closing it. Once it is closed the only way to untwist it is to break it which requires a large amount of energy. This indicates that to change the topological properties of a system you need to bring a sufficiently large modifications to it, whereas small

deformations of the belt will not change its topological feature defined by the number of twists that it possesses. In this sense we briefly discuss *topological phases*. Therefore topological materials can be classified in terms of their symmetry class and their dimensionality in a ‘periodic table’ by using the *Altland and Zirnbauer notation* [2]. These symmetries are: time-reversal symmetry, particle-hole symmetry and chiral symmetry.

Berry phase and Chern numbers

In order to introduce topological phases of matter in a more precise manner, let us consider a system whose spectrum is composed of several bands, each of them being separated by a gap from higher energy states. Let us take a Bloch state that is a function of parameters that depend on time. We suppose that we slowly modify these parameters in a way that the final state is the same as the initial one, i.e. we follow a closed path in the parameters space – this is the case when the parameters are sufficiently slowly varied according to the *adiabatic theorem* [1]. For example in our case these parameters are the quasi-momenta \mathbf{k} . During the evolution the state acquires not only a dynamical phase – due to the time evolution in quantum mechanics – but also a *geometrical phase* or *Berry phase* $e^{i\gamma}$ that depends on the path followed in the parameters space where

$$\gamma = \oint \mathbf{A}_n(\mathbf{k}) \cdot d\mathbf{k} \quad (1.1)$$

where $\mathbf{A}_n \equiv i\langle u_{n,\mathbf{k}} | \nabla_{\mathbf{k}} | u_{n,\mathbf{k}} \rangle$ is called the *Berry connection* of the band n . In 2D or 3D, we can take the curl (in momentum space) of the Berry connection and obtain the Berry curvature, which resembles a magnetic field in the space of parameters, $\Omega_n = \nabla_{\mathbf{k}} \times \mathbf{A}_n$. The corresponding integral over a closed manifold is quantized and this integer is called the *Chern number*, noted C_n that is

$$C_n = \frac{1}{2\pi} \iint_{BZ} \Omega_n \cdot d\mathbf{k} \quad (1.2)$$

in two dimensions. As we will see below, Chern numbers are important topological indices characterizing certain phases of matter and their transport properties. On the other side, the Berry phase itself can also be quantized and characterizes the topological nature of certain systems.

Edge states from bulk-edge correspondence

When two materials with different topological invariants, e.g. Chern numbers, are put in contact, there must exist edge states that are spatially localized at the interface [3] and that lie in the energy band gap. As a consequence, if the Fermi level of the system is set in the gap, we expect to observe the presence of edge states.

This is ensured by the *bulk-edge correspondence* [4]. In a topologically non-trivial, finite-size material, i.e. with non-zero Chern number, the physical boundary of the sample can be considered as an interface between a region with a non-zero topological invariant and the vacuum – that is topologically trivial – which guaranties the existence of localized states at the boundary of the sample. These states are the ones responsible for transport in the Quantum Hall Effect that we will discuss below.

1.1.2 Quantum Hall effect

One of the most striking examples of topological phase is provided by the Quantum Hall Effect, which was discovered by von Klitzing and collaborators [5] and that earned them the Nobel prize. In this section, we introduce the main key concepts of the classical and quantum Hall effects.

Classical Hall effect and the Drude Model

Before discussing the quantum Hall effect we introduce its classical counterpart and the concepts of conductivity and resistivity with the Drude model. When an electric field is applied at the ends of a two-dimensional conducting material, let's say in the x direction, a current density J_x , parallel to E_x , is generated. If the material is immersed in a perpendicular magnetic field, the Lorentz force

$$m \frac{d\mathbf{v}}{dt} = -e\mathbf{v} \times \mathbf{B} - e\mathbf{E} \quad (1.3)$$

bends the trajectory of its electrons. In a finite size material with adequate dimensions, this deviation causes an accumulation of negative charges on one side of the material and an accumulation of positive charges on the opposite one, inducing *Hall voltage* in orthogonally to the current I_x – see figure (1.1).

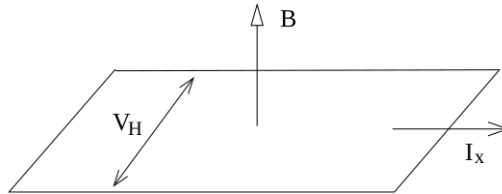


Figure 1.1: (Image from the reference [6]) Classical Hall effect.

When we add a linear friction term that encodes the effect of resistance of the material in which the electrons move, the equation of motion becomes

$$m \frac{d\mathbf{v}}{dt} = -e\mathbf{E} - e\mathbf{v} \times \mathbf{B} - \frac{m\mathbf{v}}{\tau}. \quad (1.4)$$

The coefficient τ in the friction term is called the scattering time that can be considered as the average time between two consecutive collisions of the electrons with the atoms or impurities within the material. Once an equilibrium is reached, the left hand side of (1.4) vanishes leading to

$$\mathbf{v} + \frac{e\tau}{m}\mathbf{v} \times \mathbf{B} = -\frac{e\tau}{m}\mathbf{E}. \quad (1.5)$$

Since $\mathbf{J} = -ne\mathbf{v}$ with n being the density of electrons, we rewrite the previous relation in matrix notation:

$$\begin{pmatrix} 1 & \omega_B\tau \\ -\omega_B\tau & 1 \end{pmatrix} \mathbf{J} = \frac{e^2n\tau}{m}\mathbf{E} \quad (1.6)$$

where $\omega_B = \frac{eB}{m}$ is the cyclotron frequency. Inverting this relation, we obtain the *Ohm's law*:

$$\mathbf{J} = \boldsymbol{\sigma}\mathbf{E} \quad (1.7)$$

with

$$\boldsymbol{\sigma} = \frac{\sigma_{DC}}{1 + \omega_B^2\tau^2} \begin{pmatrix} 1 & -\omega_B\tau \\ \omega_B\tau & 1 \end{pmatrix} \quad \text{with} \quad \sigma_{DC} \equiv \frac{ne^2\tau}{m} \quad (1.8)$$

called the conductivity tensor. Here σ_{DC} is the conductivity in the absence of a magnetic field. To recapitulate, applying a electric current along x gives rise to a current J_x which is deflected by the magnetic field, namely a transverse (Hall) current J_y is also generated. The off-diagonal terms in the matrix are actually responsible for the Hall effect. Indeed by putting boundaries parallel to the y -direction, the system becomes finite along y . The deflection creates an accumulation of opposite charges on one or the other boundary in function of their sign. This generates an electric field called *Hall field* which compensates the bending due to the magnetic field.

The resistivity is defined as the inverse of the conductivity:

$$\boldsymbol{\rho} = \frac{1}{\sigma_{DC}} \begin{pmatrix} 1 & \omega_B\tau \\ -\omega_B\tau & 1 \end{pmatrix}. \quad (1.9)$$

Importantly, the element $\rho_{xy} = \frac{B}{ne}$ doesn't depend on the scattering time and it is therefore independent from the imperfections of the material. If we consider a sample of the material of length L , ρ_{xy} is related to the transverse resistance R_{xy} as follows:

$$R_{xy} = \frac{V_y}{I_x} = \frac{LE_y}{LJ_x} = \frac{E_y}{J_x} = -\rho_{xy} \quad (1.10)$$

meaning it is sufficient to measure I_x and V_y . In contrast, to calculate ρ_{xx} from R_{xx} we have to take into account the appropriate lengths of the sample. We have therefore found that the Hall resistivity is independent of the details of the material but it is a more universal quantity.

Integer Quantum Hall Effect

The integer quantum Hall effect is the quantization of the Hall conductance. Actually the transverse resistivity ρ_{xy} presents a discrete character at sufficiently low temperatures when the magnetic field varies – see figure (1.2). The resistivity takes the value that only depends on the constants of nature

$$\rho_{xy} = \frac{2\pi\hbar}{e^2} \frac{1}{\nu} \quad \nu \in \mathbb{Z}. \quad (1.11)$$

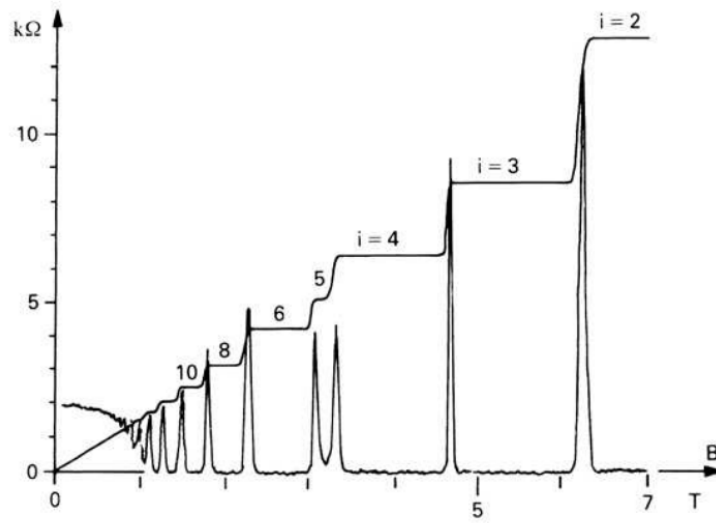


Figure 1.2: (Image from the reference [6]). Integer Quantum Hall effect exhibited by the plateaux formed by the resistivity – numbered by i – when the magnetic field B is varied.

When the magnetic field takes the value

$$B = \frac{2\pi\hbar n}{\nu e} = \frac{n}{\nu} \Phi_0 \quad (1.12)$$

the system is at the center of the ν^{th} plateau, where n is the density of electrons and $\Phi_0 = \frac{2\pi\hbar}{e}$ is known as the flux quantum [6]. The discreteness of the resistivity is related to the quantized spectrum of particles in a magnetic field, the famous Landau

Levels that we will discuss in the next section. The interesting point to notice is that the robust nature of the quantum Hall state brings a universal behaviour that does not depend on the properties of the material but only on density, charge and magnetic field. The material properties are actually crucial for something else. Namely, *disorder* in the bulk is essential to be able to distinguish an energetically broad set of localized bulk states that are responsible for the plateau behaviour of the resistivity. A clean disorder-free material cannot give the plateaus structure of the conductivity observed in the experiments, which exists thanks to the presence of these states. We can think of this in the following way. Assuming that electrons are at the correct density and completely fill a Landau Level, then if we add an electron it will occupy these localized states and therefore it will not contribute to transport. Thus the resistivity will not change. At some point the localization length of the localized states becomes larger and larger so the two edges start talking to each other – it is called *percolation* – and the electrons can start to scatter from one edge to the other. This gives a metallic behaviour and the longitudinal resistivity begins to increase, it reaches a peak as you increase the density until it gets closer to the density required for populating the next Landau level, and it happens again.

What makes systems exhibiting quantum Hall effect topologically non-trivial comes from the possibility to relate Chern numbers and conductivity. This relation is given by:

$$\sigma_{xy} = -\frac{e^2}{h} \sum_n C_n \quad C_n \in \mathbb{Z}. \quad (1.13)$$

which is called the *Thouless-Kohmoto-Nightingale-den Nijs (TKNN) formula* [7] that was rigorously derived for fermions on a 2D square lattice in a magnetic field, the well known *Hofstadter model*.

Before closing this section, it is worth mentioning that there also exists a *fractional quantum Hall effect* that emerges from materials with strong interparticle interactions. This implies the quantization of the Hall conductance at fractional values of e^2/h . Extraordinarily the excitations of the fractional quantum Hall state can have a fractional charge and fractional statistics.

Non-relativistic Landau levels

Let us take a free electron in two dimensions in a magnetic field $\mathbf{B} = \nabla \times \mathbf{A}$. Its Hamiltonian is given by

$$\hat{H} = \frac{1}{2m} (\hat{\mathbf{p}} + e\mathbf{A}(\hat{\mathbf{x}}))^2 \equiv \frac{1}{2m} \hat{\boldsymbol{\pi}}^2 \quad (1.14)$$

where we defined the mechanical momentum as $\hat{\boldsymbol{\pi}} \equiv \hat{\mathbf{p}} + e\mathbf{A}(\hat{\mathbf{x}})$. As shown in [6] the new commutation relation

$$[\hat{\pi}_x, \hat{\pi}_y] = -ie\hbar B \quad (1.15)$$

allows us to define ladder operators

$$\hat{a} = \frac{1}{\sqrt{2\hbar e B}}(\pi_x - i\pi_y) \quad \hat{a}^\dagger = \frac{1}{\sqrt{2\hbar e B}}(\pi_x + i\pi_y) \quad (1.16)$$

that satisfy $[\hat{a}, \hat{a}^\dagger] = 1$. The Hamiltonian can therefore be rewritten as

$$\hat{H} = \hbar\omega_B \left(\hat{a}^\dagger \hat{a} + \frac{1}{2} \right). \quad (1.17)$$

The spectrum of (1.17) is made of equally spaced levels called *Landau levels*:

$$E_n = \hbar\omega_B \left(n + \frac{1}{2} \right) \quad n \in \mathbb{N}. \quad (1.18)$$

The gap is proportional to the magnetic field strength. The eigenvectors $|n\rangle$, $n \in \mathbb{N}$ are constructed from the ground state $|0\rangle$ by successively applying the creation operator:

$$|n\rangle = \frac{(\hat{a}^\dagger)^n}{\sqrt{n!}} |0\rangle. \quad (1.19)$$

Depending on the chosen gauge, the eigenstates can have different forms. In this work we will pick the Landau gauge $\mathbf{A} = (0, xB, 0)$. The eigenfunctions then read

$$\psi_{n,k_y} \sim e^{ik_y y} H_n(x + k_y l_B^2) e^{-(x+k_y l_B^2)^2/2l_B^2} \quad \text{with} \quad l_B^2 \equiv \frac{\hbar}{eB} \quad (1.20)$$

where we see a dependence on the quasi-momentum k_y but none on k_x . This is because the vector potential in this gauge breaks the translational symmetry along the x direction, which prevents us to use k_x as a good quantum number. The function $H_n(x)$ is the n^{th} Hermite polynomial – that is the wavefunction associated to the n^{th} level of the harmonic oscillator.

Besides, Landau levels are macroscopically degenerate and we can easily calculate their degeneracy as follows. Classically, we know that the trajectories of a particle in a magnetic field are circles. In quantum mechanics, their center is identified by (\hat{X}, \hat{Y}) that can be written as

$$\hat{X} = \hat{x} - \frac{\hat{\pi}_y}{m\omega_B} \quad \hat{Y} = \hat{y} + \frac{\hat{\pi}_x}{m\omega_B}. \quad (1.21)$$

The operators \hat{X} and \hat{Y} don't commute since $[\hat{X}, \hat{Y}] = il_B^2$. Moreover, from uncer-

tainty principle, we find that

$$\Delta\hat{X}\Delta\hat{Y} \geq 2\pi l_B^2 \quad (1.22)$$

which is saturated when the mean value is computed on the eigenvectors (1.20) for $n = 0$ – since they are Gaussians. In this case, we interpret – heuristically – that an eigenstate occupies an area equivalent to $2\pi l_B^2$ in the 2D system of area $A = L_x L_y$ if the system consists of a rectangle of width L_x and length L_y . If we define the degeneracy \mathcal{N} as the number of states we can put onto the 2D system then we find

$$\mathcal{N} = \frac{L_x L_y}{2\pi l_B^2} = \frac{eBL_x L_y}{2\pi\hbar}. \quad (1.23)$$

Although this argument is heuristic, it turns out this result is exact [6]. In section 2.4, we will effectively observe that the degeneracy of the levels i.e. their width, increases with the size of the system and the magnetic field.

We can prove that a system whose spectrum presents Landau levels displays the quantum Hall effect. Again let us take a charged particle within a plane on which is perpendicularly applied a uniform magnetic field and an electric field along x . Its Hamiltonian is

$$\hat{H} = \frac{1}{2m} (p_x^2 + (p_y + eBx)^2) - eE_x x \quad (1.24)$$

In quantum mechanics the current in this system is

$$\mathbf{I} = -\frac{e}{m} \sum_{\substack{\text{filled} \\ \text{states}}} \langle \psi | -i\hbar\nabla + e\mathbf{A} | \psi \rangle \quad (1.25)$$

where we will assume that the filled states $|\psi\rangle$ are Landau levels (1.20). The component I_x vanishes because it's computing the momentum expectation value of harmonic oscillator eigenfunctions whereas the y component is

$$I_y = -\frac{e}{m} \sum_{n=1}^{\nu} \sum_{k_y} \left\langle \psi_{n,k_y} \left| -i\hbar \frac{\partial}{\partial y} + eBx \right| \psi_{n,k_y} \right\rangle = -e\nu \sum_{k_y} \frac{E_x}{B} = -\frac{e^2 L_x L_y \nu E_x}{2\pi\hbar}. \quad (1.26)$$

The last equality is obtained thanks to (1.23). This quantization of the resistivity (1.11) is recovered.

1.1.3 Examples of topological systems

To finish this introduction on topological matter we briefly present some relevant topological systems and their eventual symmetries. We insist a little bit more on

graphene since some of the related concepts will be peculiarly relevant for the rest of this work.

The Su-Schrieffer-Heeger (SSH) model

The SSH model, used as toy model for polyacetylene [8, 9], is the simplest 1D system that presents non-trivial topology. It consists of particles on a 1D chain with alternating hopping coefficients J and J' . This system presents a quantized *Zak phase* – the Berry phase counterpart in 1D – thanks to time-reversal, inversion and chiral symmetries. There is one phase (e.g. $J > J'$) that has no edge modes and the other phase ($J < J'$) with edge modes at zero-energy protected by chiral symmetry. In the topological transition the invariant (Zak phase) changes by π .

The Hofstadter model

The Hofstadter model consists of a 2D lattice in a uniform, perpendicular magnetic field. For specific and sufficiently large magnetic flux in each plaquette the spectrum display bands gap. For example in the square lattice with a rational p/q flux the spectrum over the Brillouin zone is composed of q bands [10] which have non-vanishing Chern number. Remarkably the spectrum acquires a fractal structure when p/q are varied between 0 and 1, known as Hofstadter’s butterfly that is shown in figure 1.3.

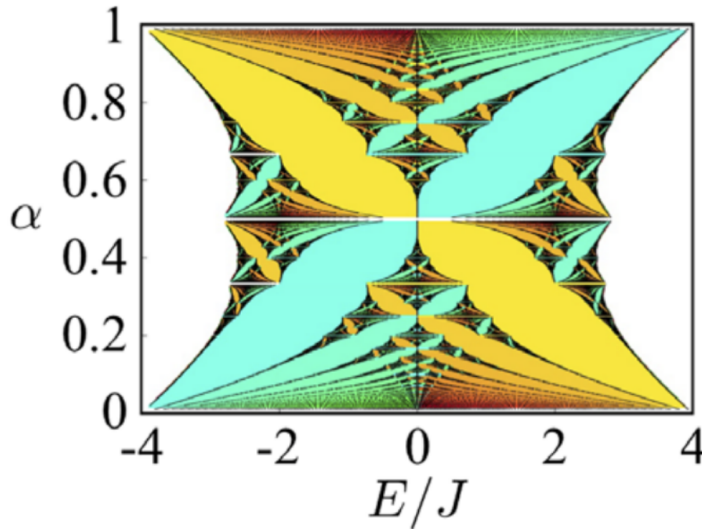


Figure 1.3: (Image from the reference [3]) Coloured Hofstadter’s butterfly. Warm colours indicate positive Chern numbers and cool colours negative. Zero Hall conductance is left blank. This represent the energy as a function of $\alpha \equiv p/q$, J is the hopping parameter of the model.

This model constitutes the lattice version of Landau levels theory which is recovered in the limit $q \gg 1$. In this sense it displays quantum Hall effect. In this system the three symmetries discussed before are broken, and in particular the breaking of time-reversal symmetry plays the crucial role for having non-zero Chern numbers.

Graphene

Graphene is an allotrope of carbon made of sp^2 -hybridized carbon atoms. Its lattice forms a 2D-honeycomb lattice. One of its interesting properties is that its low-energies excitations behave like relativistic fermions [11]. To elucidate this point, we limit ourselves to the study of a tight-binding model called *honeycomb model* where electrons hop from one site to its three nearest neighbours only. The spectrum presents a two-bands conical structure near the Fermi level $E = 0$ where conduction and valence bands touch each other which makes graphene a *semi-metal*. They touch each other at six points that delimit the first Brillouin zone. These peculiar points are called K -points or *valleys*. These are actually separated into two families of equivalent points called \mathbf{K} and \mathbf{K}' due to the presence of two sublattices. Interestingly once the dispersion relation $E(\mathbf{k})$ is expanded at first order around one of the valleys, due to the presence of two sublattices, the Hamiltonian in momentum space takes the form of a 2×2 matrix that reminds the Dirac Hamiltonian of a massless particle in two dimensions which will be demonstrated in section 2.1.2. For this reason the valleys are also called *Dirac points*. When graphene is immersed into a magnetic field the spectrum around the Dirac points display relativistic Landau level [12].

The non-trivial topology in graphene comes from the quantized Berry phase around its Dirac cones in the Brillouin zone. It is topologically protected by time-reversal symmetry and inversion symmetry. Interestingly when we consider only a 1D-ribbon of graphene with zig-zag edges the system shares many similarities to the SSH model [13]. Therefore we find the same topology: zero-energy edge states from the quantization of the Zak phase.

The Haldane model

The Haldane's Chern insulator model constitutes a topologically non-trivial insulator that does not require any magnetic field but still displays the quantum Hall effect [14]. This is due additional terms in the Hamiltonian of the honeycomb lattice: a new term that breaks time-reversal symmetry. In this case, time-reversal symmetry breaking opens a gap at the Dirac points such that a positive (or negative) Berry curvature is generated around each Dirac point and the total Chern number is then quantized to ± 1 . On the other side, an energy offset between the two inequivalent

sites, that breaks inversion-symmetry, will close the gap only around one Dirac cone causing a change of sign in the Berry curvature there. As a result, a topological transition into a regime with zero Chern number occurs.

1.2 Quantum simulation

The concept of quantum simulations is founded on the idea of mimicking a quantum system of interest with simpler and more accessible systems than classical simulations whose complexity grows exponentially with the size of the quantum system under investigation [15]. Used in various fields of science like condensed matter, high energy physics, quantum chemistry, quantum simulators serve to study simplified models where the symmetries of the simulated system are kept intact and defects are removed or controlled as much as possible.

In general a quantum simulator offers a broad tunability and controllability over the parameters of the system. In this Master's thesis we will focus on ultracold atoms though proposals suggest various ways of engineering quantum simulators as superconducting circuits, quantum dots, trapped ions, etc.

1.2.1 Ultracold atoms

From the 1970s and 1980s to the present day, theoretical and experimental quantum optics have encountered many revolutions offering an unprecedented level of *quantum engineering*, i.e. preparation, manipulation, control and detection of quantum systems made of ultracold atoms [15].

In the preparation process, the cooling is an important step for building an ultracold atom system. At low temperature, when the thermal wavelength is of the order of the spacing between particles, the laws of quantum mechanics manifest and govern the behaviour of the macroscopic world. As a result, their wave nature exhibits interfering properties and quantum superposition. For strongly interacting particles, like helium, a dissipationless liquid state is reached, and that has been dubbed superfluid state. For weakly interacting atoms, like alkali atoms, sufficiently low temperatures can lead to Bose-Einstein condensation, a state of matter where bosonic atoms occupy the same quantum state and behave as a macroscopic matter wave. Unfortunately, as a drawback it is required to reach very low temperatures, which are of the order of 1 to 100 nanokelvins. Reaching such extreme regime was made possible by the development of cooling techniques, such as laser and evaporative cooling [16], and atom trapping with laser light. The improvement of microscopy

and spectroscopic techniques [17] also played an important role to directly resolve atoms in real space.

A major ingredient in cold atoms manipulation is the *Feshbach resonance*. It consists of manipulating magnetic fields to tune the collision properties of ultracold atoms like magnitude and sign of the effective atom-atom interaction, even allowing to enter in the strongly interacting regime.

Another important tool for manipulating non-interacting ultracold gases and their dynamics is the *time-periodic driving* or *Floquet-engineering*. It consists of putting the system out of equilibrium by time-periodic perturbation, which allows for example to modify the nearest-neighbour couplings in optical lattices, making them dependent on the intensity and the frequency of the forcing. As a consequence Floquet driving has been used to manipulate the parameters of lattice models, induce phase transitions [18–20] or simulate synthetic gauge fields [21].

1.2.2 Optical lattices and Hubbard models

The advances in light-matter interaction have made possible to create optical potentials that are spatially periodic and that have been called optical lattices. In these rigid structures, which have no phonon excitations and no defects, atoms are trapped and the physics of crystal structures can be reproduced. In particular, as in condensed matter systems, the spectrum consists of energy bands and the eigenstates are Bloch functions. If the band gaps are sufficiently large and the temperature sufficiently low then only the lowest band is occupied which makes possible to work in the so-called *tight-binding approximation*. In this description, it is sufficient to consider atoms occupying highly-localized states at the bottom of each well of the lattice. As a result, only a few parameters will describe the dynamics of the atoms on the lattice and that appear in the Hubbard Hamiltonian that we briefly review here below.

Bose-Hubbard model

The Hubbard-model is originally an idealization or toy model to study magnetic properties of electrons in transition metals [15]. Since then this model has been adapted to bosonic systems in two dimensions and is called the *Bose-Hubbard model*. The Bose-Hubbard Hamiltonian reads

$$\hat{H}_{\text{BH}} = - \sum_{\langle i,j \rangle} t_{ij} \left(\hat{b}_i^\dagger \hat{b}_j + h.c. \right) + \frac{U}{2} \sum_i \hat{n}_i (\hat{n}_i - 1) - \mu \sum_i \hat{n}_i. \quad (1.27)$$

where i, j are indices of the sites of the lattice, μ is the chemical potential and \hat{b}_i^\dagger and \hat{b}_i are the creation and annihilation bosonic operators respectively and satisfy the commutation relation $[\hat{b}_i, \hat{b}_j^\dagger] = \delta_{ij}$. We will study this model in the weakly interacting limit in chapter 3. For the sake of simplicity in this introduction we will assume that tunnelling, i.e. the kinetic energy necessary for one boson to hop from site to site, is the same for all sites and directions, i.e. $t_{ij} = t$. Depending on the ratio between tunnelling and interactions, t/U , this model leads to two different quantum phases (at $T = 0$): one is the superfluid phase ($t/U \gg 1$) where the position of the particles is largely delocalized and the other one, called the *Mott-insulator phase* is characterized by a gap in the excitation spectrum and a strong localization of each particle at one site implying that any movement is energetically unfavorable. Making the number of particles fixed, a quantum phase transition at $T = 0$ can occur when each site-occupation is an integer, called the *superfluid-Mott insulator transition* and has been experimentally observed [22].

Other features can be added into the Hubbard model like terms that take into account pair hopping, next-nearest neighbours hopping and – more importantly for our purposes – *correlated* or *density-dependent hoppings* [23, 24]. These are interactions terms with the peculiarity that they explicitly depend on the density at sites between which the tunneling occurs. One approach to create density-dependent hopping coefficients exploits *Floquet engineering* that we mentioned earlier [25, 26].

In chapter 3 we treat the Bose-Hubbard model in the weakly interacting limit ($t/U \gg 1$) and add to it a harmonic trap. We will particularize to the dilute regime where a Bose-Einstein condensation takes place.

1.2.3 Gauge fields simulation

Since quantum simulators usually employ neutral particles, as atoms or photons, it has been necessary to find methods to design synthetic gauge fields in order to reproduce electromagnetic phenomena that can occur in solid-state systems. Therefore several techniques have been developed in the last decades to create *artificial* or *synthetic gauge fields* in a multitude of platforms including photonic systems, mechanical setups and ultracold atoms. In particular, gauge fields in cold atoms can be obtained by rotating atomic gases or laser dressing [27, 28] or through Floquet engineering methods [29], which have made possible to realize the Hofstadter model [30]. Floquet techniques have been in particular exploited to engineer complex hopping coefficients that are crucial for the realization of the Haldane models, both in cold atoms [31] and photonics [32].

As we will see in this thesis, the role of gauge fields can be mimicked under certain condition by applying strain on the lattice. In this respect, experiments in photonics have already shown the appearance of Landau levels under strain [33] whereas no cold atom realization of this scenario is available today. A proposal put forward in [34] relies on the modulation over space of the laser beams intensity forming the optical lattice thus displacing the minima of the optical potential and providing an effective strain on the system. The focus of this thesis will be to follow a different strategy that we will describe in the last chapter.

Chapter 2

Relativistic Landau levels in strained honeycomb lattice

In the late nineties, several groups working on electrons' motion in graphene, a 2D-allotrope of carbon with a honeycomb shape, have predicted and observed that an elastic deformation of the lattice, e.g. induced by a mechanical strain, could be interpreted as the action of a *pseudo-magnetic field* on the electrons [4]. The word *pseudo* indicates a major difference with a real magnetic field: a pseudo-magnetic field does not break time reversal symmetry whereas a real one does.

In this context this chapter has two main goals: first we provide an overview of the band structure and symmetries of the honeycomb lattice. Then we discuss the relation between strain and gauge fields, and we show the appearance of Landau levels. In particular, in the first part we discuss the features of the spectrum of a particle moving on the honeycomb lattice restraining its displacements only to its three nearest neighbours via discrete moves or *hops*, characterized by hopping coefficients. Going to momentum space we obtain the energy dispersion which is constituted of two bands as we explain in section 1.1.3. We demonstrate that the spectrum is well described by the Dirac Hamiltonian near the valleys where the two bands form a cone. Then we prove that this system preserves time-reversal symmetry. In the second part we investigate the consequences of introducing anisotropy and deformations, e.g. strain, in the system by allowing the three hopping coefficients to be different or even space-dependent. This mathematically appears in the Dirac Hamiltonian as a magnetic field would, but with signs that differ on each valley. As a major consequence, each valley can give rise to a quantum valley Hall effect, which stems from the quantization of the spectrum in discrete energies, known as *relativistic Landau levels*. These levels follow the law $E \propto \sqrt{N}$ where N is the number of the level as proven later.

Finally we briefly review strategies of generating strain on other platforms as photonics or ultracold atoms to emphasize the originality of our approach.

2.1 The honeycomb lattice

In order to construct the honeycomb lattice in two dimensions, we start with the vectors $\mathbf{a}_1 = \left(\frac{3a}{2}, \frac{\sqrt{3}a}{2}\right)$ and $\mathbf{a}_2 = \left(\frac{3a}{2}, -\frac{\sqrt{3}a}{2}\right)$ with a being the spacing parameter – see in figure (2.1) Their linear combinations form a first triangular Bravais sublattice, let's call it A . Afterwards, we add another sublattice B by putting three sites around every A site positioned at \mathbf{r}_A : $\mathbf{r}_B = \mathbf{r}_A + \boldsymbol{\delta}_j$ with $\boldsymbol{\delta}_1 = (-a, 0)$, $\boldsymbol{\delta}_2 = \left(\frac{a}{2}, \frac{\sqrt{3}a}{2}\right)$, and $\boldsymbol{\delta}_3 = \left(\frac{a}{2}, -\frac{\sqrt{3}a}{2}\right)$.

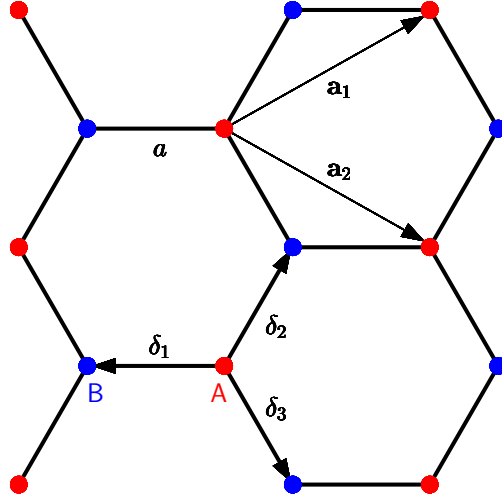


Figure 2.1: Portion of a honeycomb lattice. The vectors \mathbf{a}_1 and \mathbf{a}_2 generate the triangular Bravais sublattice composed of the A sites and the vectors $\boldsymbol{\delta}_j$ ($j = 1, 2, 3$) place the B sites.

Let us consider particles on the honeycomb lattice – we do not specify whether they are bosons or fermions. We will assume that their movement on this lattice is restricted to hopping between nearest neighboring sites. Moreover, assuming the particles do not interact with each other, the tight-binding, one-body Hamiltonian in the second quantisation picture reads¹

¹In this chapter we take the hopping matrix element t as our unit of energy.

$$\hat{H} = \sum_{\langle ij \rangle} t_{ij} \hat{a}_i^\dagger \hat{b}_j + H.c. = \sum_{\mathbf{r}, j} \left(t_j \hat{a}_{\mathbf{r}}^\dagger \hat{b}_{\mathbf{r}+\boldsymbol{\delta}_j} + H.c. \right) \quad (2.1)$$

where $\hat{a}_{\mathbf{r}} = \hat{a}(l, m)$, $\hat{a}_{\mathbf{r}}^\dagger = \hat{a}^\dagger(l, m)$ are the annihilation and creation operators of a particle at a site A at position $\mathbf{r} = l\mathbf{a}_1 + m\mathbf{a}_2$ (same for $b_{\mathbf{r}+\boldsymbol{\delta}_j}, b_{\mathbf{r}+\boldsymbol{\delta}_j}^\dagger$ at position $\mathbf{r} + \boldsymbol{\delta}_j$). The three hopping parameters t_j ($j = 1, 2, 3$) describe the cost in energy to tunnel from an A to a B site and vice-versa. The index j recalls the direction of tunnelling along the $\boldsymbol{\delta}_j$.

2.1.1 Honeycomb Hamiltonian in momentum space

Starting from (2.1), we impose periodic boundary conditions in both x and y directions. We then move to the quasi-momentum space by applying a Fourier transform on the operators \hat{a} and \hat{b} that are rewritten

$$\begin{aligned} \hat{a}(l, m) &= \frac{1}{N_s} \sum_{k_x \in BZ} \sum_{k_y \in BZ} \hat{a}_{\mathbf{k}} e^{i(l\mathbf{k} \cdot \mathbf{a}_1 + m\mathbf{k} \cdot \mathbf{a}_2)} \\ \hat{b}(l, m) &= \frac{1}{N_s} \sum_{k_x \in BZ} \sum_{k_y \in BZ} \hat{b}_{\mathbf{k}} e^{i(l\mathbf{k} \cdot \mathbf{a}_1 + m\mathbf{k} \cdot \mathbf{a}_2)} e^{i\mathbf{k} \cdot \boldsymbol{\delta}_1}, \end{aligned} \quad (2.2)$$

where the integrals run over the first Brillouin zone and N_s is the number of unit cells. The extra phase factor $e^{i\mathbf{k} \cdot \boldsymbol{\delta}_1}$ is for taking into account the inter unit-cell distance between A and B sites. Substituting (2.2) into (2.1) gives us $\hat{H} = \frac{1}{N_s} \sum_{\mathbf{k}} \hat{H}(\mathbf{k}) d\mathbf{k}$ where

$$\hat{H}(\mathbf{k}) = \hat{b}_{\mathbf{k}}^\dagger \hat{a}_{\mathbf{k}} (t_1 e^{-i\mathbf{k} \cdot \boldsymbol{\delta}_1} + t_2 e^{-i\mathbf{k} \cdot \boldsymbol{\delta}_2} + t_3 e^{-i\mathbf{k} \cdot \boldsymbol{\delta}_3}) + \hat{a}_{\mathbf{k}}^\dagger \hat{b}_{\mathbf{k}} (t_1 e^{i\mathbf{k} \cdot \boldsymbol{\delta}_1} + t_2 e^{i\mathbf{k} \cdot \boldsymbol{\delta}_2} + t_3 e^{i\mathbf{k} \cdot \boldsymbol{\delta}_3}). \quad (2.3)$$

that can be put in a matrix form:

$$\hat{H}(\mathbf{k}) = \begin{pmatrix} \hat{a}_{\mathbf{k}}^\dagger & \hat{b}_{\mathbf{k}}^\dagger \end{pmatrix} \begin{pmatrix} 0 & V^*(\mathbf{k}) \\ V(\mathbf{k}) & 0 \end{pmatrix} \begin{pmatrix} \hat{a}_{\mathbf{k}} \\ \hat{b}_{\mathbf{k}} \end{pmatrix} \equiv \begin{pmatrix} \hat{a}_{\mathbf{k}}^\dagger & \hat{b}_{\mathbf{k}}^\dagger \end{pmatrix} h(\mathbf{k}) \begin{pmatrix} \hat{a}_{\mathbf{k}} \\ \hat{b}_{\mathbf{k}} \end{pmatrix} \quad (2.4)$$

The off-diagonal element is

$$V(\mathbf{k}) = t_1 e^{i\mathbf{k} \cdot \boldsymbol{\delta}_1} + t_2 e^{i\mathbf{k} \cdot \boldsymbol{\delta}_2} + t_3 e^{i\mathbf{k} \cdot \boldsymbol{\delta}_3}. \quad (2.5)$$

By diagonalizing $h(\mathbf{k})$ we obtain the dispersion relation $E(\mathbf{k})$. This energy dispersion is constituted of two bands. If $t_1 = t_2 = t_3 = t$ these two bands have the following

analytical expression:

$$E = \pm t \sqrt{3 + 4 \cos\left(\frac{3k_x a}{2}\right) \cos\left(\frac{\sqrt{3}k_y a}{2}\right) + 2 \cos(\sqrt{3}k_y a)} \quad (2.6)$$

as shown in figure 2.2. These two bands touch each other at the Fermi level $E = 0$ in six points called *Dirac points* that correspond to the \mathbf{K} and \mathbf{K}' points which are the corners of the hexagonal Brillouin zone.

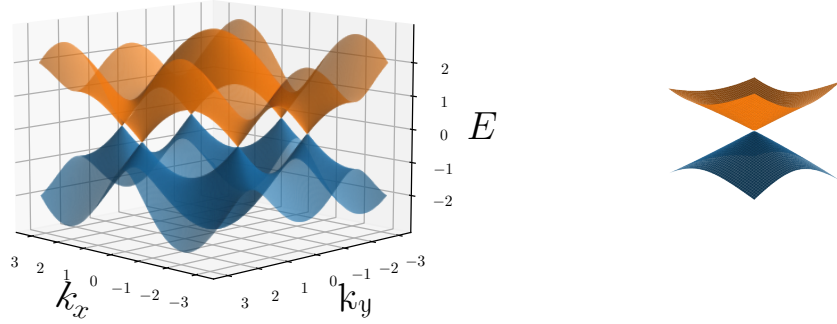


Figure 2.2: Left: Electronic dispersion in the honeycomb lattice for a fully periodic system. Right: Zoom on the Dirac point $\mathbf{K}' = (0, 4\pi/3\sqrt{3}a)$ to show a Dirac cone.

2.1.2 Effective Dirac Hamiltonian

There are two nonequivalent Dirac points denoted \mathbf{K} and \mathbf{K}' around which we can expand $V(\mathbf{k})$ given in (2.5). Around \mathbf{K} we find at first order in $\mathbf{q}a = (\mathbf{k} - \mathbf{K})a$:

$$\begin{aligned} V(\mathbf{k}) &= V(\mathbf{K}) + \left(\frac{\partial V(\mathbf{k})}{\partial \mathbf{k}} \right)_{\mathbf{k}=\mathbf{K}} \cdot \mathbf{q} + \mathcal{O}(\mathbf{q}^2) \\ &= \sum_j t_j e^{i\mathbf{K} \cdot \boldsymbol{\delta}_j} + i \sum_j t_j e^{i\mathbf{K} \cdot \boldsymbol{\delta}_j} \boldsymbol{\delta}_j \cdot \mathbf{q} + \mathcal{O}(\mathbf{q}^2) \\ &= \sum_j t_j e^{i\mathbf{K} \cdot \boldsymbol{\delta}_j} [1 + i \boldsymbol{\delta}_j \cdot \mathbf{q}] + \mathcal{O}(\mathbf{q}^2) \end{aligned} \quad (2.7)$$

for $\|\mathbf{q}\|a \ll 1$. If $t_1 = t_2 = t_3$, the Bloch Hamiltonian $h(\mathbf{k})$ can be written as

$$h(\mathbf{q}, \mathbf{K}) = \begin{pmatrix} 0 & i\hbar v_D(q_x - iq_y) \\ -i\hbar v_D(q_x + iq_y) & 0 \end{pmatrix} = \hbar v_D(q_y \sigma_x - q_x \sigma_y) \quad (2.8)$$

with $v_D \equiv 3a/2\hbar$ and σ_x, σ_y are Pauli matrices. Around \mathbf{K}' the relation (2.8) becomes

$$h(\mathbf{q}, \mathbf{K}') = \hbar v_D(-q_y \sigma_x - q_x \sigma_y). \quad (2.9)$$

The relations (2.8) and (2.9) can be recombined into

$$h(\mathbf{q}, \xi \mathbf{K}) = \hbar v_D(\xi q_y \sigma_x - q_x \sigma_y). \quad (2.10)$$

by introducing the coefficient ξ that represents the *valley pseudospin* where $\xi = +1$ and $\xi = -1$ stand for \mathbf{K} and \mathbf{K}' respectively. By applying the change of basis

$$\begin{pmatrix} \psi_A \\ \psi_B \end{pmatrix} \rightarrow \begin{pmatrix} -i & 0 \\ 0 & 1 \end{pmatrix} \begin{pmatrix} \psi_A \\ \psi_B \end{pmatrix} = \begin{pmatrix} -i\psi_A \\ \psi_B \end{pmatrix} \quad (2.11)$$

we arrive at

$$h(\mathbf{q}, \xi \mathbf{K}) \rightarrow \bar{h}(\mathbf{q}, \xi \mathbf{K}) \equiv \begin{pmatrix} i & 0 \\ 0 & 1 \end{pmatrix} h(\mathbf{q}, \xi \mathbf{K}) \begin{pmatrix} -i & 0 \\ 0 & 1 \end{pmatrix} = -\hbar v_D(q_x \sigma_x + \xi q_y \sigma_y). \quad (2.12)$$

We can assemble $h(\mathbf{q}, \mathbf{K})$ and $h(\mathbf{q}, \mathbf{K}')$ into a four-spinor representation

$$\bar{\mathcal{H}}(\mathbf{q}, \mathbf{K}, \mathbf{K}') = h(\mathbf{q}, \mathbf{K}) \oplus h(\mathbf{q}, \mathbf{K}') = \begin{pmatrix} -\hbar v_D(q_x \sigma_x + q_y \sigma_y) & 0 \\ 0 & -\hbar v_D(q_x \sigma_x - q_y \sigma_y) \end{pmatrix} \quad (2.13)$$

where the spinors are

$$\Psi_{\mathbf{q}} = \left(\psi_{\mathbf{q},+}^A, \psi_{\mathbf{q},+}^B, \psi_{\mathbf{q},-}^A, \psi_{\mathbf{q},-}^B \right)^T. \quad (2.14)$$

To make it look more like pseudospin-matrix we apply on left and right the matrix

$$\Gamma_y = \begin{pmatrix} 1 & 0 \\ 0 & \sigma_y \end{pmatrix} \quad (2.15)$$

which changes the sign in front of the real part of the matrix element and as in reference [35] we finally get²

²The Pauli matrix σ_z is noted τ_z in order to distinguish the two types of pseudospins in play here. The matrices σ_x and σ_y represent the *sublattice pseudospin*, where ‘orbital up’ corresponds to the component on the A sublattice and ‘orbital down’ to that on the B one. For its part, the matrix τ_z describes the *valley pseudospin* which is due to the twofold valley degeneracy.

$$\mathcal{H}(\mathbf{q}, \mathbf{K}, \mathbf{K}') = \Gamma_y \bar{\mathcal{H}}(\mathbf{q}, \mathbf{K}, \mathbf{K}') \Gamma_y = -\hbar v_D \tau_z \otimes \mathbf{q} \cdot \boldsymbol{\sigma} \quad \text{with} \quad \tau_z \otimes \boldsymbol{\sigma} = \begin{pmatrix} \boldsymbol{\sigma} & 0 \\ 0 & -\boldsymbol{\sigma} \end{pmatrix}. \quad (2.16)$$

The eigenvalues of \mathcal{H} are linear in momentum as

$$E_\lambda = \lambda \hbar v_D \sqrt{q_x^2 + q_y^2} = \lambda v_D q \quad (\lambda = \pm). \quad (2.17)$$

reminding us the spectrum of a relativistic, massless particle. Added to the fact we made this matrix looks like a Hamiltonian of a 1/2-spin system we see the possible parallel with the Dirac Hamiltonian. In this sense we can talk about *effective Dirac Hamiltonian*.

2.1.3 Time-reversal symmetry

The time-reversal (TR) as stated by its name changes the arrow of time. As such, it leaves the position operator unchanged but flips the sign of momentum and of angular momentum. Since in our problem we have no spin thus the TR operator is simply the complex-conjugation operator [36]. Indeed, by looking at its action on the commutator of $\hat{\mathbf{r}}$ and $\hat{\mathbf{p}}$

$$T[\hat{\mathbf{x}}, \hat{\mathbf{p}}]T^{-1} = Ti\hbar T^{-1} = -[\hat{\mathbf{x}}, \hat{\mathbf{p}}] = -i\hbar \quad (2.18)$$

then $TiT^{-1} = -i$. Since the Hamiltonian (2.1) satisfies $THT^{-1} = H$ thus our system respects the TR-symmetry. Besides we find that $V(\mathbf{k})^* = V(-\mathbf{k})$ then we find for the Bloch Hamiltonian (2.4) that

$$Th(\mathbf{k})T^{-1} = h(\mathbf{k})^*, \quad (2.19)$$

where it is easy to see that $h(-\mathbf{k}) = h(\mathbf{k})^*$. This implies

$$h(\mathbf{q}, \mathbf{K})^* = \hbar v_D (q_y \sigma_x + q_x \sigma_y) = h(-\mathbf{q}, -\mathbf{K}). \quad (2.20)$$

As a result the TR-symmetry helps us to predict the form of the Bloch Hamiltonian around \mathbf{K}' from its form around \mathbf{K} . Indeed since $\mathbf{K}' = -\mathbf{K}$ modulo a reciprocal lattice vector, we obtain

$$h(-\mathbf{q}, -\mathbf{K}) = h(-\mathbf{q}, \mathbf{K}') = \hbar v_D (q_y \sigma_x - q_x \sigma_y). \quad (2.21)$$

Therefore we can recover the equation (2.9) by simply using time-reversal symmetry. Finally we find³:

³Of course the reasoning here holds entirely for $h(\mathbf{k})$ that is linearized around \mathbf{K} and \mathbf{K}' and not

$$h(\mathbf{q}, \xi \mathbf{K})^* = -h(\mathbf{q}, \xi \mathbf{K}'). \quad (2.22)$$

The relation (2.22) also holds if we start from (2.12):

$$\bar{h}(\mathbf{q}, \xi \mathbf{K})^* = -\hbar v_D (q_x \sigma_x - \xi q_y \sigma_y) = \hbar v_D (-\xi q_x \sigma_x + q_y \sigma_y) = -\bar{h}(\mathbf{q}, \xi \mathbf{K}') \quad (2.23)$$

Having this in mind we are now able to find how to express the TR operator acting on the spinor-representation. We know that TR on a system with spin can be represented by a rotation by π around some arbitrary axis added to the complex conjugate operation. By convention we choose the rotation to be around y -axis. For half-integer spin $\mathbf{S} = \frac{\hbar}{2} \boldsymbol{\sigma}$, the TR operator is then described by

$$T = e^{-i\pi\sigma_y/2} C = \left[\cos\left(\frac{\pi}{2}\right) I + \sin\left(\frac{\pi}{2}\right) \begin{pmatrix} 0 & -1 \\ 1 & 0 \end{pmatrix} \right] C = -i\sigma_y C \quad (2.24)$$

where C is the complex conjugation operator⁴ and I is the 2×2 identity matrix. To apply it on the 4×4 matrix we simply place two matrices T as block-diagonal elements: $\mathcal{T} = T \otimes I = -i\sigma_y C \otimes I \equiv -i\Sigma_y \mathcal{C}$. We then find:

$$\begin{aligned} \mathcal{T} \mathcal{H}(\mathbf{q}, \mathbf{K}, \mathbf{K}') \mathcal{T}^{-1} &= -i\Sigma_y \mathcal{C} \mathcal{H}(\mathbf{K}, \mathbf{K}') \mathcal{C} i\Sigma_y \\ &= \Sigma_y \mathcal{H}(\mathbf{q}, \mathbf{K}, \mathbf{K}')^* \mathcal{C} \Sigma_y \\ &= -\Sigma_y \hbar v_D \begin{pmatrix} q_x \sigma_x - q_y \sigma_y & 0 \\ 0 & -q_x \sigma_x + q_y \sigma_y \end{pmatrix} \Sigma_y \\ &= -\hbar v_D \begin{pmatrix} -\mathbf{q} \cdot \boldsymbol{\sigma} & 0 \\ 0 & \mathbf{q} \cdot \boldsymbol{\sigma} \end{pmatrix} \\ &= \mathcal{H}(\mathbf{q}, \mathbf{K}', \mathbf{K}) \quad (= -\mathcal{H}(\mathbf{q}, \mathbf{K}, \mathbf{K}')) \end{aligned} \quad (2.25)$$

where Σ_y flipped the sign of the real part of the elements of \mathcal{H} . We observe that under TR, \mathbf{K} becomes $\mathbf{K}' (= -\mathbf{K})$ and vice versa. By comparing with what is said in [36] we conclude that the Dirac points behave like the spin under TR: $\mathbf{S} \rightarrow -\mathbf{S}$.

2.1.4 Periodic boundary condition along y

If we remove the periodicity along x the honeycomb lattice on the figure 2.1 becomes the one on the figure 2.3 where we colored the link in function of the hopping parameter they represent: the blue lines stand for t_2 while the green ones

for the one in (2.4)

⁴Note that $CiC = -i$.

represent t_3 . We also note the dashed lines symbolizing the periodicity along y . We are then facing a $N_x \times 2$ lattice. Importantly we must mention the type of edges chosen on the left and right edges: in our case they are both *zig-zag*. This configuration among a few others presents edge modes as explained in [36] and [37]. This feature will play an important role in the last part of this thesis.

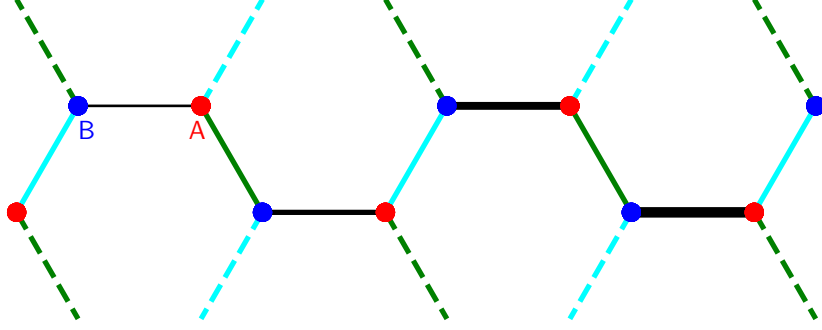


Figure 2.3: Ribbon of honeycomb lattice with imposed periodicity along the y -axis. The dashed lines symbolise the periodic condition along y . The blue lines represent $t_2 e^{ik_y \delta_{2,y}}$ while the green ones represent $t_3 e^{ik_y \delta_{3,y}}$ and the black ones the link t_1 . The thickness of the black lines symbolizes the linear strain applied on the lattice that increases with x – see section 2.4.

By starting from (2.1) and following the development⁵ in [37] we obtain:

$$\hat{H} = \bigoplus_{k_y \in BZ} H(k_y) \quad \text{where}$$

$$H(k_y) = \begin{pmatrix} \ddots & & \ddots & & \\ & 0 & 2t \cos(\sqrt{3}k_y/2) & & \\ 2t \cos(\sqrt{3}k_y/2) & & 0 & t_1 & \\ & & t_1 & 0 & 2t \cos(\sqrt{3}k_y/2) \\ & & & 2t \cos(\sqrt{3}k_y/2) & 0 \\ & & & \ddots & \ddots \end{pmatrix} \quad (2.26)$$

if $t_2 = t_3 = t$ while t_1 is an arbitrary constant. The crystal momentum or quasimomentum k_y takes values in the first Brillouin zone, i.e. $k_y \in [-4\pi/3\sqrt{3}a, 4\pi/3\sqrt{3}a]$.

⁵The details of the computations to obtain the matrix (2.26) are presented in Appendix A

We implemented an algorithm that simply consists of computing the energies in function of k_y and allows to plot an eigenvector in function of x for a chosen couple (k_y, E) . The spectrum is presented on the figure 2.4 where we distinguish the four Dirac cones as expected from the figure 2.2. We also plot eigenvectors corresponding to $(k_y a = 2\pi/3\sqrt{3}a, E \simeq 0.04t)$ (orange cross) and to $(k_y a = 1.3a, E = 0)$ (blue cross) as shown on the figure 2.5. The two curves correspond to the occupation of the A and B sublattices. The left subfigure shows the wavefunction of a particle in a box. The right subfigure shows eigenfunctions localized on the edges as we discussed earlier. We will see what happens when $t_1 \neq t_2 \neq t_3$ but are still constant. Note that for sufficiently large differences between t_1, t_2 and t_3 the Dirac points move towards each other. When $t_1 = 2t_2 = t_3 = 2t$, two inequivalent valleys merge into one as shown in figure 2.6. We also observe that when $t_1 > 2t$, a gap appears [37]. This feature is known as a Lifshitz transition.

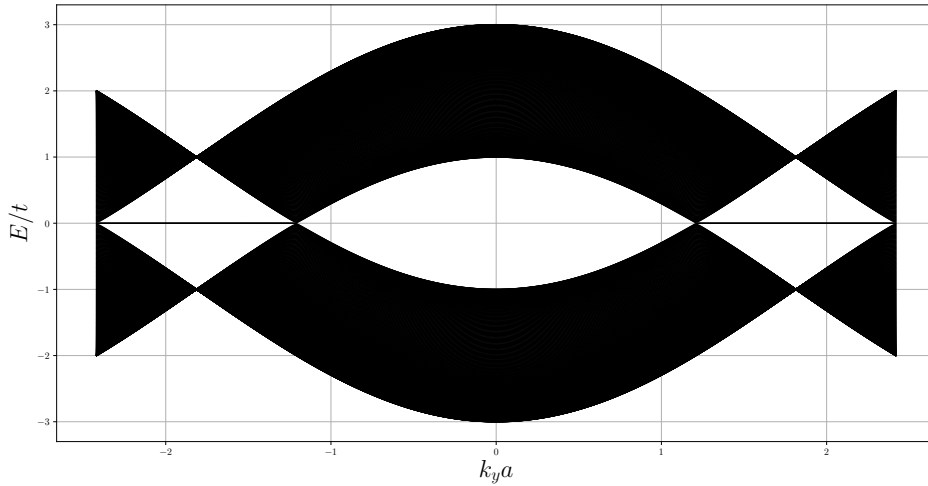


Figure 2.4: Spectrum of the honeycomb lattice with imposed periodicity along the y -axis for $t_1 = t_2 = t_3 = t$ and $N_x = 241$. We distinguish the four Dirac cones. This figure is in agreement with what can be found in the reference [36].

2.2 Relativistic Landau levels

Differently from the non-relativistic case, we discuss here the problem of a massless relativistic fermion with charge e that lives in a 2D space in presence of a perpendicular magnetic field [35]. The Hamiltonian for this particle is the Dirac Hamiltonian

$$\hat{H} = v_D \boldsymbol{\sigma} \cdot (\hat{\mathbf{p}} + e\mathbf{A}(\hat{\mathbf{x}})) \equiv v_D \boldsymbol{\sigma} \cdot \hat{\boldsymbol{\Pi}} \quad (2.27)$$

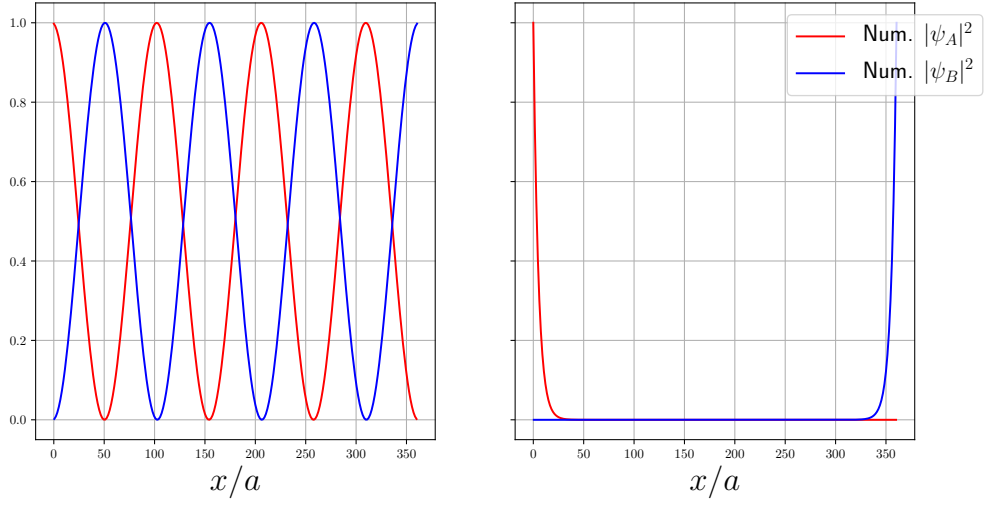
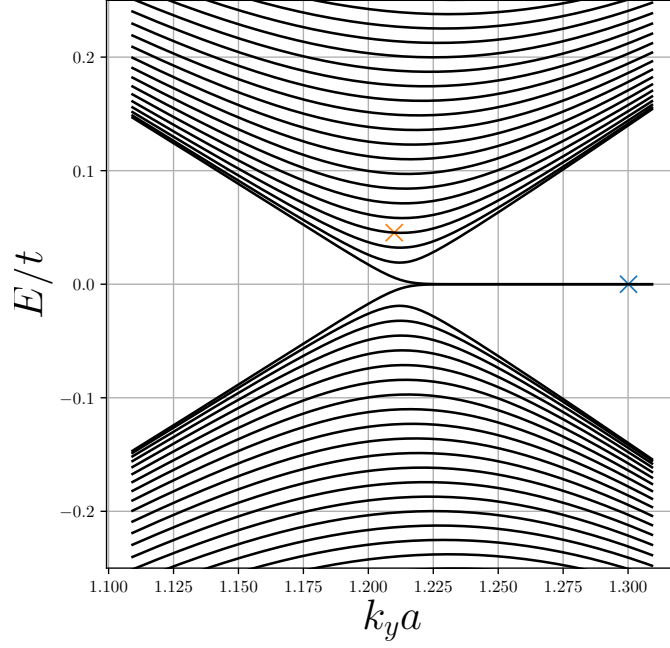


Figure 2.5: Zoom on a Dirac cone (top). The orange cross corresponds to the eigenvectors plotted to the left and the blue one to the eigenvectors to the right. These last ones are localized on the edges.

expressed in terms of the Pauli matrices. When we pass to the ladder operators

$$\hat{a} = \frac{l_B}{\sqrt{2\hbar}}(\hat{\Pi}_x - i\hat{\Pi}_y) \quad \hat{a}^\dagger = \frac{l_B}{\sqrt{2\hbar}}(\hat{\Pi}_x + i\hat{\Pi}_y) \quad \text{with} \quad [\hat{a}, \hat{a}^\dagger] = 1 \quad (2.28)$$

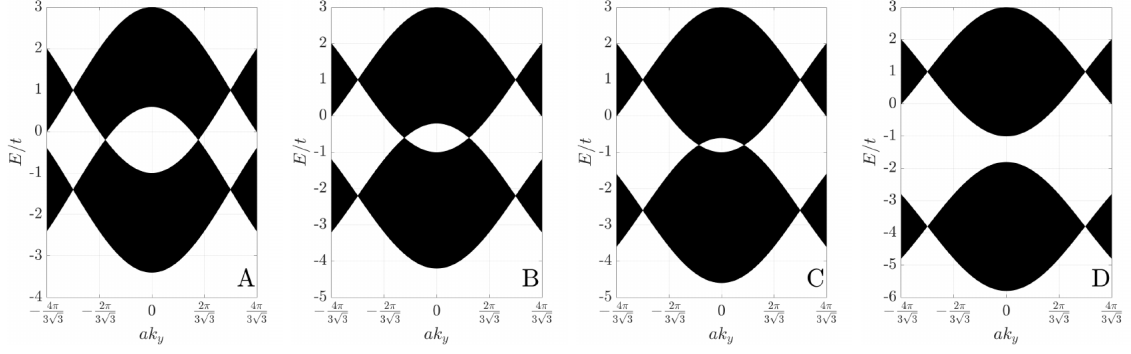


Figure 2.6: (Image from the reference [37]) Energy bands for different values of the ratio t_1/t . From left to right: $t_1/t = 1.2, 1.6, 1.8, 2.4$. Note the movement of two inequivalent Dirac points towards each other.

where $l_B^2 = \hbar/|eB|$, the Hamiltonian (2.27) becomes

$$\hat{H} = \frac{\sqrt{2}v_D}{l_B} \begin{pmatrix} 0 & \hat{a} \\ \hat{a}^\dagger & 0 \end{pmatrix}. \quad (2.29)$$

To diagonalize this Hamiltonian we consider the eigenvalue problem

$$\hat{H} \begin{pmatrix} \phi_A \\ \phi_B \end{pmatrix} = \epsilon \begin{pmatrix} \phi_A \\ \phi_B \end{pmatrix}. \quad (2.30)$$

By applying a second time H , we obtain

$$\begin{aligned} 2 \left(\frac{v_D}{l_B} \right)^2 \hat{a} \hat{a}^\dagger \phi_A &= \epsilon^2 \phi_A \\ 2 \left(\frac{v_D}{l_B} \right)^2 \hat{a}^\dagger \hat{a} \phi_B &= \epsilon^2 \phi_B \end{aligned} \quad (2.31)$$

where $\hat{N} = \hat{a}^\dagger \hat{a}$ whose eigenvalues are $N \in \mathbb{N}$. Therefore the eigenvalues of \hat{H} are given by

$$\epsilon_N = \pm \frac{\hbar v_D}{l_B} \sqrt{2N} = \pm v_D \sqrt{2|eB|N} \quad N \in \mathbb{N} \quad (2.32)$$

where the $+$ and $-$ signs correspond to the conduction and valence bands respectively. Both positive and negative states can be labeled by an integer $0 < N < \infty$. The spectrum displays a level structure. Compared to its non-relativistic counterpart, the energy levels are not equally spaced anymore. The corresponding eigenvectors are:

$$\psi_{\pm|n|}(x, y) = e^{iq_y y} \begin{pmatrix} \phi_A(x) \\ \phi_B(x) \end{pmatrix} = e^{iq_y y} \begin{pmatrix} \pm \langle x || n | - 1 \rangle \\ \langle x || n | \rangle \end{pmatrix} \quad (2.33)$$

where

$$\langle x|n\rangle \propto e^{-(x-x_0)^2/2\ell_B^2} H_n((x-x_0)/\ell_B) \quad \text{for } n \geq 0. \quad (2.34)$$

The degeneracy of the levels is calculated in the same way as for non-relativistic Landau levels – see (1.23).

2.3 Pseudo gauge field in honeycomb lattices

If we choose completely general hopping parameters ($t_1 \neq t_2 \neq t_3$) something interesting appears from (2.7). Following reference [37] we first expand around $\mathbf{K} = (0, -4\pi/3\sqrt{3}a)$:

$$\begin{aligned} V(\mathbf{q} + \mathbf{K}) = & q_x \left[\frac{\sqrt{3}a}{4}(t_2 - t_3) - i\frac{a}{4}(4t_1 + t_2 + t_3) \right] + q_y \left[\frac{3a}{4}(t_2 + t_3) - i\frac{\sqrt{3}a}{4}(t_2 - t_3) \right] \\ & + \frac{1}{2}(2t_1 - t_2 - t_3) - i\frac{\sqrt{3}}{2}(t_2 - t_3) + \mathcal{O}((qa)^2) \end{aligned} \quad (2.35)$$

Introducing

$$\begin{aligned} v_D^x &= \frac{a}{4\hbar}(4t_1 + t_2 + t_3) + i\frac{\sqrt{3}a}{4\hbar}(t_2 - t_3) \\ v_D^y &= \frac{3a}{4\hbar}(t_2 + t_3) - i\frac{\sqrt{3}a}{4\hbar}(t_2 - t_3) \\ v_D^x eA_x &= \frac{\sqrt{3}}{2}(t_2 - t_3) \\ v_D^y eA_y &= \frac{1}{2}(2t_1 - t_2 - t_3). \end{aligned} \quad (2.36)$$

we find

$$V(\mathbf{q} + \mathbf{K}) = -iv_D^x(\hbar q_x + eA_x) + v_D^y(\hbar q_y + eA_y) \quad (2.37)$$

thus the Hamiltonian reads

$$h(\mathbf{q}, \mathbf{K}, \mathbf{A}) = -v_D^x(\hbar q_x + eA_x)\sigma_y + v_D^y(\hbar q_y + eA_y)\sigma_x. \quad (2.38)$$

Putting the Bloch Hamiltonian into this form highlights the existence of a pseudo

gauge field \mathbf{A} due to anisotropy. Around $\mathbf{K}' = (0, 4\pi/3\sqrt{3}a)$ we get

$$V(\mathbf{q} + \mathbf{K}') = q_x \left[-\frac{\sqrt{3}a}{4}(t_2 - t_3) - i\frac{a}{4}(4t_1 + t_2 + t_3) \right] + q_y \left[-\frac{3a}{4}(t_2 + t_3) - i\frac{\sqrt{3}a}{4}(t_2 - t_3) \right] \\ + \frac{1}{2}(2t_1 - t_2 - t_3) + i\frac{\sqrt{3}}{2}(t_2 - t_3) + \mathcal{O}((qa)^2). \quad (2.39)$$

which gives

$$h(\mathbf{q}, \mathbf{K}', (-A_x, A_y)) = -(v_D^x)^*(\hbar q_x - eA_x)\sigma_y - (v_D^y)^*(\hbar q_y + eA_y)\sigma_x. \quad (2.40)$$

At this point, it is important to notice that the previous results shows that anisotropic hopping manifests as a gauge field for the valleys \mathbf{K} and \mathbf{K}' , despite the fact that no actual gauge field has been applied. Moreover, if the artificial vector potential \mathbf{A} is made space dependent, e.g. by making the hopping coefficients space dependent as we will see in the next section we obtain the effective Dirac Hamiltonian of a relativistic particle in a valley-dependent magnetic field $\mathbf{B} = \nabla \times \mathbf{A}$.

By repeating the change of basis (2.11) and assembling $h(\mathbf{q}, \mathbf{K}, \mathbf{A})$ and $h(\mathbf{q}, \mathbf{K}', \mathbf{A})$ into a 4×4 matrix we find

$$\bar{\mathcal{H}}(\mathbf{q}, \mathbf{K}, \mathbf{K}', \mathbf{A}) = \begin{pmatrix} -(v_D^x\sigma_x, v_D^y\sigma_y) \cdot (\hbar\mathbf{q} + e\mathbf{A}) & 0 \\ 0 & -(v_D^x)^*(\hbar q_x - eA_x)\sigma_x + (v_D^y)^*(\hbar q_y + eA_y)\sigma_y \end{pmatrix} \quad (2.41)$$

Applying again Γ_y to the left and right will modify only $h(\mathbf{q}, \mathbf{K}', \mathbf{A})$ by changing the signs in front of the real part of the elements of the matrix. Then $V(\mathbf{q} + \mathbf{K}')$ becomes

$$V(\mathbf{q} + \mathbf{K}') \rightarrow q_x \left[\frac{\sqrt{3}a}{4}(t_2 - t_3) - i\frac{a}{4}(4t_1 + t_2 + t_3) \right] + q_y \left[\frac{3a}{4}(t_2 + t_3) - i\frac{\sqrt{3}a}{4}(t_2 - t_3) \right] \\ - \frac{1}{2}(2t_1 - t_2 - t_3) + i\frac{\sqrt{3}}{2}(t_2 - t_3) + \mathcal{O}((qa)^2). \quad (2.42)$$

which is similar to $V(\mathbf{q} + \mathbf{K})$ except for the last two terms that have opposite sign. These terms actually correspond to the terms $v_D^x eA_x$ and $v_D^y eA_y$. From this we can

rewrite the relations (2.36):

$$\begin{aligned}
v_D^x &= \frac{a}{4\hbar}(4t_1 + t_2 + t_3) + i\frac{\sqrt{3}a}{4\hbar}(t_2 - t_3) \\
v_D^y &= \frac{3a}{4\hbar}(t_2 + t_3) - i\frac{\sqrt{3}a}{4\hbar}(t_2 - t_3) \\
v_D^x eA_x &= \frac{\sqrt{3}}{2}\xi(t_2 - t_3) \\
v_D^y eA_y &= \frac{1}{2}\xi(2t_1 - t_2 - t_3).
\end{aligned} \tag{2.43}$$

Finally we find

$$\mathcal{H}(\mathbf{q}, \mathbf{K}, \mathbf{K}', \mathbf{A}) = \begin{pmatrix} h(\mathbf{q}, \mathbf{K}, \mathbf{A}) & 0 \\ 0 & h(\mathbf{q}, \mathbf{K}', -\mathbf{A}) \end{pmatrix} \tag{2.44}$$

where the vector potential is now explicitly valley-dependent. Consequently the pseudo-magnetic field is also valley-dependent (positive for the valley \mathbf{K} and negative for the valley \mathbf{K}'). This is not what would happen for a spinful particle in a magnetic field. Indeed from the beginning the TR symmetry has not been broken. Therefore \mathbf{B} is not behaving as a magnetic field and the valleys are not behaving as spins. In other words, if we had true magnetic field and spins, both valleys would see the same sign of magnetic field but that would break time-reversal symmetry, which is not the case here.

Besides, the presence of the pseudo-vector potential has two other consequences. The first one is the displacement of the Dirac cones. Indeed the presence of this \mathbf{A} is a results from unequal hopping parameters and as we stated in the section 2.1.4 it inevitably leads to the movement of the Dirac cones towards each other. The second important consequence of the pseudo-magnetic field is the appearance of relativistic Landau Levels on each valley, as we will see below.

2.4 Strain along x

The goal of this section is to numerically compute a pseudo-Landau levels spectrum. For comparison and make clear the directions we are heading to, we present in figure 2.7 the spectrum of a honeycomb lattice on which a real magnetic field is applied. Landau levels are clearly visible. Following reference [38] and the discussion of the previous section, we know that it is possible to generate Landau levels physics by applying strain on an honeycomb lattice. To implement strain only along x we choose to make the hopping parameter t_1 space-dependent as follows:

$$t_1(x) = t \left[1 + \frac{\tau}{3a} \left(x - \frac{L_x}{2} \right) \right] \quad x \in A \text{ sublattice}, \quad (2.45)$$

which is centered in the middle of the system of length L_x . The coefficient τ represents the intensity of the strain applied on the lattice. The hopping t_1 is set in the middle to be $t_1 = t$. Physically, the hopping should all have the same sign at all positions along x therefore we require the condition $t_1(-L_x/2) \geq 0$ at one edge which imposes an upper bound on the strain:

$$\frac{\tau L_x}{6a} < 1. \quad (2.46)$$

This condition automatically implies that $t_1(L_x/2) \leq 2t$ at the other edge which guarantees that no local Lifshitz transition to a gapped state takes place in the considered ribbon. By taking $t_2 = t_3 = t$ we remark that the periodicity along y is conserved but not the one along x . Therefore the repeated part of the lattice forms a ribbon composed of $N_x \times 2$ sites – see figure 2.3 where the hopping parameter increases with x as in (2.45) – as symbolized by the thickness of the black lines.

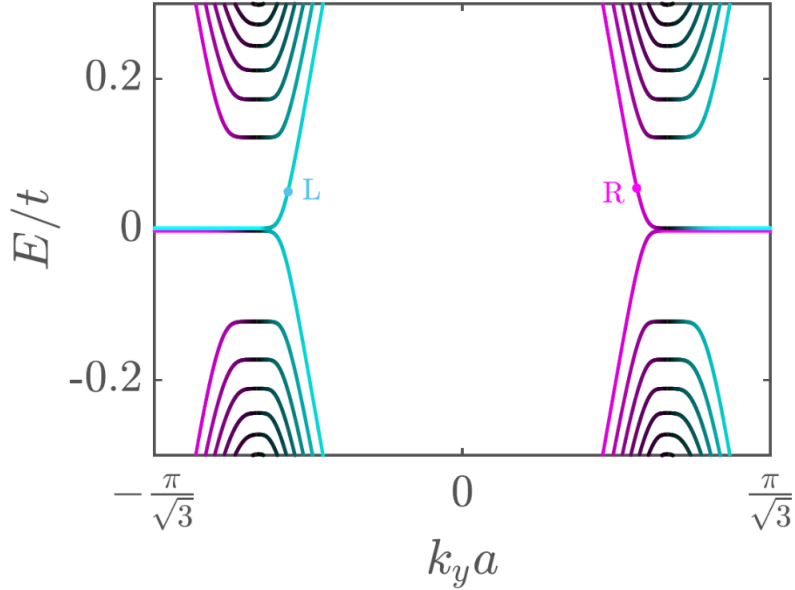


Figure 2.7: (Picture from reference [39]) Spectrum of an honeycomb lattice in a real magnetic field with periodic boundary conditions along y . This specific spectrum corresponds to a system with $N_x = 99$ sites in a magnetic field $|B| = 30$ T for parameters of solid state graphene.

Thanks to what we derived and discussed about the analytical resemblance between the Dirac Hamiltonian and the honeycomb lattice near its Dirac points, in

sections 2.2 and 2.1.2, we are able to predict at which energy we should find the Landau levels. The expressions 2.43 give in our case

$$\begin{aligned} v_D^x &= v_D + \frac{\tau t x}{3\hbar} & v_D^y &= \frac{3at}{2\hbar} \\ A_x &= 0 & A_y &= \xi \frac{2\hbar}{9ea^2} \tau x. \end{aligned} \quad (2.47)$$

The velocity is space-dependent but we may neglect the term in v_D^x that is proportional to τ as long as $\tau x \ll v_D \hbar / t, \forall x$. This condition turns out to be in accordance with (2.46) and it helps us to predict for which values of τ the Landau levels can be observed in function of the size of the system. When τ is sufficiently small such that we can neglect the dependence of the velocity on the position, the effective Hamiltonian – around the Dirac points – describes a relativistic particle in a magnetic field

$$\mathbf{B} = \nabla \times \mathbf{A} = \xi \frac{2\hbar}{9ea^2} \tau \hat{\mathbf{z}}. \quad (2.48)$$

and as we have seen in section 2.2 its energy spectrum is

$$E_N = \pm t \sqrt{N\tau} \quad N \in \mathbb{N}. \quad (2.49)$$

Nevertheless we have to remember that the vector potential that is proportional to τ translates the Dirac cones. If τ becomes too large the Dirac cones will merge and the analysis based on relativistic Landau levels is not applicable anymore. The spectrum for the entire strained lattice is shown in figure 2.8 for $N_x = 241$ and $\tau = 0.005$. We also represent with red dashed lines the Landau levels (2.49). We later explain the presence of the green lines. On the figure 2.9 we plot the eigenvectors at $E = v_D \sqrt{2\hbar|eB|}$ ($N = 1$) and $E = v_D \sqrt{4\hbar|eB|}$ ($N = 2$) both with $k_y = 2\pi/3\sqrt{3}a$.

The first remark relative to the figures 2.8 and 2.9 is that they are in perfect agreement with the ones obtained in the references [38] and [39] respectively. On the spectrum we notice that the crossings between the numerical spectrum (in black) and the true Landau levels (in red) are at the middle of the levels. This ensures at least that exactly at the Dirac point there is no difference between applying a real magnetic field on the honeycomb lattice from straining it. Moreover we observe a good fitting of the numerical eigenvectors with the analytical ones, the little disagreements at the right peaks is due to the anisotropy induced by strain which increases the magnitude of the hopping in the right side of the lattice and we start observing deviations from a perturbative regime. Indeed when we decrease τ – not enough to completely destroy the Landau levels – the magnetic length increases and the eigenfunctions extends over a larger number of sites implying that the

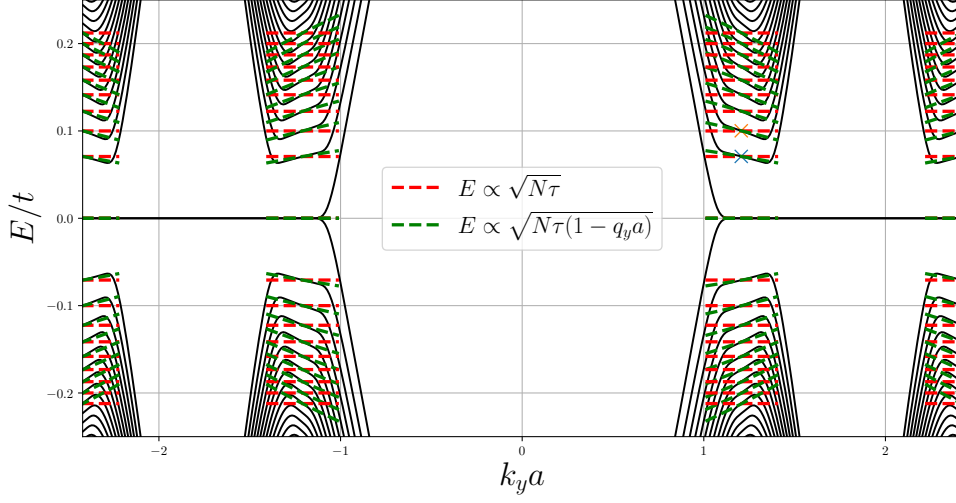


Figure 2.8: Spectrum (black lines) of strained honeycomb lattice in the x -direction with periodic boundary conditions along y . This specific spectrum corresponds to a system with $N_x = 241$ sites and $\tau = 0.005$. The red and green lines represent respectively the Landau levels (2.49) and (2.50). The crosses indicates to which points of the spectrum correspond the eigenfunctions plotted in figure 2.9. This spectrum is in accordance with [38].

function is more localized around the Dirac point thus the numerical eigenfunctions get a better agreement with the Landau levels eigenfunctions. Note that by flipping the sign in front of τ the disagreement goes to the left peak, as expected.

For now let us focus on the slope of the pseudo-Landau levels. As done in [38] reintroducing the τ -term in v_D^x will add a dependency of the energy on q_y as follows:

$$E_N = \pm t \sqrt{N\tau} \sqrt{1 - q_y a}. \quad (2.50)$$

We plotted the corrected pseudo-Landau levels on the figure 2.8 in dashed green lines. We see that they better fit the spectrum than the real Landau levels (red lines). The accuracy could be improved yet by expanding (2.5) to higher orders on $q_y a \ll 1$.

Here below we investigate which parameters should be tuned to broaden the Landau levels. This is relevant for experimental observations of Landau levels since more states would be available to reveal them. From section 1.1.2 we know that the increase of the system's size and of the intensity of the magnetic field enlarge the Landau levels. This is due to the degeneracy of the eigenvalue which is proportional to the magnetic flux through the lattice. Inspired by this analysis we vary N_x and

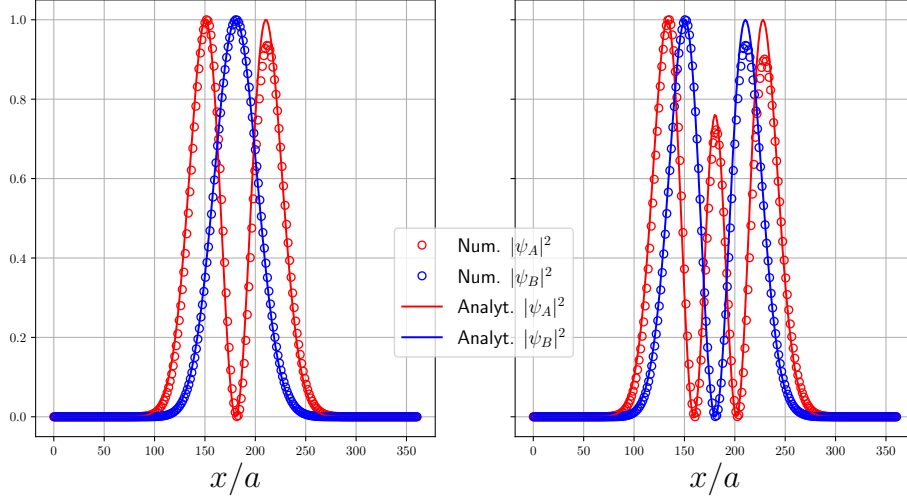


Figure 2.9: Comparison between the eigenvectors of a spin-1/2 relativistic particle in a magnetic field (solid line) – see (2.29) – and the eigenvectors of a strained honeycomb lattice (circles) at the Dirac point $(2\pi/3a, 2\pi/3\sqrt{3}a)$ for $N = 1$ (left) and $N = 2$ (right). The results are in accordance with [39].

τ (to which the pseudo-magnetic field is proportional) and present the results on figure 2.10. We conclude that increasing both τ and N_x broadens the levels as we expected. Although we know that τ cannot grow arbitrarily in order not to reach the Lifshitz transition, we also understand that keeping τ small will flatten the levels.

In conclusion, we have shown that each valley displays a separate quantum Hall effect where the magnetic field changes sign for each valley. For this reason, this phenomenon is called *valley quantum Hall effect*. Anyway we still expect to observe edge states for energies that lie in the gaps between the levels, as we explained in section 1.1.2. Importantly we need to remember that in figure 2.5 we showed that the ribbon naturally possesses edge states for zig-zag terminations – see section 1.1.3. It will be important to distinguish the different origin of edge states in the last part of this work.

With the help of figure 2.11 we show the mean position of the eigenstates and we notice several features. There are indeed edge states coming from the topological properties brought by the Landau levels physics. For example in figure 2.11 thanks to the colour map we observe that the eigenstate corresponding to the Landau levels (blue diagonal lines) evolve into edge states when bending to higher energies (red vertical lines). We emphasize that we are able to effectively identify its origin to the Landau levels since it did not exist when no strain was applied. To support

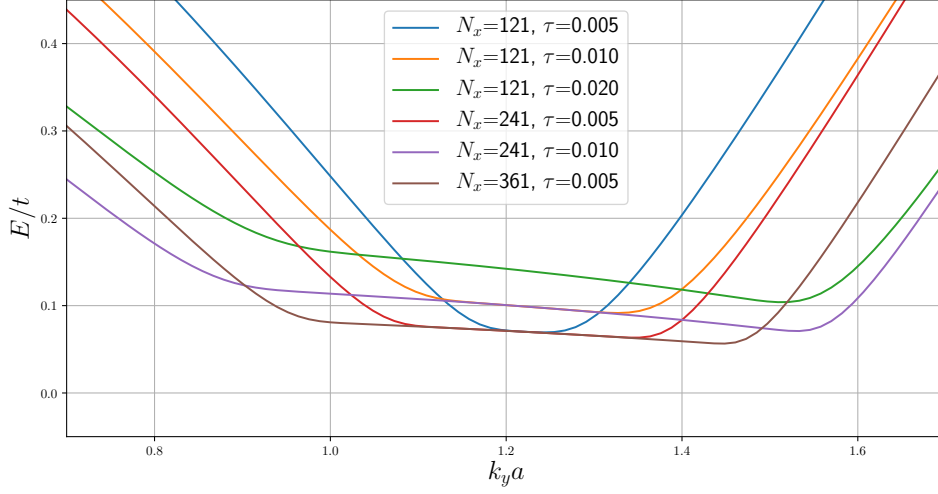


Figure 2.10: Comparison of the width and length of pseudo-Landau levels for various values of N_x and τ .

this claim we also show the colour-mapped, unstrained honeycomb spectrum in figure 2.12 where only the zero-energy level correspond to edge states. Secondly the alternation of colours on the zero-energy level indicates that the 0th Landau level is degenerate with the zig-zag edge states of the honeycomb lattice.

We make a final a remark concerning a possible hybridization between the 0th Landau level and the zero-energy level of the honeycomb system. By looking at the colour of the spectrum in the upper inset near the Dirac point – around $k_y a = 1.21$ – we see that where we would expect to see a bulk state apparently sits a state neither localized at the edge nor in the middle of the system. Indicated in the same inset by the blue cross, we present in figure 2.13 the associated eigenstate. We neatly remark the ambivalence of its localization. Its part corresponding to the A sublattice is concentrated in the middle of the system whereas its B sublattice-part is completely localized at the right edge. Another important clue is the double degeneracy of $E = 0$ visible in the lower inset of the figure 2.11 that is not present in the lower inset of figure 2.12.

2.5 Strain on other platforms

Suitable designs of the strain have been engineered such that experimentalists could generate large and constant pseudo-magnetic fields. In the experiment from the group of Rechtsman [33] in photonics artificial strain is realized by shifting the waveguides in space and thus creating a space dependent coupling between them that simulates trigonal strain, creating an artificial pseudo-magnetic field for the

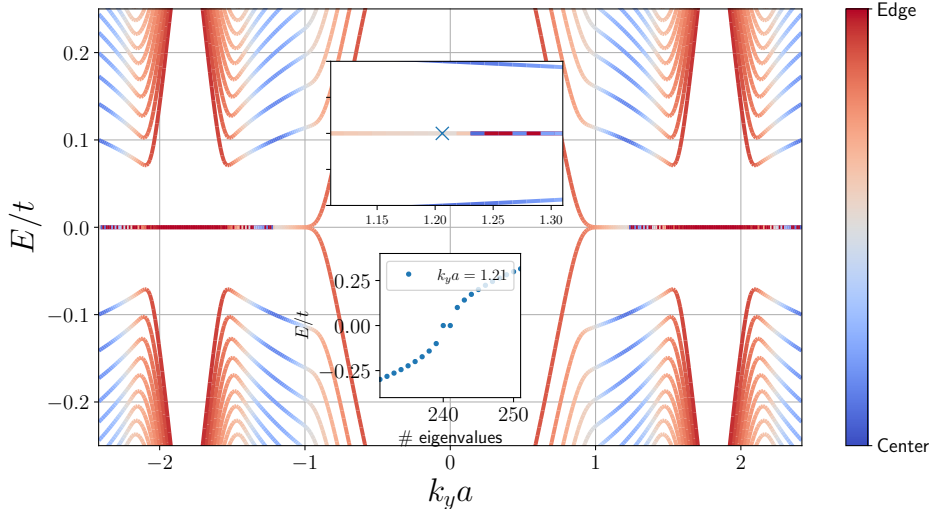


Figure 2.11: Spectrum of honeycomb lattice for $N_x = 241$, $\tau = 0.01$ with periodic boundary conditions along y . The colours indicate where is the mean position of the each eigenstates with respect to the center of the system. The blue cross in the upper inset correspond to the eigenvector plotted in figure 2.13. The lower inset shows the double degeneracy of the level $E = 0$.

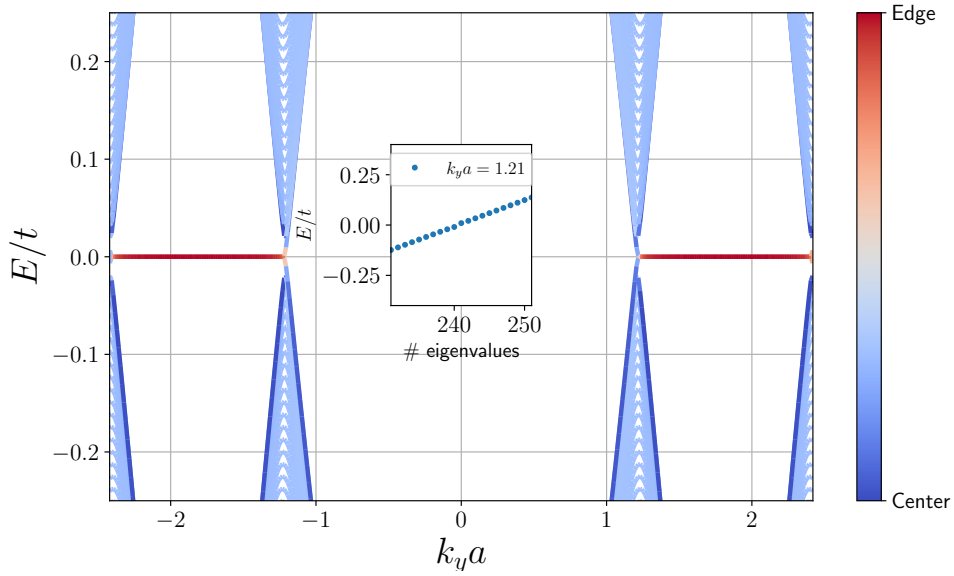


Figure 2.12: Spectrum of honeycomb lattice for $N_x = 241$, $\tau = 0$ with periodic boundary conditions along y . The colours indicate where is the mean position of each eigenstates with respect to the center of the system.

photons.

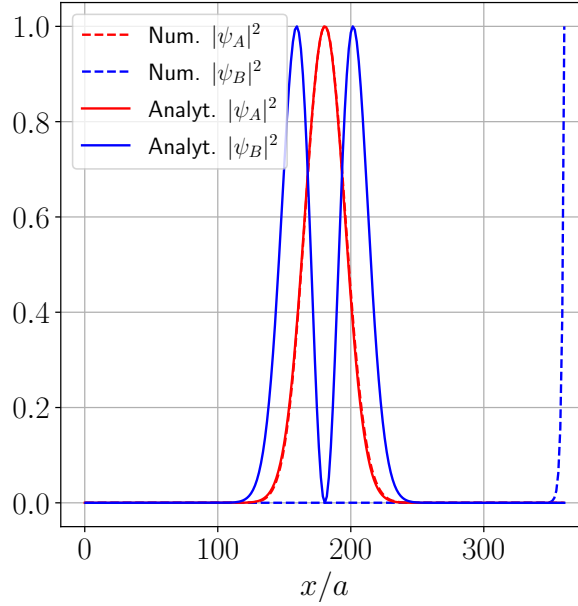


Figure 2.13: Comparison between the eigenvectors of a spin-1/2 relativistic particle in a magnetic field (solid line) – see (2.29) – and the eigenvectors of a strained honeycomb lattice (dashed lines) at $k_y a = 1.23$ (left) and at $k_y a = 1.38$ (right) for $N = 0$. It shows the presence of both Landau level and edge state (naturally present for zig-zag honeycomb) at the 0th level.

For cold atoms, a proposal to generate strain and simulate a valley-dependent synthetic magnetic field has been presented in [34] for a honeycomb optical lattice. They proposed an experimental setup to show that just as in the valley Hall effect in strained graphene, for atoms near the Dirac points, the variations in the hopping matrix elements can be described by a pseudomagnetic fields and result in the formation of relativistic Landau levels. The optical lattice is generated by three laser beams that together form a honeycomb lattice. Starting with three identical beams and allowing their intensity to vary in space should result in a space-dependent shift of the minima of the optical lattice. This property will then generate a space dependent tunneling amplitude (or hopping) that reproduces the effect of strain in graphene, namely the generation of Landau levels at each Dirac cones. At the same time they observe a shift in the position of the Dirac cones in momentum space. This shift can be encoded into the Dirac equations by adding a vector potential in the same way as we did in section 2.3.

The motivation of the following chapters is to propose an alternative scheme to obtain linear strain that builds on space-dependent hopping, using a new strategy that is specific to ultracold atoms. In place of using variations of the laser beams

intensity, we will rather use a mixture of ultracold atoms whose interactions induce density-dependent hopping parameters and we will exploit the space-dependence of the density of a trapped gas to mimic the effect of strain as we will show later in this work.

Chapter 3

Weakly interacting Bose-Einstein condensate in optical lattice

This chapter is dedicated to the introduction of the relevant concepts both in non-interacting and weakly interacting Bose-Einstein condensates. We deduce the Gross-Pitaevskii equation from the Bose-Hubbard model in the mean-field approximation, both in the continuum and on a 1D optical lattice. Then we discuss the Thomas-Fermi regime, which provides useful analytical relations that will serve as tests for our numerical results. Finally we solve the Gross-Pitaevskii equation with the self-consistent method and imaginary-time method. We then compare results from these methods with each other and with the analytical relations mentioned above.

3.1 Bose-Einstein condensation in continuum

3.1.1 The ideal Bose gas

Bosons are particles with integer spins therefore, for a system of identical bosons, the wave function is symmetric under exchange of any two particles. Unlike fermions, which have half-integer spin and antisymmetric wave functions, bosons may occupy the same single-particle state. The phenomenon called *Bose-Einstein condensation* occurs when bosons occupy the lowest state. More specifically condensation occurs when the occupation number of the lowest state is of the order of the total number of particles $N = \sum_i \nu_i$ while the other single-particle states have a occupation number of order 1. To understand this phenomenon we need to look at the average occupation numbers in the grand canonical ensemble for independent particles. For the i^{th} level the occupation, as described by the Bose-Einstein distribution, reads

$$\bar{n}_i = \frac{1}{\exp[\beta(\epsilon_i - \mu)] - 1} \quad (3.1)$$

where $\beta = 1/k_B T$, k_B being the Boltzmann constant, T the temperature and μ

the chemical potential. From the non-negativity of \bar{n}_i , we deduce that $\mu < \epsilon_\nu, \forall \nu$ so evidently μ is also smaller than the lowest energy ϵ_0 . When μ approaches ϵ_0 the occupation number $N_0 \equiv \bar{n}_0$ becomes larger and larger. This is actually the mechanism at the origin of the Bose-Einstein condensation. Let us separate the total number of particles into the particles in the lowest energy state from the others by defining

$$N_T(T, \mu) = \sum_{i \neq 0} \bar{n}_i(T, \mu) \quad (3.2)$$

such that

$$N = N_0 + N_T. \quad (3.3)$$

The number N_T is called the *thermal depletion of the condensate* and grows as particles go out of the condensed state via thermal fluctuations. Since we will stay at $T = 0$ all along this work, we will later discuss depletion originating from quantum fluctuations in an interacting gas. For the rest of the discussion we focus on the free particle case. Following the discussion in [40] the thermal depletion for a free gas in a box of volume V is

$$N_T = \sum_{\mathbf{p} \neq 0} \frac{1}{\exp[(\beta(p^2/2m) - \mu)] - 1} = \frac{V}{\lambda_T^3} g_{3/2}(e^{\beta\mu}), \quad (3.4)$$

where g_p belongs to the class of *Bose functions* – for which $g_{3/2}(1) = 2.612$ – and $\lambda_T = \sqrt{2\pi\hbar^2/mk_B T}$ is the thermal wavelength. The critical temperature¹ T_c can be found thanks to the condition $N_T(T_c, \mu = \epsilon_0) = N$ such that T_c is given by

$$k_B T_c = \frac{2\pi\hbar^2}{m} \left(\frac{N}{V g_{3/2}(1)} \right)^{2/3}, \quad (3.5)$$

Using (3.4) and (3.5) we find from (3.3) that

$$N_0 = N \left[1 - \left(\frac{T}{T_c} \right)^{3/2} \right]. \quad (3.6)$$

Bose-Einstein condensate in harmonic trap

If the BEC is trapped by a harmonic potential, the ground state wave function is a Gaussian:

¹Two types of atoms that are typically used are rubidium and sodium. Their critical temperatures are respectively 170 nK for a density of $2.5 \times 10^{12} \text{ cm}^{-3}$, and 2 μK for a density of 10^{14} cm^{-3} .

$$\Psi(\mathbf{r}) = \left(\frac{m\omega_{ho}}{\pi\hbar}\right)^{3/4} \exp\left[-\frac{m}{2\hbar}(\omega_x x^2 + \omega_y y^2 + \omega_z z^2)\right] \quad \text{with} \quad \int d\mathbf{r} |\Psi(\mathbf{r})|^2 = 1 \quad (3.7)$$

where $\omega_{ho} \equiv (\omega_x \omega_y \omega_z)^{1/3}$. The density distribution of the N -body system is $n(x) = N|\Psi(x)|^2$ and grows with N . The size of the condensate is independent of N and is fixed by the harmonic oscillator length

$$a_{ho} = \left(\frac{\hbar}{m\omega_{ho}}\right)^{1/2}, \quad (3.8)$$

which corresponds to the width of the Gaussian (3.7). At a finite temperature some of the particles occupy the lowest state, the other being distributed among the excited states at higher energies according to (3.1). From the same equation we see that Bose-Einstein condensation takes place when the value of the chemical potential μ is so close to the lowest energy ϵ_0 that the occupation number $\bar{n}_0 \equiv N_0$ of the lowest level becomes comparable to the total number of particles. The critical temperature for Bose-Einstein condensation is defined as before by the equality $N_T = N$, which turns out to be given by the expression

$$k_B T_c^0 = \hbar\omega \left(\frac{N}{\zeta(3)}\right)^{1/3} = 0.94\hbar\omega_{ho} N^{1/3} \quad (3.9)$$

where ζ is the ζ -Riemann function. Therefore the thermal dependence of the condensate fraction N_0/N in this case is

$$\frac{N_0}{N} = 1 - \left(\frac{T}{T_c^0}\right)^3. \quad (3.10)$$

It is worth noticing that this law differs from the one characterizing BEC in a uniform gas in a box – see (3.6) – where the T -dependence of the thermal component behaves like $T^{3/2}$ rather than T^3 . To end this section we compute the kinetic and potential energy of the BEC in d dimensions:

$$\begin{aligned} \frac{E_{\text{kin}}}{N} &= \frac{2d^{d/2}}{\Gamma(d/2)} \frac{\hbar^2}{2m} \int_0^\infty \left(\frac{m\omega_{ho}}{\pi\hbar}\right)^{d/2} \left(\frac{\partial}{\partial r} e^{-\frac{m\omega_{ho} r^2}{2\hbar}}\right)^2 r^{d-1} dr = \frac{d\hbar\omega_{ho}}{4} \\ \frac{E_{\text{pot}}}{N} &= \frac{2d^{d/2}}{\Gamma(d/2)} \int_0^\infty \left(\frac{m\omega_{ho}}{\pi\hbar}\right)^{d/2} \frac{m\omega_{ho}^2}{2} r^2 e^{-\frac{m\omega_{ho} r^2}{\hbar}} r^{d-1} dr = \frac{d\hbar\omega_{ho}}{4} \end{aligned} \quad (3.11)$$

with $\omega_{ho} \equiv (\omega_1 \dots \omega_d)^{1/d}$ and Γ being the Γ -Euler function. We will use the results (3.11) as a comparison for the numerical computations presented later.

3.1.2 Mean-field approximation

Here we present a general treatment of Bose-Einstein condensation that can be applied to a generic bosonic gas. We also introduce the mean-field approximation in order to deal with a weakly interacting system. Let us define the one-body density matrix

$$n^{(1)}(\mathbf{r}, \mathbf{r}') = \langle \hat{\Psi}^\dagger(\mathbf{r}) \hat{\Psi}(\mathbf{r}') \rangle \quad (3.12)$$

If the system occupies a pure state described by the N -body wave function $\Phi_j(\mathbf{r}_1, \dots, \mathbf{r}_N)$ normalized to 1, then its corresponding one-body density matrix can be written as

$$n_j^{(1)}(\mathbf{r}, \mathbf{r}') = N \int d\mathbf{r}_2 \dots \mathbf{r}_N \Phi_j^*(\mathbf{r}, \mathbf{r}_2, \dots, \mathbf{r}_N) \Phi_j(\mathbf{r}', \mathbf{r}_2, \dots, \mathbf{r}_N). \quad (3.13)$$

Instead for a thermal state the one-body density matrix reads

$$n^{(1)}(\mathbf{r}, \mathbf{r}') = \frac{1}{Z} \sum_j e^{-E_j/k_B T} n_j^{(1)}(\mathbf{r}, \mathbf{r}'). \quad (3.14)$$

Occupation numbers and one-body density matrix are related to each other by

$$\int d\mathbf{r}' n^{(1)}(\mathbf{r}, \mathbf{r}') \varphi_i(\mathbf{r}') = \nu_i \varphi_i(\mathbf{r}). \quad (3.15)$$

The set of solutions $\{\varphi_i\}$ of this equation forms a basis of ortho-normalized wave functions. Note that by multiplying (3.15) by $\varphi_i^*(\mathbf{r})$ and integrating over \mathbf{r} we find the normalization condition $\sum_i \nu_i = N$ after employing the completeness relation $\sum_i \varphi_i^*(\mathbf{r}) \varphi_i(\mathbf{r}') = \delta(\mathbf{r} - \mathbf{r}')$. Thus, we can write

$$n^{(1)}(\mathbf{r}, \mathbf{r}') = \sum_i \nu_i \varphi_i^*(\mathbf{r}) \varphi_i(\mathbf{r}') \quad (3.16)$$

Having in mind the particularity of the state φ_0 , we conveniently separate the term $i = 0$ from the rest:

$$n^{(1)}(\mathbf{r}, \mathbf{r}') = N_0 \varphi_0^*(\mathbf{r}) \varphi_0(\mathbf{r}') + \sum_{i \neq 0} \nu_i \varphi_i^*(\mathbf{r}) \varphi_i(\mathbf{r}') \quad (3.17)$$

Furthermore, in second quantization, the field operator $\hat{\Psi}(\mathbf{r})$ can be written in terms of the single-particle wave functions φ_i :

$$\hat{\Psi}(\mathbf{r}) = \sum_i \varphi_i \hat{a}_i, \quad (3.18)$$

where \hat{a}_i (\hat{a}_i^\dagger) are the annihilation (creation) operators of a particle in the state φ_i and satisfy

$$[\hat{a}_i, \hat{a}_j^\dagger] = \delta_{ij}, \quad [\hat{a}_i, \hat{a}_j] = [\hat{a}_i^\dagger, \hat{a}_j^\dagger] = 0. \quad (3.19)$$

Inserting (3.18) into (3.12), we find $\langle \hat{a}_j^\dagger \hat{a}_i \rangle = \delta_{ij} \nu_i$. Again, we separate the ‘condensate term’ from the other terms:

$$\hat{\Psi}(\mathbf{r}) = \varphi_0(\mathbf{r}) \hat{a}_0 + \sum_{i \neq 0} \varphi_i(\mathbf{r}) \hat{a}_i \quad (3.20)$$

We now introduce the *mean-field approximation*. It consists of replacing the operators \hat{a}_0 and \hat{a}_0^\dagger by the number $\sqrt{N_0}$. This means that we are ignoring the noncommutativity of the operators \hat{a}_0 and \hat{a}_0^\dagger since their commutator is equal to 1 which is negligible with respect of $N_0 = \langle \hat{a}_0^\dagger \hat{a}_0 \rangle \gg 1$. Such an approximation is equivalent to treating $\varphi_0 \hat{a}_0$ as a classical field so that (3.20) can be rewritten as

$$\hat{\Psi}(\mathbf{r}) = \Psi_0(\mathbf{r}) + \delta\hat{\Psi}(\mathbf{r}), \quad (3.21)$$

where $\Psi_0 = \sqrt{N_0} \varphi_0$ is the order parameter representing the condensate wavefunction, which is defined up to phase factor², whereas $\delta\hat{\Psi}(\mathbf{r}) = \sum_{i \neq 0} \varphi_i \hat{a}_i$. This last contribution $\delta\hat{\Psi}$ contains the classical fluctuations due to thermal effects and quantum fluctuations due to interparticle interactions. This procedure was originally introduced by Bogoliubov and it provides the basis to treat the weakly interacting Bose gas.

Long-range order

The momentum distribution [40]

$$n(\mathbf{p}) = \langle \hat{\Psi}^\dagger(\mathbf{p}) \hat{\Psi}(\mathbf{p}) \rangle \quad (3.22)$$

is obtained by Fourier-transforming (3.12):

$$n^{(1)}(\mathbf{s}) = \frac{1}{V} \int d\mathbf{p} n(\mathbf{p}) e^{i\mathbf{p} \cdot \mathbf{s}}. \quad (3.23)$$

for $\mathbf{s} = \mathbf{r} - \mathbf{r}'$. Typically the momentum distribution is smooth at small momenta therefore the one-body density matrix vanishes when $\|\mathbf{s}\| \rightarrow \infty$. The story is different in presence of BoseEinstein condensation due to the macroscopic occupation of the state with momentum $\mathbf{p} = 0$. The momentum distribution contains a delta-function term

²One can always multiply this function by the numerical factor $e^{i\alpha}$ without changing any physical property. This reflects the gauge symmetry exhibited by all the physical equations of the problem. Making an explicit choice for the value of the order parameter (and hence for the phase) corresponds to a formal breaking of gauge symmetry.

$$n(\mathbf{p}) = N_0 \delta(\mathbf{p}) + \tilde{n}(\mathbf{p}) \quad (3.24)$$

where $\tilde{n}(\mathbf{p})$ is an unspecified function here that depends on the system under consideration. By taking the Fourier transform of (3.24) in presence of a BEC the one-body density matrix does not vanish at large distances but approaches a finite value:

$$n^{(1)}(s)_{s \rightarrow \infty} \rightarrow \frac{N_0}{V}. \quad (3.25)$$

This behaviour is called *off-diagonal long-range order* (ODLRO) since it involves the off-diagonal components ($\mathbf{r} \neq \mathbf{r}'$) of (3.12).

3.1.3 Weakly interacting gas and Gross-Pitaevskii equation in continuum

From now on, we will assume that the bosonic gas is sufficiently dilute or rarefied meaning that the average distance between particles $n^{-1/3}$ is much bigger than the range r_0 of the interatomic forces ($n^{-1/3}r_0 \ll 1$). In this sense three-body (and more) interactions can be neglected [40]. The many-body Hamiltonian in second quantization describing this type of gas of N interacting bosons in an external potential V_{ext} reads [15]:

$$\begin{aligned} \hat{H}(t) = & \int d\mathbf{r} \hat{\Psi}^\dagger(\mathbf{r}, t) \left[-\frac{\hbar^2}{2m} \nabla^2 + V_{\text{ext}} \right] \hat{\Psi}(\mathbf{r}, t) \\ & + \frac{1}{2} \int d\mathbf{r} d\mathbf{r}' \hat{\Psi}^\dagger(\mathbf{r}, t) \hat{\Psi}^\dagger(\mathbf{r}', t) V(\mathbf{r} - \mathbf{r}') \hat{\Psi}(\mathbf{r}, t) \hat{\Psi}(\mathbf{r}', t) \end{aligned} \quad (3.26)$$

where $\hat{\Psi}^\dagger(\mathbf{r}, t)$ and $\hat{\Psi}(\mathbf{r}, t)$ are respectively the bosonic creation and annihilation field operators. We will consider that interactions between atoms are repulsive ($a_s > 0$) and described by an on-site potential

$$V(\mathbf{r} - \mathbf{r}') = \frac{4\pi\hbar^2 a_s}{m} \delta(\mathbf{r} - \mathbf{r}') \equiv U \delta(\mathbf{r} - \mathbf{r}') \quad (3.27)$$

with m being the atomic mass. The form (3.27) can be obtained from scattering theory arguments at low energy and temperature, where the description of two-body interactions only requires the s-wave channel described a single quantity a_s . The Hamiltonian (3.26) then becomes

$$\begin{aligned} \hat{H}(t) = & \int d\mathbf{r} \hat{\Psi}^\dagger(\mathbf{r}, t) \left[-\frac{\hbar^2}{2m} \nabla^2 + V_{\text{ext}} \right] \hat{\Psi}(\mathbf{r}, t) \\ & + \frac{U}{2} \int d\mathbf{r} \hat{\Psi}^\dagger(\mathbf{r}, t) \hat{\Psi}^\dagger(\mathbf{r}, t) \hat{\Psi}(\mathbf{r}, t) \hat{\Psi}(\mathbf{r}, t) \end{aligned} \quad (3.28)$$

Finally we will assume that the gas is weakly interacting meaning that we require

$$|a_s| \max(n)^{1/d} \ll 1 \quad (3.29)$$

with n the density of the gas and d the dimension of the system. This important condition can be rewritten as

$$\left(\frac{Um}{4\pi\hbar^2}\right)^d n \ll 1. \quad (3.30)$$

The Gross-Pitaevskii equation

To establish the equation governing the order parameter $\Psi(\mathbf{r}, t)$ defined in equation (3.21), we first use the Heisenberg equation for the field operator $\hat{\Psi}(\mathbf{r}, t)$:

$$i\hbar \frac{\partial}{\partial t} \hat{\Psi}(\mathbf{r}, t) = [\hat{\Psi}(\mathbf{r}, t), \hat{H}] = \left[-\frac{\hbar^2}{2m} \nabla^2 + V_{\text{ext}}(\mathbf{r}, t) + U \hat{\Psi}^\dagger(\mathbf{r}, t) \hat{\Psi}(\mathbf{r}, t) \right] \hat{\Psi}(\mathbf{r}, t), \quad (3.31)$$

using the fact that $[\hat{\Psi}(\mathbf{r}', t), \hat{\Psi}^\dagger(\mathbf{r}, t)] = \delta(\mathbf{r} - \mathbf{r}')$. Supposing that our system is an bosonic dilute gas with binary, short-range interactions at temperature near the absolute zero, we employ the mean-field description, i.e. we neglect any fluctuation, and replace $\hat{\Psi}(\mathbf{r}, t)$ in (3.28) by its expectation value $\Psi(\mathbf{r}, t)$. In the end we can simply replace the field operator by its expectation value Ψ and we obtain the so-called time-dependent Gross-Pitaevskii equation

$$i\hbar \frac{\partial}{\partial t} \Psi(\mathbf{r}, t) = \left[-\frac{\hbar^2}{2m} \nabla^2 + V_{\text{ext}}(\mathbf{r}, t) + U |\Psi(\mathbf{r}, t)|^2 \right] \Psi(\mathbf{r}, t) \quad (3.32)$$

The function $\Psi_0(\mathbf{r})$ is a complex quantity characterized by a modulus and a phase:

$$\Psi_0(\mathbf{r}) = |\Psi_0(\mathbf{r})| e^{iS(\mathbf{r})}. \quad (3.33)$$

The modulus determines the contribution of the condensate to the diagonal density matrix (3.12). The phase $S(\mathbf{r})$ contributes to coherence and superfluid phenomena.

As explained in [40], in the mean-field approximation (3.21), the expectation value $\langle \hat{\Psi} \rangle$ does not vanish. This statement would not be true if the states on the left and on the right had the same number of particles³. Since $N_0 \gg 1$ adding a particle in the condensate has no influence on the system. In other terms, the state $|N\rangle$ containing N particles and the states $|N+1\rangle \propto \hat{a}_0^\dagger |N\rangle$ and $|N-1\rangle \propto \hat{a}_0 |N\rangle$ are physically equivalent apart from the corrections of order $1/N_0$. Therefore we can

³The quantity $\langle N | \hat{\Psi} | N \rangle$ vanishes since $\langle N | M \rangle = \delta_{NM}$ and $\hat{\Psi} | N \rangle = \sqrt{N-1} | N-1 \rangle$.

have $\Psi_0 = \langle \hat{\Psi} \rangle$ if we assume that the expectation value is taken over states with no fixed number of particles but whose average density is peaked around N_0 . Similarly we have $\Psi_0^* = \langle \hat{\Psi}^\dagger \rangle$. If we take this average over stationary states $|\Psi_N\rangle(\mathbf{r}, t) = e^{-iE_N t/\hbar} |\Psi_N\rangle(\mathbf{r})$, it is easy to see that the time dependence of the order parameter is given by the law

$$\Psi_0(\mathbf{r}, t) = \Psi_0(\mathbf{r}) e^{-i\mu t/\hbar}, \quad (3.34)$$

where $\mu = E(N) - E(N-1) \simeq \partial E / \partial N$ is the chemical potential. Finally, we obtain the time-independent Gross-Pitaevskii equation when we substitute (3.34) into (3.32):

$$-\frac{\hbar^2}{2m} \nabla^2 \Psi(\mathbf{r}) + V_{\text{ext}}(\mathbf{r}) \Psi(\mathbf{r}) + U |\Psi(\mathbf{r})|^2 \Psi(\mathbf{r}) = \mu \Psi(\mathbf{r}) \quad (3.35)$$

Eventually we obtain the energy functional by substituting $\hat{\Psi}$ and $\hat{\Psi}^\dagger$ by Ψ_0 and Ψ_0^* respectively in (3.28):

$$E[\Psi] = \int d^d \mathbf{r} \Psi^*(\mathbf{r}, t) \left[-\frac{\hbar^2}{2m} \nabla^2 + V_{\text{ext}} \right] \Psi(\mathbf{r}, t) + \frac{U}{2} \int d^d \mathbf{r} |\Psi(\mathbf{r}, t)|^4 \quad (3.36)$$

where we generalized to d dimensions. We are able to identify three energy contributions to the energy functional:

$$\begin{aligned} E_{\text{kin}} &= -\frac{\hbar^2}{2m} \int d^d \mathbf{r} \Psi^*(\mathbf{r}, t) \nabla^2 \Psi(\mathbf{r}, t) = \frac{\hbar^2}{2m} \int d^d \mathbf{r} |\nabla \Psi(\mathbf{r}, t)|^2 \\ E_{\text{pot}} &= \int d^d \mathbf{r} V_{\text{ext}}(\mathbf{r}, t) |\Psi(\mathbf{r}, t)|^2 \\ E_{\text{int}} &= \frac{U}{2} \int d^d \mathbf{r} |\Psi(\mathbf{r}, t)|^4 \end{aligned} \quad (3.37)$$

Note that the equation (3.35) can also be obtained from a variational principle by imposing the stationary condition to the energy (3.36) with respect to variations of Ψ_0^* , with the constraint that the number $N = N_0$ of particles is fixed regarding μ as a Lagrange multiplier.

3.1.4 Thomas-Fermi regime in the harmonic trap

The physical consequence of the repulsive interaction is the expansion of the cloud with respect to the non-interacting case. Since the total number of particles is fixed, for stronger and stronger interactions the density profile of the cloud will become broader since a high density in the center costs energy and it is energetically more convenient to bring the particles away from the center in order to reduce the density. The density profile will then become flatter and the gradient $\nabla \Psi$ will

become smaller and smaller. As a consequence, the kinetic energy represented by the first of equations (3.37) will become negligible compared to the other two energy contributions, namely the potential and interaction energies. This regime is called the *Thomas-Fermi regime*. The Gross-Pitaevskii equation in this regime becomes

$$V_{\text{ext}}(\mathbf{r})\psi(\mathbf{r}) + U|\psi(\mathbf{r})|^2\psi(\mathbf{r}) = \mu\psi(\mathbf{r}) \quad (3.38)$$

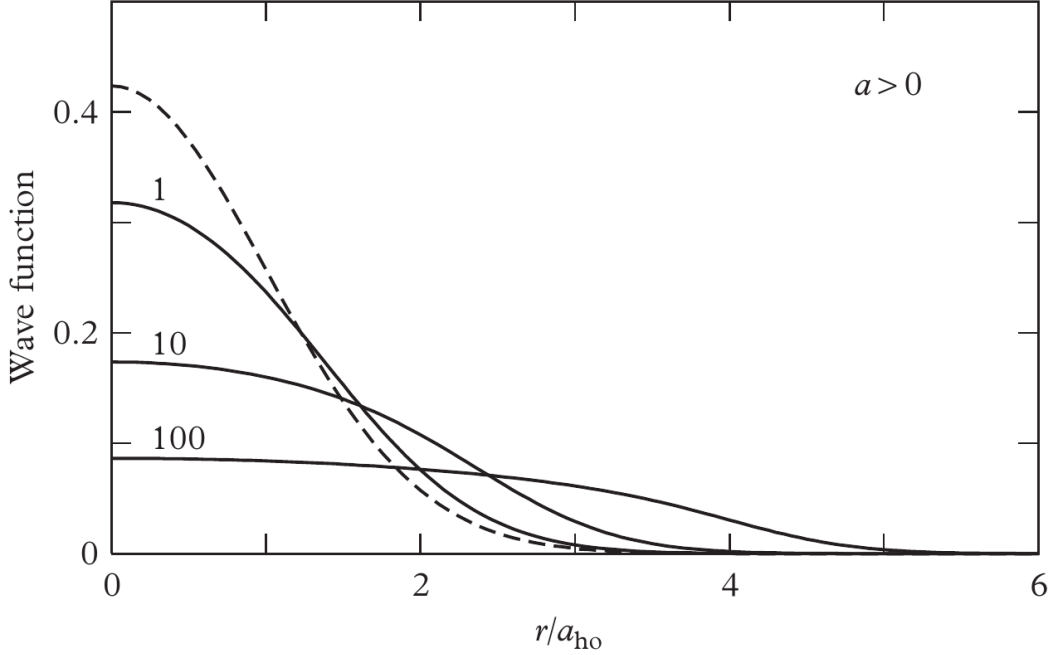


Figure 3.1: (Figure from reference [40]) Normalized wavefunctions of the BEC for various values of the interaction parameter Na_s/a_{ho} . The distance with respect to the center r is divided by the width a_{ho} of the wavefunction for $U = 0$, which is a Gaussian. The parameter a_s (a in the figure) is the s -wave scattering length.

Assuming $\Psi \neq 0$ everywhere, the Thomas-Fermi (TF) density is

$$n_{\text{TF}} = |\Psi(\mathbf{r})|^2 = \frac{1}{U} (\mu - V_{\text{ext}}(\mathbf{r})) \quad (3.39)$$

with $\mu > V_{\text{ext}}(\mathbf{r})$ everywhere in the cloud. If we choose the external potential to be

$$V_{\text{ext}}(\mathbf{r}) = \frac{m\omega_0^2}{2} r^2 \equiv \frac{V_0}{2} r^2, \quad (3.40)$$

then the density is simply a parabola centered at origin:

$$n_{\text{TF}}(r) = \frac{1}{U} \left(\mu - \frac{V_0}{2} r^2 \right). \quad (3.41)$$

By computing the number of particles N with the TF density in d dimension, we

find

$$\begin{aligned}
N &= \frac{2\pi^{d/2}}{\Gamma(d/2)U} \int_0^{R/2} dr r^{d-1} \left(\mu - \frac{V_0}{2} r^2 \right) \\
&= \frac{\mu^{1+d/2}}{U} \left(\frac{2}{V_0} \right)^{d/2} \frac{4}{d(d+2)} \frac{\pi^{d/2}}{\Gamma(d/2)}.
\end{aligned} \tag{3.42}$$

We also have at our disposal a relation between μ , R (the total size of the cloud) and V_0 that comes from the vanishing of the density at the boundaries (at $r = \pm R/2$):

$$\mu = \frac{V_0}{8} R^2 \tag{3.43}$$

By isolating μ in (3.42), we obtain

$$\mu = \left[U \left(\frac{V_0}{2} \right)^{d/2} \frac{d(d+2)}{4} \frac{\Gamma(d/2)}{\pi^{d/2}} \right]^{2/(d+2)} N^{2/(d+2)} \tag{3.44}$$

Since $\mu = \frac{\partial E}{\partial N}$ we find that the energy is

$$E = \left[U \left(\frac{V_0}{2} \right)^{d/2} \frac{d(d+2)}{4} \frac{\Gamma(d/2)}{\pi^{d/2}} \right]^{2/(d+2)} \frac{d+2}{d+4} N^{(d+4)/(d+2)} = \frac{d+2}{d+4} \mu N \tag{3.45}$$

as obtained in [40].

Importantly the TF approximation is applicable only in the center of the cloud. Indeed, even if the gradient of a wavefunction can be neglected in the bulk of a system it can not be neglected at its boundaries where the wavefunction goes from a finite value to zero [41]. To solve this problem finite-size corrections to the TF limit are studied in [42]. In this sense the TF regime must be thought only as an asymptotic limit that will be helpful to check the validity of our codes. This asymptotic character explains why we can not perfectly superimpose the parabola with data computed with any value of U . Nevertheless as shown in figure 3.2 it is effectively possible to tend to the TF regime. By keeping N and V_0 fixed and varying U we see that the parabolas n_{TF} (in dashed lines) fit better the densities n_0 as U increases.

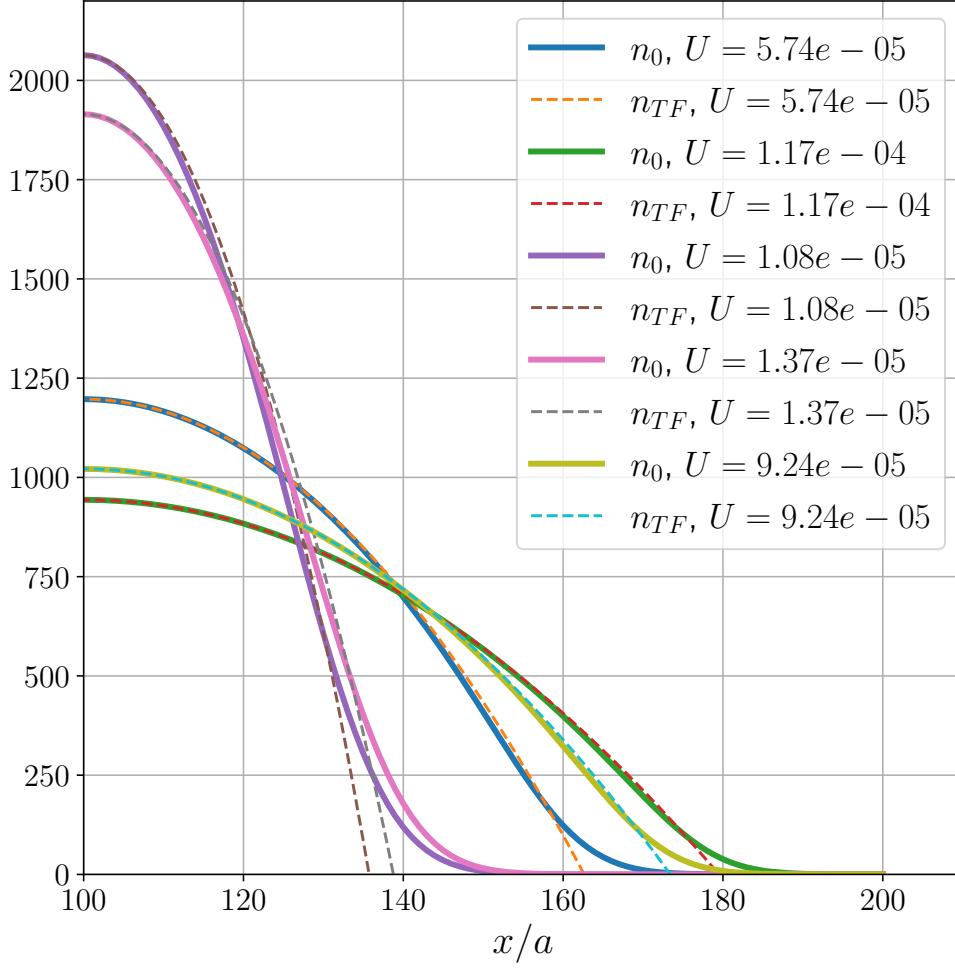


Figure 3.2: Comparison between the densities of the BEC for various values of the interaction parameter U with the TF densities computed for the same values of parameters $N = 10^5$, $V_0 = 3.5 \times 10^{-5}$. The densities n_0 are obtained with the self-consistent method – see section 3.2.2.

3.1.5 Virial theorem and relations between the energy contributions

We can deduce a virial theorem in d dimensions that rely the different energy contributions. First by simply multiplying the Gross-Pitaevskii equation (3.35) by Ψ^* and integrating over \mathbf{r} , we obtain a general relation:

$$\mu N = E_{\text{kin}} + E_{\text{pot}} + 2E_{\text{int}}. \quad (3.46)$$

Thanks to the scaling argument provided in [43] we find the virial theorem for our problem:

$$2E_{\text{kin}} - 2E_{\text{pot}} + dE_{\text{int}} = 0 \quad (3.47)$$

Thanks to the relationships (3.46) and (3.47), new relations can be derived. Indeed, if $E_{\text{kin}} = E_{\text{int}}$

$$\frac{E_{\text{int}}}{N} = \frac{2}{8+d}\mu \quad (3.48)$$

and when $E_{\text{pot}} = E_{\text{int}}$, we have

$$\frac{E_{\text{int}}}{N} = \frac{2}{8-d}\mu \quad (3.49)$$

These relations will help us to check the correctness of what is computed by the numerical calculations that we present in the next sections.

3.1.6 Depletion of the condensate by quantum fluctuations

In section 3.1.2 we neglected the quantum fluctuations by taking into account only the particle operators $\hat{a}_{\mathbf{p}}^\dagger$ and $\hat{a}_{\mathbf{p}}$ for $\mathbf{p} = 0$. Here we discuss the effect of quantum fluctuations in a uniform system. Using the Fourier transform

$$\hat{\Psi}(\mathbf{r}) = \sum_{\mathbf{p}} \hat{a}_{\mathbf{p}} \frac{1}{\sqrt{V}} e^{i\mathbf{p}\cdot\mathbf{r}/\hbar} \quad (3.50)$$

on the Hamiltonian (3.26) we find

$$\hat{H} = \sum_{\mathbf{p}} \frac{p^2}{2m} \hat{a}_{\mathbf{p}}^\dagger \hat{a}_{\mathbf{p}} + \frac{1}{2V} U \sum_{\mathbf{p}_1, \mathbf{p}_2} \hat{a}_{\mathbf{p}_1}^\dagger \hat{a}_{\mathbf{p}_2}^\dagger \hat{a}_{\mathbf{p}_1} \hat{a}_{\mathbf{p}_2}. \quad (3.51)$$

By keeping only the quadratic terms in the particle operators with $\mathbf{p} \neq 0$, we obtain

$$\hat{H} = \frac{U}{2V} \hat{a}_0^\dagger \hat{a}_0^\dagger \hat{a}_0 \hat{a}_0 + \sum_{\mathbf{p}} \frac{p^2}{2m} \hat{a}_{\mathbf{p}}^\dagger \hat{a}_{\mathbf{p}} + \frac{U}{2V} \sum_{\mathbf{p} \neq 0} \left(4\hat{a}_0^\dagger \hat{a}_{\mathbf{p}}^\dagger \hat{a}_0 \hat{a}_{\mathbf{p}} + \hat{a}_{\mathbf{p}}^\dagger \hat{a}_{-\mathbf{p}}^\dagger \hat{a}_0 \hat{a}_0 + \hat{a}_0^\dagger \hat{a}_0^\dagger \hat{a}_{\mathbf{p}} \hat{a}_{\mathbf{p}} \right) \quad (3.52)$$

where $\mathbf{p}_1 = -\mathbf{p}_2 \equiv \mathbf{p}$ by momentum conservation. Since $\hat{a}_0^\dagger \hat{a}_0 = N - \sum_{\mathbf{p} \neq 0} \hat{a}_{\mathbf{p}}^\dagger \hat{a}_{\mathbf{p}}$ we find

$$\hat{a}_0^\dagger \hat{a}_0^\dagger \hat{a}_0 \hat{a}_0 = N^2 - 2N \sum_{\mathbf{p} \neq 0} \hat{a}_{\mathbf{p}}^\dagger \hat{a}_{\mathbf{p}} \quad (3.53)$$

A correction can also be made in the relation between U_0 and the scattering length. Previously we had $U = \frac{4\pi\hbar^2 a_s}{m}$ but if we go beyond the lowest-order Born-approximation

in scattering theory, we find the renormalized relation between the effective potential and U

$$U \rightarrow U \left(1 + \frac{U}{V} \sum_{\mathbf{p} \neq 0} \frac{m}{p^2} \right). \quad (3.54)$$

Substitution of (3.53) and (3.54) into (3.52) gives

$$\hat{H} = U \frac{N^2}{2V} + \sum_{\mathbf{p}} \frac{p^2}{2m} \hat{a}_{\mathbf{p}}^\dagger \hat{a}_{\mathbf{p}} + \frac{1}{2} U n \sum_{\mathbf{p} \neq 0} \left(2 \hat{a}_{\mathbf{p}}^\dagger \hat{a}_{\mathbf{p}} + \hat{a}_{\mathbf{p}}^\dagger \hat{a}_{-\mathbf{p}}^\dagger + \hat{a}_{\mathbf{p}} \hat{a}_{-\mathbf{p}} + \frac{m U n}{p^2} \right). \quad (3.55)$$

for $n = N/V$. This Hamiltonian can be diagonalized thanks by the *Bogoliubov transformation*:

$$\hat{a}_{\mathbf{p}} = u_{\mathbf{p}} \hat{b}_{\mathbf{p}} + v_{-\mathbf{p}}^* \hat{b}_{-\mathbf{p}}^\dagger \quad \hat{a}_{\mathbf{p}}^\dagger = u_{\mathbf{p}}^* \hat{b}_{\mathbf{p}}^\dagger + v_{-\mathbf{p}} \hat{b}_{-\mathbf{p}}. \quad (3.56)$$

If we want to impose the new set of operators $\{\hat{b}_{\mathbf{p}}^\dagger, \hat{b}_{\mathbf{p}}\}$ to obey the Bose commutation relations $\hat{b}_{\mathbf{p}} \hat{b}_{\mathbf{p}}^\dagger - \hat{b}_{\mathbf{p}}^\dagger \hat{b}_{\mathbf{p}} = \delta_{\mathbf{p}\mathbf{p}'}$, as the operators $\hat{a}_{\mathbf{p}}^\dagger, \hat{a}_{\mathbf{p}}$ did, the coefficients $u_{\mathbf{p}}, v_{\mathbf{p}}$ must satisfy

$$|u_{\mathbf{p}}|^2 + |v_{-\mathbf{p}}|^2 = 1 \quad (3.57)$$

i.e. if we can write $u_{\mathbf{p}} = \cosh(\alpha_{\mathbf{p}})$, $v_{-\mathbf{p}} = \sinh(\alpha_{\mathbf{p}})$. The coefficient $\alpha_{\mathbf{p}}$ is chosen in such a way that the off-diagonal terms $\hat{b}_{\mathbf{p}}^\dagger \hat{b}_{-\mathbf{p}}^\dagger$ and $\hat{b}_{\mathbf{p}} \hat{b}_{\mathbf{p}}$ of the Hamiltonian (3.55) vanish. This condition takes the form

$$\coth(2\alpha_{\mathbf{p}}) = -\frac{p^2/2m + U n}{U n} \quad (3.58)$$

therefore the explicit form of the coefficients $u_{\mathbf{p}}$ and $v_{\mathbf{p}}$ becomes

$$u_{\mathbf{p}}, v_{\mathbf{p}} = \pm \left(\frac{p^2/2m + U n}{2\epsilon(p)} \pm \frac{1}{2} \right)^{1/2} \quad (3.59)$$

where $\epsilon(p)$ is the *Bogoliubov dispersion law* for the elementary excitations of the system:

$$\epsilon(p) = \left[\frac{U n}{m} p^2 + \left(\frac{p^2}{2m} \right)^2 \right]^{1/2}. \quad (3.60)$$

Once diagonalized the Hamiltonian reads

$$\hat{H} = E_0 + \sum_{\mathbf{p} \neq 0} \epsilon(p) \hat{b}_{\mathbf{p}}^\dagger \hat{b}_{\mathbf{p}} \quad (3.61)$$

where

$$E_0 = U \frac{N^2}{2V} + \frac{1}{2} \sum_{\mathbf{p} \neq 0} \left[\epsilon(p) - Un - \frac{p^2}{2m} + \frac{m(Un)^2}{p^2} \right] \quad (3.62)$$

is the ground state energy calculated to the higher order in mUn/p^2 . The physical meaning of (3.61) is that the original system of interacting particles can be described in terms of independent quasi-particles with respect to the BEC as a vacuum, having energy $\epsilon(p)$ and whose creation and annihilation operators are given, respectively, by $\hat{b}_{\mathbf{p}}^\dagger$ and $\hat{b}_{\mathbf{p}}$.

Phonon-like excitations and superfluidity

Interestingly for small momentum $p \ll mc$, where $c \equiv \sqrt{Un/m}$ is known as the sound velocity, the dispersion law of quasi-particles (3.60) takes the form

$$\epsilon(p) = cp \quad (3.63)$$

which reminds us the phonon dispersion relation. This means that the low energy excitations of an interacting Bose gas are sound waves. In the opposite limit $p \gg mc$ the dispersion relation is:

$$\epsilon(p) = \frac{p^2}{2m} + Un. \quad (3.64)$$

which is the one of a free particle. Besides, since the number of excitations is not constant nor limited, the chemical potential of the quasi-particles is zero. Their average occupation number $N_{\mathbf{p}}$ with momentum \mathbf{p} is then given by

$$N_{\mathbf{p}} \equiv \langle \hat{b}_{\mathbf{p}}^\dagger \hat{b}_{\mathbf{p}} \rangle = \frac{1}{\exp(\beta\epsilon(p)) - 1}. \quad (3.65)$$

However this occupation number is different from $\langle \hat{a}_{\mathbf{p}}^\dagger \hat{a}_{\mathbf{p}} \rangle$ that is directly related to the particle momentum distribution. Inverting (3.56) we find

$$n_{\mathbf{p}} = \langle \hat{a}_{\mathbf{p}}^\dagger \hat{a}_{\mathbf{p}} \rangle = |v_{-\mathbf{p}}|^2 + |u_{\mathbf{p}}|^2 \langle \hat{b}_{\mathbf{p}}^\dagger \hat{b}_{\mathbf{p}} \rangle + |v_{-\mathbf{p}}|^2 \langle \hat{b}_{-\mathbf{p}}^\dagger \hat{b}_{-\mathbf{p}} \rangle. \quad (3.66)$$

Since at $T = 0$ $\langle \hat{b}_{\mathbf{p}}^\dagger \hat{b}_{\mathbf{p}} \rangle = 0$, interactions in the gas introduce particles with non-zero momentum and their number occupation is given by

$$n_{\mathbf{p}} \equiv |v_{-\mathbf{p}}|^2 = \frac{p^2/2m + Un}{2\epsilon(p)} - \frac{1}{2}. \quad (3.67)$$

The depletion number of the condensate due to quantum fluctuations at absolute zero is computed by integrating (3.67) over all \mathbf{p} :

$$N_T = \frac{8V}{3\sqrt{\pi}} (na^3)^{1/2}. \quad (3.68)$$

Before closing this paragraph, it is worth mentioning the concept of superfluidity, namely the fact that a weakly interacting gas of bosons manifests frictionless flow. Indeed, the Landau criterion that is solely based on Galileian invariance [40] shows that a linear spectrum, as for the Bogoliubov spectrum of excitation that we have just derived, is a sufficient condition for superfluidity.

3.2 Weakly interacting Bose-Einstein condensate in optical lattice

In order to simulate condensed matter systems, it is crucial to be able to simulate crystal-like structure as they appear in solid state materials. As we mentioned in section 1.2.2, light can be used to trap ultracold atoms in a large variety of periodic geometries. For example by taking a cubic optical lattice potential obtained by standing waves of light

$$V_{\text{ext}} = V_x \cos(2k_0 x) + V_y \cos(2k_0 y) + V_z \cos(2k_0 z) \quad (3.69)$$

where V_x, V_y and V_z are the depths of the optical lattice depths in the x, y and z directions respectively and where $\hbar k_0$ is photon momentum of the laser beam. We suppose that $V_x, V_y, V_z \gg E_R$ – where $E_R = \hbar^2 k_0^2 / 2m$ is the *recoil energy* of an atom – which means that the wave function of each atom is steeply localized on the intensity minima of the optical potential. In other words the atoms occupy the lowest energy state of each well. We can therefore use the tight-binding approximation allowing to write the field operator $\hat{\Psi}$ as a sum of wave functions $\Theta(\mathbf{r} - \mathbf{r}_i)$, called *Wannier functions*, localized in each well of the potential that shapes the optical lattice:

$$\hat{\Psi}(\mathbf{r}, t) = \sum_i \hat{b}_i \Theta(\mathbf{r} - \mathbf{r}_i) \quad (3.70)$$

where \hat{b}_i (\hat{b}_i^\dagger) denotes the annihilation (creation) operator of a particle localized to the i^{th} lattice site (with position \mathbf{r}_i) that obeys commutation relations $[\hat{b}_i, \hat{b}_j^\dagger] = \delta_{ij}$. Substituting (3.70) into (3.28), we obtain the *Bose-Hubbard Hamiltonian*:

$$\hat{H} = \sum_{\langle i, j \rangle} t_{ij} (\hat{b}_i^\dagger \hat{b}_j + h.c.) + \frac{1}{2} \sum_i U \hat{n}_i (\hat{n}_i - 1) \quad (3.71)$$

where the density operator $\hat{n}_i = \hat{b}_i^\dagger \hat{b}_i$, the hopping parameters from the site i to the j site (or from j to i) is

$$t_{ij} = - \int d\mathbf{r} \Theta^*(\mathbf{r} - \mathbf{r}_i) \left[-\frac{\hbar^2}{2m} \nabla^2 + V_{\text{ext}} \right] \Theta(\mathbf{r} - \mathbf{r}_j) \quad (3.72)$$

and

$$U = \frac{4\pi\hbar^2 a_s}{m} \int d\mathbf{r} |\Theta(\mathbf{r} - \mathbf{r}_i)|^4 \quad (3.73)$$

We note that the parameter U that we are using here is different from the one that have been defined in the continuum because it contains information about the optical lattice through the Wannier function integral. The notation $\langle i, j \rangle$ indicates that only nearest-neighbour hopping processes are included. In the mean-field approximation, we find $\hat{b}_i = \langle \hat{b}_i \rangle + \delta\hat{\Psi}_i = \Psi_i + \delta\hat{\Psi}_i$ and ignoring the fluctuations, we obtain the energy functional

$$E[\psi] = J \sum_{\langle i, j \rangle} (\Psi_j^* \Psi_i + h.c.) + \frac{V_0}{2} \sum_i \mathbf{r}_i^2 |\Psi_i|^2 + \frac{U}{2} \sum_i |\Psi_i|^4 - \frac{UN}{2} \quad (3.74)$$

with $\sum_i |\Psi_i|^2 = N$ and we supposed that the hopping parameters are equal to J due the isotropy of the system.

3.2.1 Bose-Einstein condensate on a 1D lattice

Let us focus on the case of a Bose-Einstein condensate in a 1D lattice with a harmonic trap centered in the middle of the lattice. The energy functional (3.74) becomes

$$\begin{aligned} E[\Psi] = & -J \sum_i [\Psi_{i+1}^* \Psi_i + \Psi_i^* \Psi_{i+1}] + \frac{V_0}{2} \sum_i \left(i - \frac{N_x}{2}\right)^2 a^2 |\Psi_i|^2 \\ & + \frac{U}{2} \sum_i |\Psi_i|^4 - \frac{UN}{2} \end{aligned} \quad (3.75)$$

with a the lattice spacing between two neighbouring sites and N_x the total number of sites. Taking the functional derivative of $E[\Psi, \Psi^*]$ by Ψ^* gives

$$\frac{\delta E[\Psi, \Psi^*]}{\delta \Psi_i^*} = -J[\Psi_{i-1} + \Psi_{i+1}] + \frac{V_0}{2} \left(i - \frac{N_x}{2}\right)^2 a^2 \Psi_i + U|\Psi_i|^2 \Psi_i \quad (3.76)$$

Note that

$$\sum_i \frac{\delta(\Psi_i \Psi_{i+1}^*)}{\delta \Psi_j^*} = \sum_i \Psi_i \frac{\delta \Psi_{i+1}^*}{\delta \Psi_j^*} = \sum_i \Psi_i \delta_{i, j-1} = \Psi_{j-1}$$

Taking into account the constrain $N = \sum_i |\Psi_i|^2$, minimizing the functional $E - \mu N$

with μ constant gives

$$\begin{aligned}
0 &= \frac{\delta(E - \mu N)}{\delta \Psi_i^*} \\
&= -J[\Psi_{i-1} + \Psi_{i+1}] + \frac{V_0}{2} \left(i - \frac{N_x}{2}\right)^2 a^2 \Psi_i + U|\Psi_i|^2 \Psi_i - \mu \Psi_i
\end{aligned} \tag{3.77}$$

that becomes

$$-J[\phi_{i-1} + \phi_{i+1}] + \frac{V_0}{2} \left(i - \frac{N_x}{2}\right)^2 a^2 \phi_i + UN|\phi_i|^2 \phi_i = \mu \phi_i \tag{3.78}$$

after substituting Ψ by $\sqrt{N}\phi$ and divide by \sqrt{N} . We have therefore derived a discrete version of the time-independed Gross-Pitaevskii equation that we have discussed in section 3.1.3 for the continuum case. This set of N_x equations can be rewritten as a non-linear eigenvalue problem $H_{GP}(\phi)\phi = \mu\phi$:

$$\begin{pmatrix}
\ddots & \ddots & & \ddots & & \\
& -J & W(\phi_{i-1}, i-1) & & -J & \\
& & & -J & W(\phi_i, i) & -J \\
& & & & -J & W(\phi_{i+1}, i+1) & -J \\
& & & & & \ddots & \ddots & \ddots
\end{pmatrix}
\begin{pmatrix}
\vdots \\
\phi_{i-1} \\
\phi_i \\
\phi_{i+1} \\
\vdots
\end{pmatrix}
= \mu
\begin{pmatrix}
\vdots \\
\phi_{i-1} \\
\phi_i \\
\phi_{i+1} \\
\vdots
\end{pmatrix} \tag{3.79}$$

for $i \in \{0, \dots, N_x\}$, where $W(\phi_i, i) \equiv \frac{V_0 a^2}{2} \left(i - \frac{N_x}{2}\right)^2 + U|\phi_i|^2$. The section 3.2.2 is devoted to present two numerical techniques to compute μ and ϕ . Before discussing the solution of the previous nonlinear equation, we calculate the expressions for the different energy contributions. The kinetic energy reads

$$E_{\text{kin}} = -J \sum_i [\Psi_{i+1} \Psi_i^* + \Psi_i \Psi_{i+1}^*]. \tag{3.80}$$

Introducing the finite difference Laplacian of Ψ

$$\Delta_f \Psi = \frac{\Psi_{i+1} - 2\Psi_i + \Psi_{i-1}}{a^2} \tag{3.81}$$

we can reformulate the kinetic energy in terms of it. Since

$$\begin{aligned}
E_{\text{kin}} &= -J \sum_{i=0}^{N_x-1} \Psi_{i+1}^* \Psi_i - J \sum_{i=0}^{N_x-1} \Psi_{i+1} \Psi_i^* \\
&= -J \sum_{i=1}^{N_x} \Psi_i^* \Psi_{i-1} - J \sum_{i=0}^{N_x-1} \Psi_{i+1} \Psi_i^* \\
&= \underbrace{-J \Psi_{N_x}^* \Psi_{N_x-1} - J \Psi_1 \Psi_0^*}_{\text{Boundary effect}} - J \sum_{i=1}^{N_x-1} \Psi_i^* (\Psi_{i+1} + \Psi_{i-1}) \\
&\simeq -Ja^2 \sum_i \Psi_i^* \left[\frac{\Psi_{i+1} + \Psi_{i-1} - 2\Psi_i}{a^2} + \frac{2\Psi_i}{a^2} \right] \\
&= -Ja^2 \sum_i \Psi_i^* \Delta_f \Psi_i - 2JN
\end{aligned} \tag{3.82}$$

where the boundary effects were neglected because $N_x \gg 1$ and the wave function of the BEC, Ψ , is sufficiently smooth and tends to 0 at the boundaries of the system. The potential energy reads

$$E_{\text{pot}} = \frac{V_0 a^2}{2} \sum_i \left(i - \frac{N_x}{2} \right)^2 |\Psi_i|^2 \tag{3.83}$$

while the interacting energy is

$$E_{\text{int}} = \frac{U}{2} \sum_i |\Psi_i|^4 - \frac{UN}{2}. \tag{3.84}$$

After, incorporating the discrete Laplacian in the Gross-Pitaevskii equation (3.78) leads to

$$-Ja^2 \Delta_f \phi_i + \frac{V_0 a^2}{2} \left(i - \frac{N_x}{2} \right)^2 \phi_i + UN |\phi_i|^2 \phi_i = (\mu + 2J) \phi_i. \tag{3.85}$$

We are now facing a similar situation than in the continuum case (3.35) except that the chemical potential is now shifted by half the bandwidth. This shift must be taken into account to compare numerical and analytical results as we will show later. If the TF regime is reached, the term in (3.75) containing the Laplacian becomes negligible and the TF density is

$$n_{\text{TF}} = |\Psi(\mathbf{r})|^2 = \frac{N}{U} (\mu + 2J - V_{\text{ext}}(\mathbf{r})). \tag{3.86}$$

Furthermore the number of particles is $N = \sum_i n_{\text{TF}}(i)$ for $-\frac{R}{2} \leq (i - \frac{N_x}{2})a \leq \frac{R}{2}$, R being the size the cloud. We define M the number of sites in the cloud, such that

$R = Ma$. We deduce a relation between μ, N, V_0 and R :

$$N = \frac{1}{U} \sum_{i=0}^M \left[\mu + 2J - \frac{V_0 a^2}{2} \left(i - \frac{M}{2} \right)^2 \right] = \frac{2(\mu + 2J)}{3U} \left(M - \frac{1}{M} \right). \quad (3.87)$$

Note the use of the identity

$$\sum_{i=1}^M i^2 = \frac{M(M+1)(2M+1)}{6} \quad (3.88)$$

and the replacement of N_x by M in the expression of the potential V_{ext} , necessary for cancellation of the density at $i = M$, supposing that the center of the cloud is at the centre of the system. From (3.87), we conclude that for $M \rightarrow \infty$, the result (3.42) for $d = 1$ is recovered.

3.2.2 Numerical solution of Gross-Pitaevskii equation in a 1D lattice

In this section we solve the Gross-Pitaevskii equation. Its non-linear character makes it, in general, impossible to solve analytically. Fortunately, we have at our disposal numerical techniques and two of them are presented in the following subsections. After introducing them both, we will then compare them with each other and with the analytical results derived above for the 1D lattice.

Imaginary time method

The first method to solve the Gross-Pitaevskii equation (3.79) is the *imaginary-time* method reviewed in [44]. We know that any state $\phi(x, t)$ can be decomposed in a basis of the eigenvectors⁴ $\{\varphi_i\}$ of the Hamiltonian (3.28) that here is approximated by equation (3.79):

$$\phi = \sum_i c_i \varphi_i \quad \text{with} \quad c_i \in \mathbb{C}, H_{GP} \varphi_i = E_i \varphi_i \quad (3.89)$$

The wavefunction evolves as

$$\begin{aligned} \phi(x, t) &= e^{-iH_{GP}t} \phi(x, 0) = \sum_j e^{-itE_j} c_j \varphi_j(x) \\ &= e^{-itE_0} \left[c_0 \varphi_0(x) + \sum_{j>0} e^{-it(E_j - E_0)} c_j \varphi_j(x) \right] \end{aligned} \quad (3.90)$$

⁴We formally introduce the eigenvectors of the Hamiltonian (3.28) although they correspond to excited states that we ignored from the beginning. Actually, the excited states exponentially disappear with this method.

By defining $\tau = it$, we see that for $\tau \rightarrow \infty$, the sum in the brackets will exponentially be negligible with respect to $c_0\varphi_0$ since $E_j > E_0$ thus

$$\phi(x, -i\tau) = e^{-\tau E_0} c_0 \varphi_0(x) + \mathcal{O}(e^{-2\tau}) \quad (3.91)$$

and we see that the last term becomes negligible for $\tau \gg 1$.

Besides, the evolution is not unitary anymore with the redefinition $it \rightarrow \tau$ since $e^{-\tau H_{GP}}$ is not a unitary operator. The evolution is then given by

$$\partial_\tau \phi(x, -i\tau) = -H_{GP} \phi(x, -i\tau) \quad (3.92)$$

We implemented an algorithm, whose pseudocode is shown in [Alg.1], to solve equation (3.92) starting from an initial state to the lowest energy-state. It requires a routine that we name “GP”, to calculate the Hamiltonian that is used to compute the next time-step:

$$\begin{aligned} \phi_{\tau+d\tau} &= e^{-H_{GP}d\tau} \phi_\tau \\ &= \phi_\tau - H_{GP} \phi_\tau d\tau + \mathcal{O}((d\tau)^2) \end{aligned} \quad (3.93)$$

Algorithm 1 Imaginary-time algorithm

```

1: Pick initial, normalized state  $\phi_{\text{old}} = \varphi(0)$ , convergence limit  $\epsilon$  and time-step  $d\tau$ 
2: while true:
3:    $\phi_{\text{new}} \leftarrow \text{dop853}(\text{GP}(\tau, \phi_{\text{old}}), \tau + d\tau)$ 
4:    $\phi_{\text{new}} \leftarrow \frac{\phi_{\text{new}}}{\sum |\phi_{\text{new}}|^2}$ 
5:    $\delta_r \leftarrow |\max(|\phi_{\text{new}}|^2) - \max(|\phi_{\text{old}}|^2)| / \max(|\phi_{\text{new}}|^2)$ 
6:   if  $\delta_r < \epsilon$  :
7:     break
8:   endif
9:    $\phi_{\text{old}} \leftarrow \phi_{\text{new}}$ 
10: end while
11:  $\phi_{\text{new}} \leftarrow e^{-H(\phi_{\text{new}})d\tau} \phi_{\text{new}} = e^{-E_0 d\tau} \phi_{\text{new}}$ 
12:  $E_0 = -\frac{\ln \|\phi_{\text{new}}\|}{d\tau}$ 
13: returns  $E_0, \phi_{\text{new}}$ 

```

if the condition⁵ $E_{\text{max}} d\tau \ll 1$ is satisfied. Starting from an arbitrary ϕ_{old} , the state occupied by the system tends to an eigenvector of the Hamiltonian associated to the lowest eigenvalue when $\tau \gg 1$. In this regard the last ϕ_{old} obtained is an eigenstate

⁵The routine dop853 comes from a preexisting Python library. The criteria of convergence of the algorithm is dictated by this method. Before trying to find it in the documentation of this routine we made our own assumption that lies on a physical criteria which is simply $E_0 d\tau \ll 1$. The perfect agreement with the self-consistent method and the analytical results ensured us that our assumption was correct.

with a good approximation. Therefore we find

$$\phi_{\text{new}}^{(i)} = e^{-Hd\tau} \phi_{\text{old}}^{(i)} = e^{-E_0 d\tau} \phi_{\text{old}}^{(i)}. \quad (3.94)$$

By taking the absolute squared then summing over the positions, i.e. over the index i and since $\sum_i |\phi_{\text{old}}^{(i)}|^2 = 1$, we have⁶

$$\|\phi_{\text{new}}\|^2 = e^{-2E_0 d\tau} \quad (3.95)$$

thus

$$E_0 = -\frac{\ln \|\phi_{\text{new}}\|}{d\tau}. \quad (3.96)$$

Since ϕ_{new} is in good approximation the eigenstate of H_{GP} associated to the eigenvalue E_0 , we conclude that $E_0 = \mu$.

Self-consistent method

The second method used to solve the Gross-Pitaevskii equation (3.78) is the self-consistent method. Its pseudocode is presented in [Alg.2]. It is an iterative procedure. The state $\phi^{(n)}$ – the exponent in parentheses indicates the step of the procedure – permits to compute $\phi^{(n+1)}$. From equation (3.79), we insert $\phi^{(n)}$ in the Hamiltonian as follows:

$$H_{GP}(\phi^{(n)}) = \begin{pmatrix} \ddots & \ddots & \ddots & & \\ & -J & W(\phi_{i-1}^{(n)}, i-1) & -J & \\ & & -J & W(\phi_i^{(n)}, i) & -J \\ & & & -J & W(\phi_{i+1}^{(n)}, i+1) & -J \\ & & & & \ddots & \ddots & \ddots \end{pmatrix} \quad (3.97)$$

where $W(\phi_i^{(n)}, i) \equiv \frac{V_0 \ell^2}{2} (i - \frac{N_x}{2})^2 + U |\phi_i^{(n)}|^2$. In order to find $\phi^{(n+1)}$ and its associated eigenvalue $E_0^{(n+1)}$, we simply compute the lowest state and eigenvalue of the matrix above. We then input this state in (3.97) and compute again the lowest eigenvalue and eigenstate. We repeat this process until the (relative) difference between the maxima of two successive densities is lower than a threshold ϵ . In figure 3.3 we show that both imaginary-time and the self-consistent methods converge by plotting all the values taken by the quantity $\delta_r / \max(\delta_r)$ during the processes for $U = 10^{-5}$, $N = 10^4$, $V_0 = 5 \times 10^{-5}$. Note that $\phi^{(n)}$ is in good approximation the eigenstate of H_{GP}

⁶Note that the constant c_0 was dropped during the normalization step.

associated to the eigenvalue E_0 and we conclude that $E_0 = \mu$. Again this is confirmed by the results in figure 3.5.

Algorithm 2 Self-consistent algorithm

```

1: Pick initial, normalized state  $\phi_{\text{old}} = \varphi^{(n=0)}$ , convergence limit  $\epsilon$ .
2: while true:
3:    $\phi^{(n)} \leftarrow$  eigenvector associated to lowest energy of  $H(\phi^{(n-1)})$ 
4:    $\phi^{(n)} \leftarrow \frac{\phi^{(n)}}{\sum |\phi^{(n)}|^2}$ 
5:    $\delta_r \leftarrow |\max(|\phi^{(n)}|^2) - \max(|\phi^{(n-1)}|^2)| / \max(|\phi^{(n)}|^2)$ 
6:   if  $\delta_r < \epsilon$  :
7:     break
8:   endif
9:    $\phi^{(n-1)} \leftarrow \phi^{(n)}$ 
10: end while
11:  $E_0 \leftarrow$  lowest energy of  $H(\phi^{(n)})$ 
12:  $\phi^* \leftarrow$  eigenvector associated to  $E_0$ 
13: returns  $E_0, \phi^*$ 

```

3.2.3 Comparison of the imaginary-time and the self-consistent methods with analytical results

In this section we compare the imaginary-time and the self-consistent methods introduced in the two previous subsections. We computed the density profiles for different values of the interacting parameter U while keeping the other parameters, N and V_0 , fixed. We take the hopping matrix element J as our unit of energy and a as our unit of distance, and hereafter set $J = a = 1$ throughout. We will reintroduce them in the calculations to understand how they intervene in the matrix of the Hamiltonian. The plot in figure 3.4 shows the excellent agreement between the two methods. We note the expected broadening of the curves with the increase of U . In parallel, we computed the chemical potential as a function of U as shown in figure 3.5. Again, we find good agreement. We also compare μ to the derivative of the energy functional with respect to N , $\frac{\partial E}{\partial N}$ and to its asymptotic behaviour in the TF regime – see (3.44). In the same figure we see that they all match very well.

Finally we compare the numerical results with other analytical expressions in the non-interacting ($U = 0$) and in the TF regimes to test the validity of our algorithms. In the continuum, if $U = 0$ the interacting energy vanishes and, as stated in section 3.1.1, the wave function is a Gaussian. In the discrete case if the wave function is sufficiently broad, the discretization of the system is not unnoticeable meaning that the particles in the lowest energy state behave as in the continuum, except that the mass is renormalized by the band curvature. The difference between

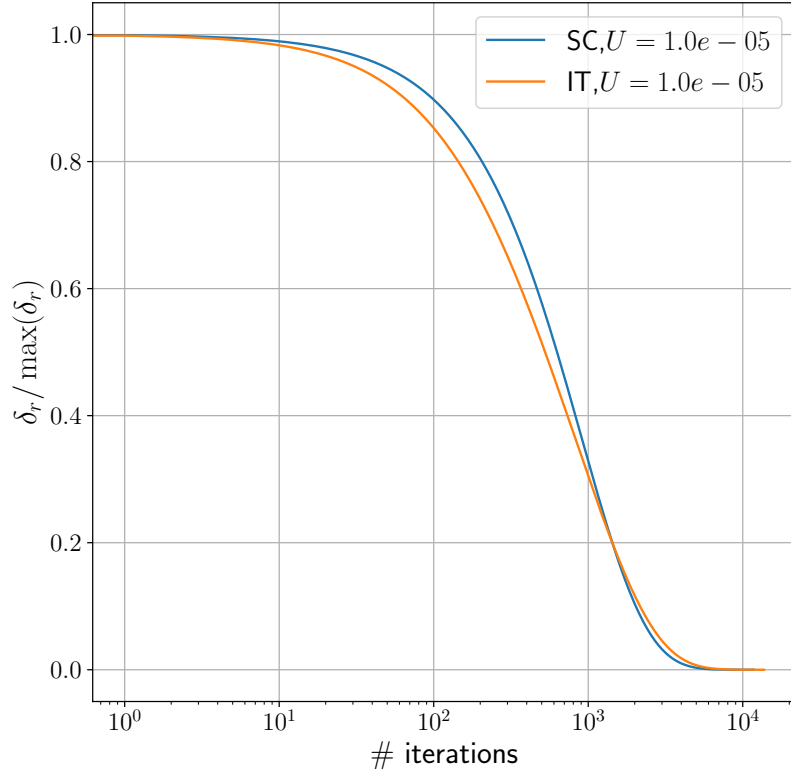


Figure 3.3: Evolution of the relative error between the maxima of two successive intermediate solutions of the Gross-Pitaevskii equations computed with the self-consistent (blue) and the imaginary-time (orange) methods for $U = 10^{-5}$, $N = 10^4$, $V_0 = 5 \times 10^{-5}$.

(3.82),(3.83) and their integral counterparts is therefore negligible apart from the shift $2J$ appearing on the kinetic energy. This statement is supported by the figure 3.6 that shows the good agreement between the two algorithms and the relations (3.82) and (3.83). Besides we are able to adapt for the discrete case the relations between N, μ, R and V_0 derived beforehand in the sections 3.1.4 and 3.1.5 when the interactions are taken into account. The equations (3.46) and (3.47) still hold if we shift μ by $2J$ and we are able to derive the same relations between the energy contributions and μ – see (3.48), (3.49). The comparison between these analytical expressions and the numerical results are presented in figure 3.7 where we observe excellent agreement once again.

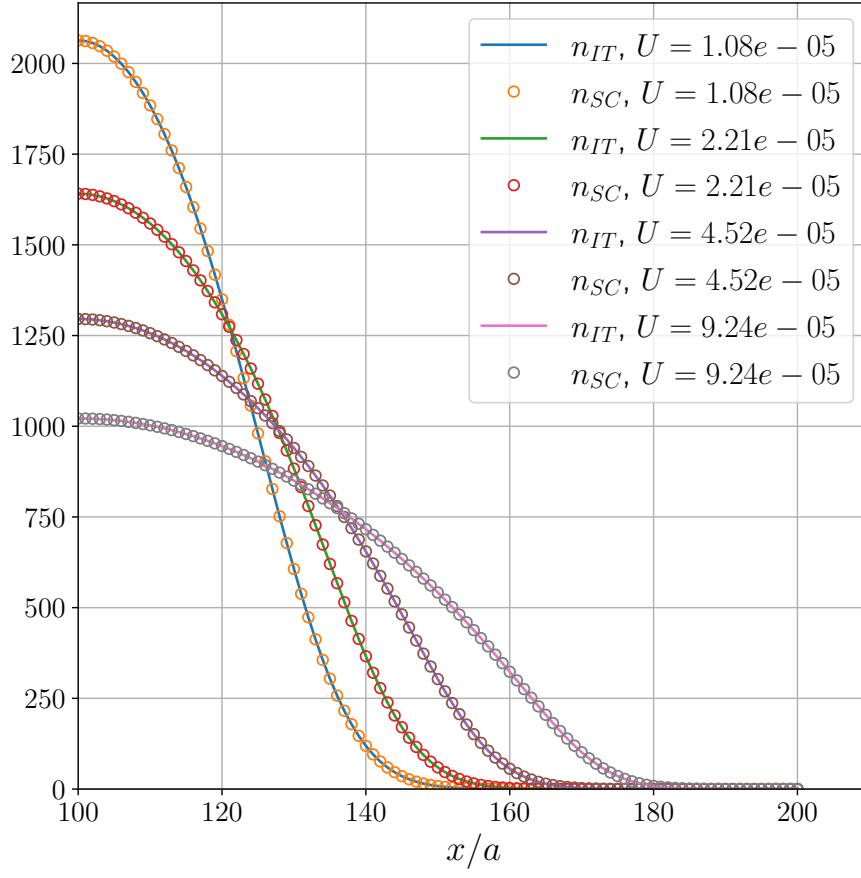


Figure 3.4: Comparison between densities obtained with the imaginary-time and self consistent methods for different values of U , $N = 10^5$ and $V_0 = 3.5 \times 10^{-5}$.

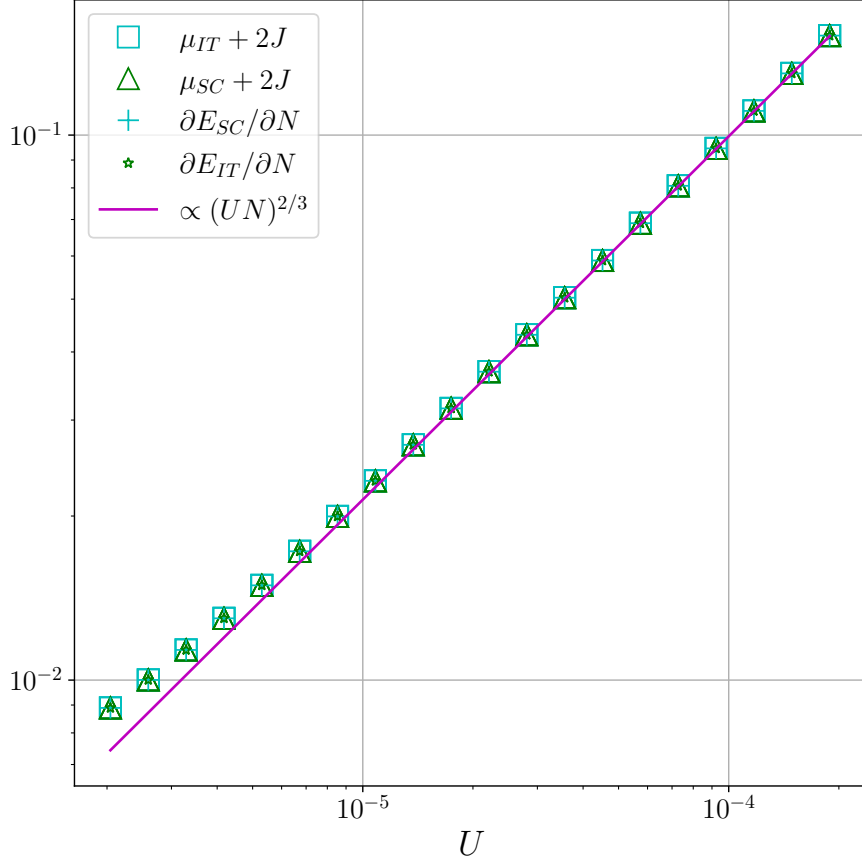


Figure 3.5: Comparison of the chemical potential as a function of U computed with the self-consistent and imaginary-time methods, for $V_0 = 3.5 \times 10^{-5}$ and $N = 10^5$. The numerical results are in agreement with the analytical predictions (3.44) in the TF regime. We also compare both chemical potentials to $\partial E / \partial N(N) = E(N+1) - E(N)$ where the energy functional has been computed with both methods.

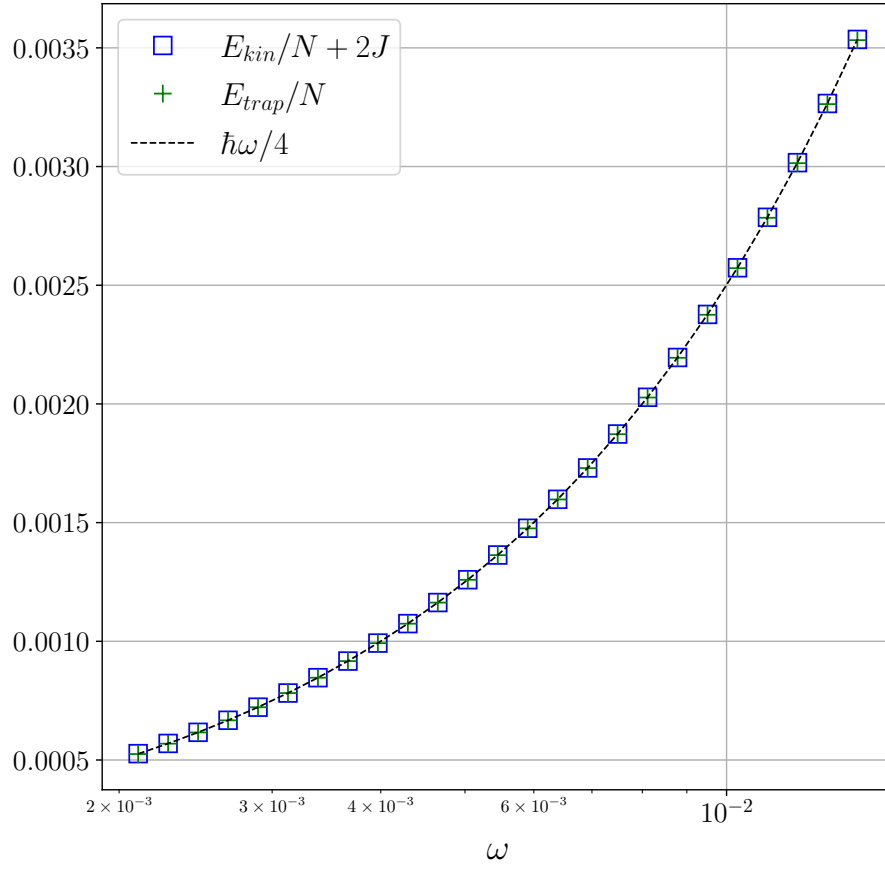


Figure 3.6: Evolution of the energy contributions in function of $\omega = \sqrt{V_0/m}$ computed with the self-consistent method. The numerical results are in agreement with the analytical predictions for $U = 0$ and $N = 10^4$ (non-interacting BEC) in equation (3.11).

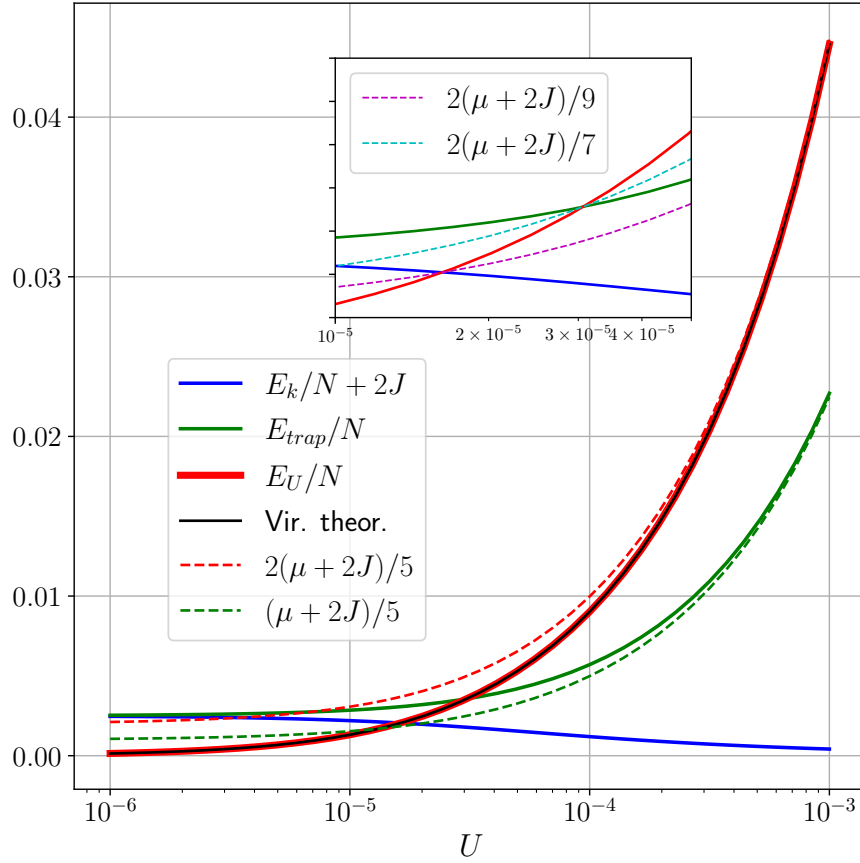


Figure 3.7: Evolution of the energy contributions as a function of U computed with the self-consistent method for a weakly interacting BEC in a 1D lattice, for $N = 10^4$ and $V_0 = 5 \times 10^{-5}$. The numerical results are in agreement with the analytical predictions for $E_U = E_{\text{kin}}$, $E_U = E_{\text{trap}}$ and at high values of U (Thomas-Fermi regime) as well.

Chapter 4

Relativistic Landau levels from a Fermi-Bose mixture

As we emphasized from the beginning of this thesis our ultimate goal is to construct a model of ultracold atoms that simulates strain on a honeycomb lattice in order to produce pseudo-Landau levels. The main goal of this chapter is to present a new strategy of Landau levels simulation in a honeycomb lattice. We are going to use a mixture of two species of ultracold atoms in such a way that this new system mimics the effect of linear strain discussed in chapter 2 instead of using sophisticated laser configurations as done in [34]. Inspired by the preexisting literature on correlated hopping [26, 45–47] we will make the hopping parameters of this new system linearly dependent on one space coordinate thus effectively realizing linear strain. We start by solving the Gross-Pitaevskii equation in the honeycomb lattice with a ribbon geometry. We then present the model that will reproduce strain and see how to mathematically manipulate the correlated-hopping coefficients to recover a linear dependence. Then we present the spectrum and discuss different features that take place. In the end we discuss the modifications of the spectrum once we go away from the Thomas-Fermi regime.

4.1 Numerical solution of Gross-Pitaevskii equation in a honeycomb lattice with a ribbon geometry

We start by studying a BEC in a honeycomb lattice and we perform a similar analysis to the one presented in the previous chapter for a 1D chain. Here we solve the Gross-Pitaevskii equation and calculate the density profile of the bosons that will contribute to the simulation of strain in the second part of the chapter. The Hamiltonian corresponding to this system looks like (3.71) except of course for the

hopping term that is now adapted to a honeycomb geometry:

$$\begin{aligned} \hat{H} = & -J \sum_{\mathbf{r} \in A, j} \left(\hat{a}_{\mathbf{r}}^\dagger \hat{b}_{\mathbf{r}+\boldsymbol{\delta}_j} + \hat{b}_{\mathbf{r}+\boldsymbol{\delta}_j}^\dagger \hat{a}_{\mathbf{r}} \right) + \sum_{\mathbf{r} \in A} \left[\frac{V_0}{2} \left(x - \frac{L_x}{2} \right)^2 \hat{a}_{\mathbf{r}}^\dagger \hat{a}_{\mathbf{r}} + \frac{U}{2} \hat{a}_{\mathbf{r}}^\dagger \hat{a}_{\mathbf{r}}^\dagger \hat{a}_{\mathbf{r}} \hat{a}_{\mathbf{r}} \right] \\ & + \sum_{\mathbf{r} \in B} \left[\frac{V_0}{2} \left(x - \frac{L_x}{2} \right)^2 \hat{b}_{\mathbf{r}}^\dagger \hat{b}_{\mathbf{r}} + \frac{U}{2} \hat{b}_{\mathbf{r}}^\dagger \hat{b}_{\mathbf{r}}^\dagger \hat{b}_{\mathbf{r}} \hat{b}_{\mathbf{r}} \right] \end{aligned} \quad (4.1)$$

where $\mathbf{r} = (x, y)$, $\boldsymbol{\delta}_1 = (-1, 0)$, $\boldsymbol{\delta}_2 = \left(\frac{1}{2}, \frac{\sqrt{3}}{2}\right)$ and $\boldsymbol{\delta}_3 = \left(\frac{1}{2}, -\frac{\sqrt{3}}{2}\right)$, U is the intensity of the repulsive interaction ($U \geq 0$) between two bosons, N_x (N_y) is the number of sites in the x (y) direction and V_0 is a parameter related to the frequency of the harmonic trap imposed along x . Enforcing periodic boundary conditions along y allows us to replace the operators \hat{a}, \hat{b} and their respective hermitian conjugates using the Fourier transformation presented in [A](#). Substituting into (4.1) we obtain

$$\begin{aligned} \hat{H} = & -J \sum_{x \in A, k_y} \left[\hat{a}_{x, k_y}^\dagger \left(\sum_j e^{ik_y \delta_{j,y}} \hat{b}_{z_j, k_y} \right) + h.c. \right] + \frac{V_0}{2} \sum_{x \in A, k_y} \left(x - \frac{L_x}{2} \right)^2 \hat{a}_{x, k_y}^\dagger \hat{a}_{x, k_y} \\ & + \frac{V_0}{2} \sum_{x \in B, k_y} \left(x - \frac{L_x}{2} \right)^2 \hat{b}_{x, k_y}^\dagger \hat{b}_{x, k_y} + \frac{U}{2N_y} \sum_{\substack{x \in A \\ k_y^1, k_y^2, k_y^3, k_y^4}} \delta_{k_y^1 + k_y^2, k_y^3 + k_y^4} \hat{a}_{x, k_y^1}^\dagger \hat{a}_{x, k_y^2}^\dagger \hat{a}_{x, k_y^3} \hat{a}_{x, k_y^4} \\ & + \frac{U}{2N_y} \sum_{\substack{x \in B \\ k_y^1, k_y^2, k_y^3, k_y^4}} \delta_{k_y^1 + k_y^2, k_y^3 + k_y^4} \hat{b}_{x, k_y^1}^\dagger \hat{b}_{x, k_y^2}^\dagger \hat{b}_{x, k_y^3} \hat{b}_{x, k_y^4}, \end{aligned} \quad (4.2)$$

where we defined $z_j \equiv x + \delta_{j,x}$, $x \in A$ and L_x is the size of the system along x , related to N_x by $L_x = 3N_x/2$. Regarding the conditions discussed in section [3.21](#), we apply the mean-field approximation $\hat{a}_{x, k_y} = \Psi_A(x, k_y) + \delta \hat{a}$ and $\hat{b}_{x, k_y} = \Psi_B(x, k_y) + \delta \hat{b}$ and neglect the fluctuations:

$$\begin{aligned}
E[\Psi] = & -J \sum_{x \in A, k_y} \left[\Psi_A^*(x, k_y) \left(\sum_j e^{ik_y \delta_{j,y}} \Psi_B(z_j, k_y) \right) + h.c. \right] \\
& + \frac{V_0}{2} \sum_{x \in A, k_y} \left(x - \frac{L_x}{2} \right)^2 \Psi_A^*(x, k_y) \Psi_A(x, k_y) \\
& + \frac{V_0}{2} \sum_{x \in B, k_y} \left(x - \frac{L_x}{2} \right)^2 \Psi_B^*(x, k_y) \Psi_B(x, k_y) \\
& + \frac{U}{2N_y} \sum_{\substack{x \in A \\ k_y^1, k_y^2, k_y^3, k_y^4}} \delta_{k_y^1 + k_y^2, k_y^3 + k_y^4} \hat{\Psi}_A^*(x, k_y^1) \Psi_A^*(x, k_y^2) \Psi_A(x, k_y^3) \Psi_A(x, k_y^4) \\
& + \frac{U}{2N_y} \sum_{\substack{x \in B \\ k_y^1, k_y^2, k_y^3, k_y^4}} \delta_{k_y^1 + k_y^2, k_y^3 + k_y^4} \Psi_B^*(x, k_y^1) \Psi_B^*(x, k_y^2) \Psi_B(x, k_y^3) \Psi_B(x, k_y^4),
\end{aligned} \tag{4.3}$$

Let us remind that the system is periodic in the y direction. The repeated structure along the y -direction – presented in figure 2.3 – is composed of two rows of unit cells. It is then useful to renormalise the field by the length of the system along y . Let us define $\Psi \rightarrow \sqrt{NN_y} \phi$ and assume that the condensed bosons occupy the lowest energy state – namely $k_y = 0$ – we then find

$$\begin{aligned}
\frac{E[\phi_A, \phi_B]}{NN_y} = & -J \sum_{x \in A} \left[\phi_A^*(x) \left(\sum_j \phi_B(z_j) \right) + h.c. \right] + \frac{V_x}{2} \sum_{x \in A} \left(x - \frac{L_x}{2} \right)^2 |\phi_A(x)|^2 \\
& + \frac{V_x}{2} \sum_{x \in B} \left(x - \frac{L_x}{2} \right)^2 |\phi_B(x)|^2 + \frac{U}{2} \sum_{x \in A} |\phi_A(x)|^4 + \frac{U}{2} \sum_{x \in B} |\phi_B(x)|^4,
\end{aligned} \tag{4.4}$$

where N is the total number of particles in the cloud. Again, we derive the equations of motion for this system, taking into account only the stationary solutions. Deriving each energy contribution with respect to ϕ_A^* and ϕ_B^* we obtain

$$\begin{aligned}
\left. \frac{\delta E_{\text{kin}}}{\delta \phi_A^*(z)} \right|_{z=x} &= -J \sum_j \phi_B(x + \delta_{x,j}) \\
\left. \frac{\delta E_{\text{pot}}}{\delta \phi_A^*(z)} \right|_{z=x} &= \frac{V_0}{2} x^2 \phi_A(x) \\
\left. \frac{\delta E_{\text{int}}}{\delta \phi_A^*(z)} \right|_{z=x} &= U |\phi_A(x)|^2 \phi_A(x) \\
\left. \frac{\delta E_{\text{kin}}}{\delta \phi_B^*(z)} \right|_{z=x+\delta_{i,x}} &= -J \sum_j \phi_A(x + \delta_{x,i} - \delta_{x,j}) \\
\left. \frac{\delta E_{\text{pot}}}{\delta \phi_B^*(z)} \right|_{z=x+\delta_{i,x}} &= \frac{V_0}{2} (x + \delta_{x,i})^2 \phi_B(x + \delta_{x,i}) \\
\left. \frac{\delta E_{\text{int}}}{\delta \phi_B^*(z)} \right|_{z=x+\delta_{i,x}} &= U |\phi_B(x + \delta_{x,i})|^2 \phi_B(x + \delta_{x,i}),
\end{aligned} \tag{4.5}$$

Therefore the equation of motion is

$$\begin{cases} -J \sum_j \phi_B(z_j) + \frac{V_0}{2} \left(x - \frac{L_x}{2} \right)^2 \phi_A(x) + U |\phi_A(x)|^2 \phi_A(x) = \mu \phi_A(x) \\ -J \sum_j \phi_A(z_i - \delta_{x,j}) + \frac{V_0}{2} \left(z_i - \frac{L_x}{2} \right)^2 \phi_B(z_i) + U |\phi_B(z_i)|^2 \phi_B(z_i) = \mu \phi_B(z_i) \end{cases} \tag{4.6}$$

for every position x in the sublattice A , $z_j \equiv x + \delta_{j,x}$ ¹ and μ the chemical potential – appearing in place of the energy, see section 3.1.3. As we did in section 3.2.1 we rewrite the system (4.6) into the eigenvalue equation $H_{GP}\phi = \mu\phi$ where

$$H_{GP} = \begin{pmatrix} \ddots & \ddots & \ddots & & & & \\ & -J & W(\phi_A, x) & -2J & & & \\ & & -2J & W(\phi_B, z_j) & -J & & \\ & & & -J & W(\phi_A, z_j + 1) & -2J & \\ & & & & \ddots & \ddots & \ddots \end{pmatrix}. \tag{4.7}$$

The solution to the Gross-Pitaevskii equation (4.6) is calculated with the self-consistent method². As we did in the section 3.2.3, we compare the results with

¹For the sake of clarity, in (4.6), we didn't replace x or z_j by their coordinate in the basis $\{\mathbf{a}_1, \mathbf{a}_2\}$ as we did for the 1D case. Since we have a space dependence due to the harmonic trap that requires the exact position of the site, putting only the indices in the basis $\{\mathbf{a}_1, \mathbf{a}_2\}$ wouldn't have been correct. Indeed an A and a B sites can have the same index as shown in figure A.1. For this reason we will stick to the exact space-coordinate.

²Since we proved in section 3.2.3 that the two methods are in very good agreement with each

analytical ones. A notable difference is the shift to apply on the chemical potential in the continuum. Indeed in the 1D lattice a shift of $+2J$ was added to the chemical potential in continuum. Here this shift adds up to $3J$ because of the difference between the 2D honeycomb dispersion and the one of a 1D chain. The figure 4.1 reveals the good agreement between numerical and analytical results as their ‘1D-counterparts’ did. In figure 4.2 we show that when U is increased the density profile flattens, similarly to the behavior that we have already seen for the 1D chain, see figure 3.2.

4.2 Correlated hoppings and the Landau levels

The system we are now going to discuss is a mixture of fermions and bosons at $T = 0$ K that we will symbolize with \downarrow and \uparrow respectively. We will exploit this setup to simulate the physics of Landau levels. Differently from other approaches where strain is obtained by deforming the system, here we will generate space-dependent hopping coefficients through the interactions of fermions with a non-uniform gas of bosons. The main ingredients of our scheme involve:

- An optical lattice with a honeycomb geometry;
- Trapped bosons (\uparrow) that are repulsively interacting and that hop on the nearest neighbor sites of the honeycomb lattice. They are also trapped by a harmonic potential along the x -direction. As we wrote earlier we benefit of an important controllability in the present system which makes possible to have a dominant contribution of the harmonic confinement along the x -direction while we are neglecting harmonic confinement along the y -direction. The Hamiltonian for this subsystem then reads

$$\begin{aligned} \hat{H}_B = & -J \sum_{\mathbf{r} \in A, j} \left(\hat{a}_{\uparrow, \mathbf{r}}^\dagger \hat{b}_{\uparrow, \mathbf{r} + \boldsymbol{\delta}_j} + H.c. \right) + \sum_{\mathbf{r} \in A} \frac{V_x}{2} x^2 \hat{a}_{\uparrow, \mathbf{r}}^\dagger \hat{a}_{\uparrow, \mathbf{r}} + \sum_{\mathbf{r} \in B} \frac{V_x}{2} x^2 \hat{b}_{\uparrow, \mathbf{r}}^\dagger \hat{b}_{\uparrow, \mathbf{r}} \\ & + \frac{U}{2} \sum_{\mathbf{r} \in A} \hat{a}_{\uparrow, \mathbf{r}}^\dagger \hat{a}_{\uparrow, \mathbf{r}}^\dagger \hat{a}_{\uparrow, \mathbf{r}} \hat{a}_{\uparrow, \mathbf{r}} + \frac{U}{2} \sum_{\mathbf{r} \in B} \hat{b}_{\uparrow, \mathbf{r}}^\dagger \hat{b}_{\uparrow, \mathbf{r}}^\dagger \hat{b}_{\uparrow, \mathbf{r}} \hat{b}_{\uparrow, \mathbf{r}}. \end{aligned} \quad (4.8)$$

Section 4.1 has been dedicated to its analysis. Thanks to this analysis we figured out which ranges of parameters we should choose such that the Bose-Einstein condensate enters the Thomas-Fermi regime.

other for the 1D case and since the algorithm for the honeycomb lattice is not significantly different, we legitimately assumed that both methods would still be in good agreement as well.

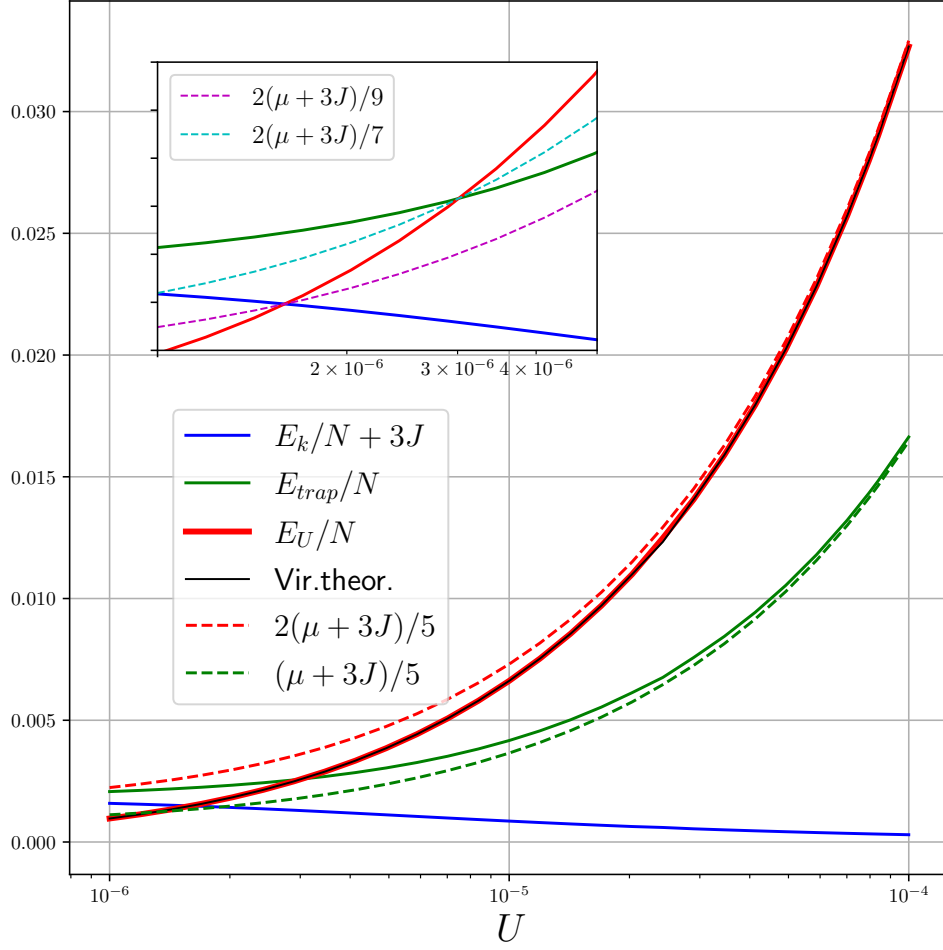


Figure 4.1: Evolution of the energy contributions as a function of U computed with the self-consistent method for a weakly interacting BEC in a honeycomb lattice, for $V_0 = 3.5 \times 10^{-5}$, $N = 10^5$. The numerical results are in agreement with the analytical predictions for $E_U = E_{\text{kin}}$, $E_U = E_{\text{trap}}$ and at high values of U (TF regime) as well.

- Fermions (\downarrow) that hop on the nearest neighbor sites of the honeycomb lattice. They do not interact³ with each other and their Hamiltonian reads

$$\hat{H}_F = -t \sum_{\mathbf{r} \in A, j} \hat{a}_{\downarrow, \mathbf{r}}^\dagger \hat{b}_{\downarrow, \mathbf{r} + \boldsymbol{\delta}_j} + h.c. \quad (4.9)$$

³In cold atoms the interparticle potential are often short-range which limits the interactions to be on-site in good approximation. Because of the Pauli principle fermions can not occupy the same energy state which prevents them to be at the same site of the lattice if we do not take into account internal degrees of freedom.

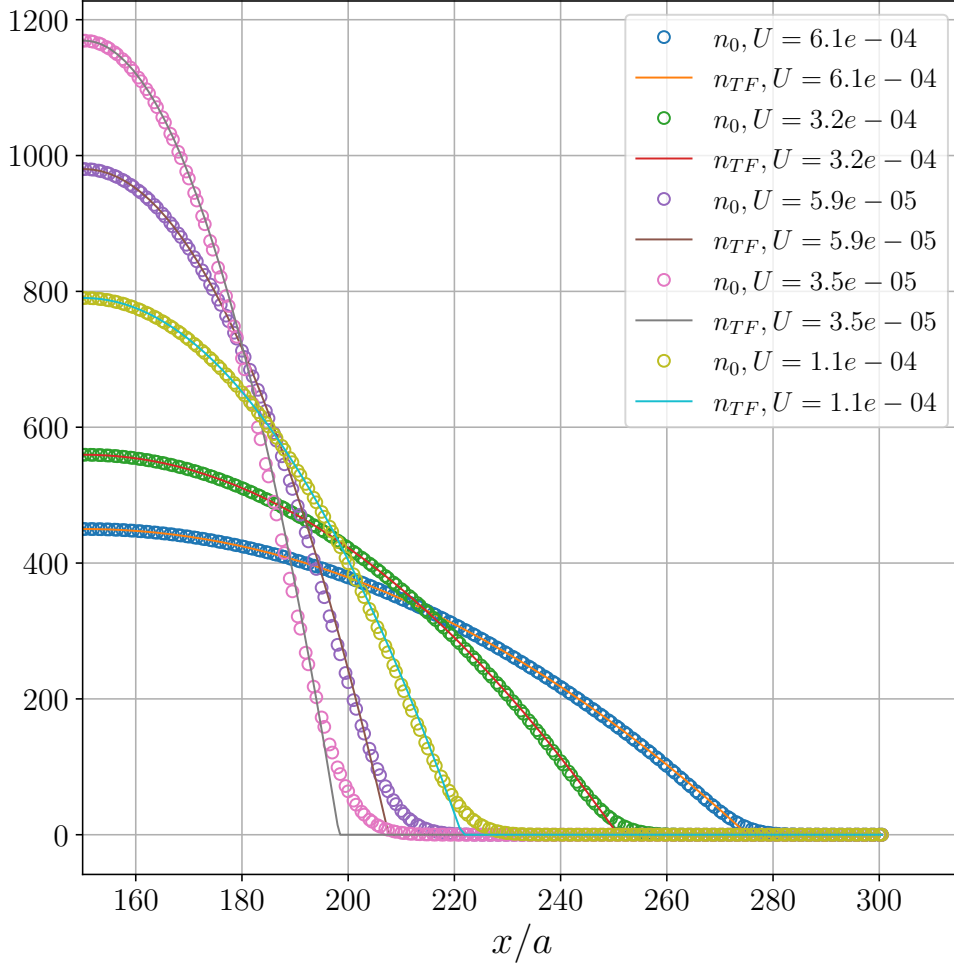


Figure 4.2: Densities of a weakly interacting BEC in a honeycomb lattice for various values of the interaction parameter U and fixed N, V_0 . They are compared to the TF densities with the same parameters. The agreement is better as U increases.

The section 2.1.2 was devoted to the study of the spectrum of this Hamiltonian and we later discussed the effect of strain in order to generate a pseudomagnetic field and Landau levels near the Dirac points.

- Interactions between fermions and bosons that manifest when a fermion hops to a neighbor sites and there is a non-vanishing occupation of bosons on the two sites. In particular, the interacting term that we propose to use has the form

$$\hat{H}_{BF} = \alpha t \sum_{\mathbf{r} \in A, j} \hat{a}_{\downarrow, \mathbf{r}}^\dagger (n_{\uparrow, \mathbf{r}} - n_{\uparrow, \mathbf{r} + \boldsymbol{\delta}_j}) \hat{b}_{\downarrow, \mathbf{r} + \boldsymbol{\delta}_j} + h.c. \quad (4.10)$$

where α is the constant that measures the strength of the density dependent hopping process. By assembling \hat{H}_F and \hat{H}_{BF} the hopping amplitude t_j for a fermion at position \mathbf{r} and tunnelling to $\mathbf{r} + \boldsymbol{\delta}_j$ – or vice-versa – is therefore given by

$$t_j(\mathbf{r}) = t \left[1 - \frac{\alpha}{3} (n_{\uparrow, \mathbf{r}} - n_{\uparrow, \mathbf{r} + \boldsymbol{\delta}_j}) \right] \quad j = 1, 2, 3. \quad (4.11)$$

Because of their dependence on the bosonic density they are commonly called *correlated* or *density-assisted hopping processes*. The reason of this specific combination of the density evaluated at neighbouring sites will be explained below.

We will also assume that the density of bosons at each site is fixed and the presence of fermions does not influence the behaviour of the bosons. In other words, once the bosonic gas occupies its equilibrium state it never leaves it despite the presence of the fermions. Bosons are then considered as a background by the fermions. This assumption is obviously not correct because the bosons can have a feedback from the fermions and it will be important to also analyze this effect. However this is beyond the scope of this thesis.

Recovering the linearity

Interestingly it is possible to recover a linear space-dependence of the hopping parameters in equation (4.11) when the bosonic gas is in the Thomas Fermi regime. Indeed, the bosonic density is an inverted parabola as a function of the position, except for the boundaries of the cloud. If we omit for a moment this problem at the edges of the cloud, the density is given by (3.39) when we impose a periodicity along the y -axis. Therefore, if the parabola is centered at the middle of the system in x_c , we obtain

$$\begin{aligned} n_{\text{TF}}(x) - n_{\text{TF}}(x - a) &= -\frac{V_0}{2U} [(x - x_c)^2 - (x - a - x_c)^2] = -\frac{V_0 a}{U} (x - x_c) + \frac{V_0 a^2}{2U}, \\ n_{\text{TF}}(x) - n_{\text{TF}}(x + a/2) &= -\frac{V_0}{2U} \left[(x - x_c)^2 - \left(x + \frac{a}{2} - x_c \right)^2 \right] = \frac{V_0 a}{2U} (x - x_c) + \frac{V_0 a^2}{8U} \end{aligned} \quad (4.12)$$

where the first expression is calculated for the link corresponding to $\boldsymbol{\delta}_1$ and the second one to $\boldsymbol{\delta}_2$ and $\boldsymbol{\delta}_3$. Both of these results are linear in x . The resulting

Hamiltonian⁴ is $\hat{H}_f = \hat{H}_F + \hat{H}_{BF}$:

$$\begin{aligned}
\hat{H}_f &= - \sum_{k_y} \hat{H}_f(k_y) \\
&= \sum_{x \in A, k_y} \left\{ \hat{a}_{x, k_y}^\dagger t \underbrace{\left[1 + \alpha \frac{V_0 a}{3U} (x - x_c) - \alpha \frac{V_0 a^2}{24U} \right]}_{t_1(x)} \hat{b}_{z_1, k_y} \right. \\
&\quad + \hat{a}_{x, k_y}^\dagger t \underbrace{\left[1 - \alpha \frac{V_0 a}{6U} (x - x_c) - \alpha \frac{V_0 a^2}{24U} \right]}_{t_2(x)} e^{ik_y \delta_{2,y}} \hat{b}_{z_2, k_y} \\
&\quad \left. + \hat{a}_{x, k_y}^\dagger t \underbrace{\left[1 - \alpha \frac{V_0 a}{6U} (x - x_c) - \alpha \frac{V_0 a^2}{24U} \right]}_{t_3(x)} e^{ik_y \delta_{3,y}} \hat{b}_{z_3, k_y} + h.c. \right\} \tag{4.13}
\end{aligned}$$

with $z_j \equiv x + \delta_j$ where we followed the same reasoning as in chapter 2 following the argument in Appendix A. Its matrix form is in every respect similar to (2.26) except for the specific form of the hopping parameters. We can obtain its spectrum by firstly computing the density of the BEC only, with the same code used in the section 4.1 and secondly by plugging the resulting density in (4.13) to obtain the spectrum and the eigenvectors of $\hat{H}_f(k_y)$.

To be as close as possible to the TF regime without neglecting the kinetic energy we learned in the section 3.1.4 that some ranges of values for the parameters U , N and V_0 are more convenient than others – see figure 3.2. Assuming that V and N are fixed, we choose a value of the parameter U such that it properly fits the TF density while it covers as much as possible the entire lattice. Indeed we want the artificial linear strain to be applied everywhere as it was previously the case for the mechanical strain. By taking $U = 10^{-3}$, $N = 10^5$, $V_0 = 3.5 \times 10^{-5}$ for a system of $L_x = 301.5$ sites – $E_{\text{kin}}/E_U = 0.0008$ – we find the density in figure 4.3. We will later see what happens when the BEC does not occupy all the sites of the lattice which is experimentally more realistic. In figure 4.3 we observe that the Thomas-Fermi density (in red) correctly fits the data except at the boundaries, which is expected from the discussion in the section 3.1.4. To end this section we present the figure 4.4 where we clearly distinguish the Landau levels. From equations (2.43) we deduce the energies of the pseudo-Landau levels for this specific case, where we added a linear dependence on x in t_2 and t_3 – unlike in section 2.4 where only t_1 depended

⁴For the sake of readability we removed the symbol \downarrow since we only talk about the fermions.

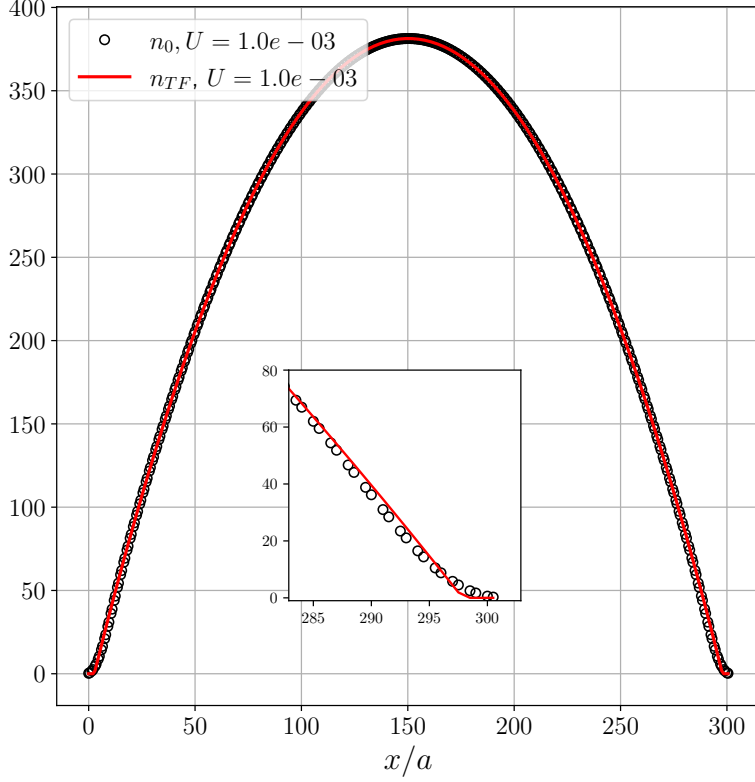


Figure 4.3: The density per particle of the cloud numerically computed (n_0) is globally well fitted by the Thomas-Fermi density. The parameters are: $\alpha = 0.1, U = 10^{-3}, N = 10^5, V_0 = 3.5 \times 10^{-5}$. Inset: zoom on the edge where the parabola.

on x . We then plotted in dashed black lines the tilted Landau levels whose energies are

$$E_j = \pm t a \sqrt{\frac{3}{2} j \alpha \frac{V_0}{U}} \sqrt{1 - q_y a} \quad j \in N. \quad (4.14)$$

Since they match very well we conclude that this model is suitable to recreate the physics of Landau levels.

4.3 Landau levels away from the Thomas-Fermi regime

As we mentioned earlier the boundaries of the cloud cause a deviation of the bosonic density from the parabola expected in the TF regime. In this section we are going to study what happens when we deviate even more from the TF regime.

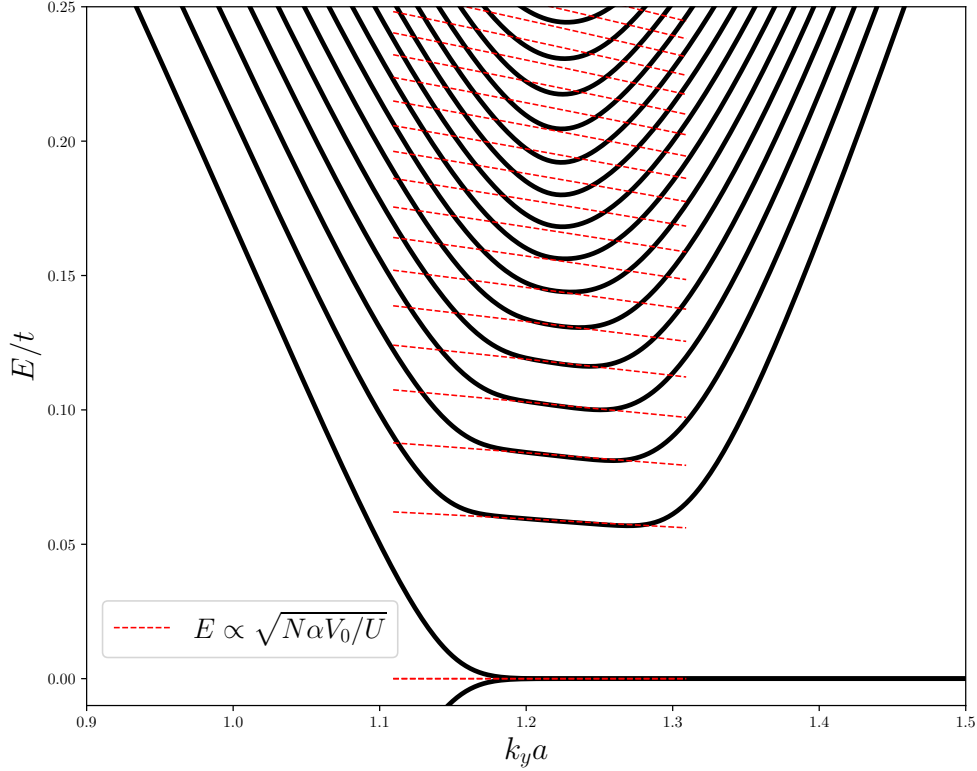


Figure 4.4: Spectrum of \hat{H}_f near one of the Dirac point for $L_x = 301.5, U = 10^{-3}, N = 10^5, V_0 = 3.5 \times 10^{-5}$. The lowest pseudo-Landau levels are well fitted by the analytical square-root law (4.14).

In order to go away from the TF regime, here below we decrease the strength of the interactions U while keeping all the other parameters fixed. We expect that reducing U will modify the spectrum. This is what we observe in figure 4.5, obtained for parameters $U = 10^{-4}, N = 10^5, V_0 = 3.5 \times 10^{-5}$ even if we are still in the TF regime ($E_{\text{kin}}/E_U \simeq 10^{-2}$) as shown in figure 4.1. We remark two important features. First the data are not well fitted by the TF density in comparison to the figure 4.3 at the boundaries. Secondly the density doesn't cover the entire system which leads to a zone where fermions would not interact with bosons. We will call it the *unstrained zone*. There are two main reasons for these effects:

1. Lowering U will decrease the size of the BEC-cloud as shown in figure 4.2. The part of the system where there is effectively an artificial strain is reduced with respect to the one for $U = 10^{-3}$. However from (4.14) we understand that decreasing U could result in a stronger strain which has the effect of enlarging and tilting the Landau levels, as we observed in figure 2.10.

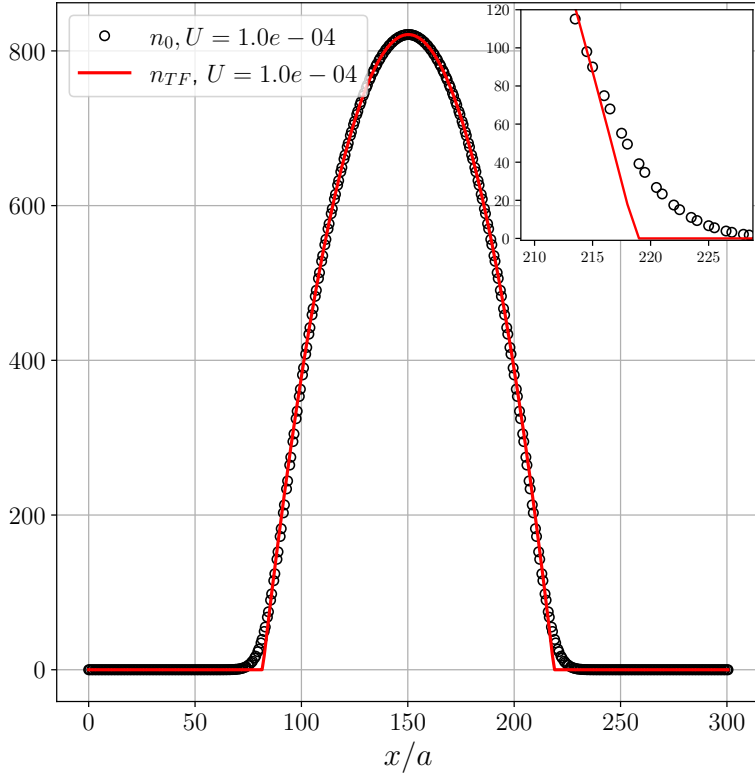


Figure 4.5: The density profile of the BEC n_0 numerically computed for $\alpha = 0.1, U = 10^{-4}, N = 10^5$ and $V_0 = 3.5 \times 10^{-5}$ is globally well fitted by the Thomas-Fermi density except at the edge of the cloud as shown by the inset what leads to noticeable nonlinearities. We also note that the clouds does not cover the entire system which lets a zone without interactions with bosons. Inset: zoom on the edge where the parabola showing a less good agreement between n_0 and n_{TF} than for $U = 10^{-3}$.

2. Decreasing U also makes the density of the BEC quit its parabolic shape first at the boundaries and progressively to the bulk. This results in supplementary non-linear terms in the correlated hopping thus breaking the assumption of linear strain near the edge of the cloud.

4.3.1 Presence of unstrained zones

The spectrum of \hat{H}_f for $\alpha = 0.1, U = 10^{-4}, V_0 = 1.0 \times 10^{-5}$ and $N = 10^5$ is shown in figure 4.6. Several new structures are visible. We remark a conical shape similar to the one encountered in the figure 2.5 that corresponded to a unstrained honeycomb lattice. We notice that the minima of subsequent energy levels alternatively shift to

the left and to the right in momentum space. We also note a superimposed spectrum presenting Landau levels. At $E = 0$ we see an additional bump that merges with the 0th Landau levels from around $k_y a = 1.3$ to $k_y a = 1.5$. Moreover we plotted in light gray the spectrum that we would have gotten if we had used the TF density in place of the numerical one and with which the hopping coefficient would have been linear in space. We note slight deviations between the two. To analyse this spectrum we are going to proceed step-by-step by separating the effects of the nonlinearities from those due to the presence of the unstrained zone.

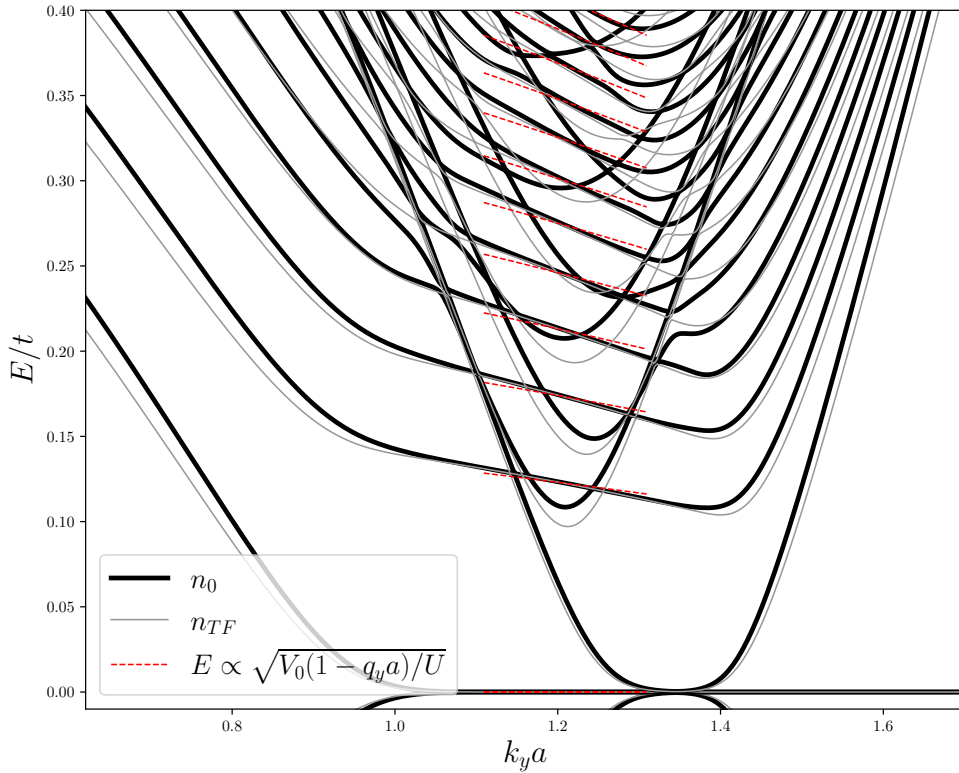


Figure 4.6: Spectrum of \hat{H}_f near a Dirac point for $L_x = 301.5a$, $\alpha = 0.1$, $U = 10^{-4}$, $V_0 = 1.0 \times 10^{-5}$ and $N = 10^5$.

Since we did not observe any deformations in figure 4.4 we can try to introduce by hand an unstrained zone in the system to figure out how the conical structure arises. This is simply done by increasing L_x without varying the other parameters such that the size of the cloud remains the same – as long as the boundaries of the system are placed sufficiently far from the center of the trap, where the density of bosons is negligible. By choosing $L_x = 601.5a$, $U = 10^{-3}$, $N = 10^5$, $V_0 = 3.5 \times 10^{-5}$ we obtain the density presented in figure 4.7 and the corresponding spectrum in

figure 4.8. Again we plotted in light gray the spectrum that we would have gotten if we had used the TF density in place of the numerical one. This shows, as expected, that the nonlinearities – absent if we use the TF density – are not perceptible in the present case.

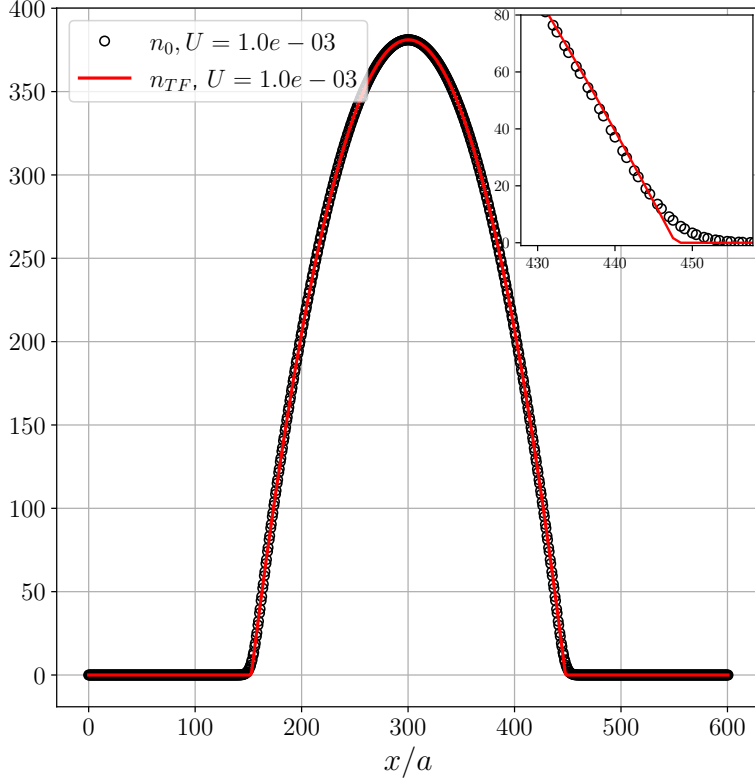


Figure 4.7: Density for $L_x = 601.5a$, $U = 10^{-3}$, $N = 10^5$, $V_0 = 3.5 \times 10^{-5}$. Only half of the system is strained.

4.3.2 Boundaries of the cloud and edge modes

An interesting question to ask is: *which part of the spectrum corresponds to which region of the system?* To answer it we simply compute the eigenvectors for every point of the spectrum and assign them a color as a function of the value of their mean positions. The results are shown in figures 4.9 and 4.10. In the first figure we see that the conical structure is spatially divided in two different subsystems, one to the left of the system (in blue) and the other one to the right (in pink). The second figure is complementary to the first one to distinguish if the eigenvectors are localized or not around the edges of the BEC cloud – these edges are near $\pm R/2$. The color gets warmer as the state gets closer to one of the edges.

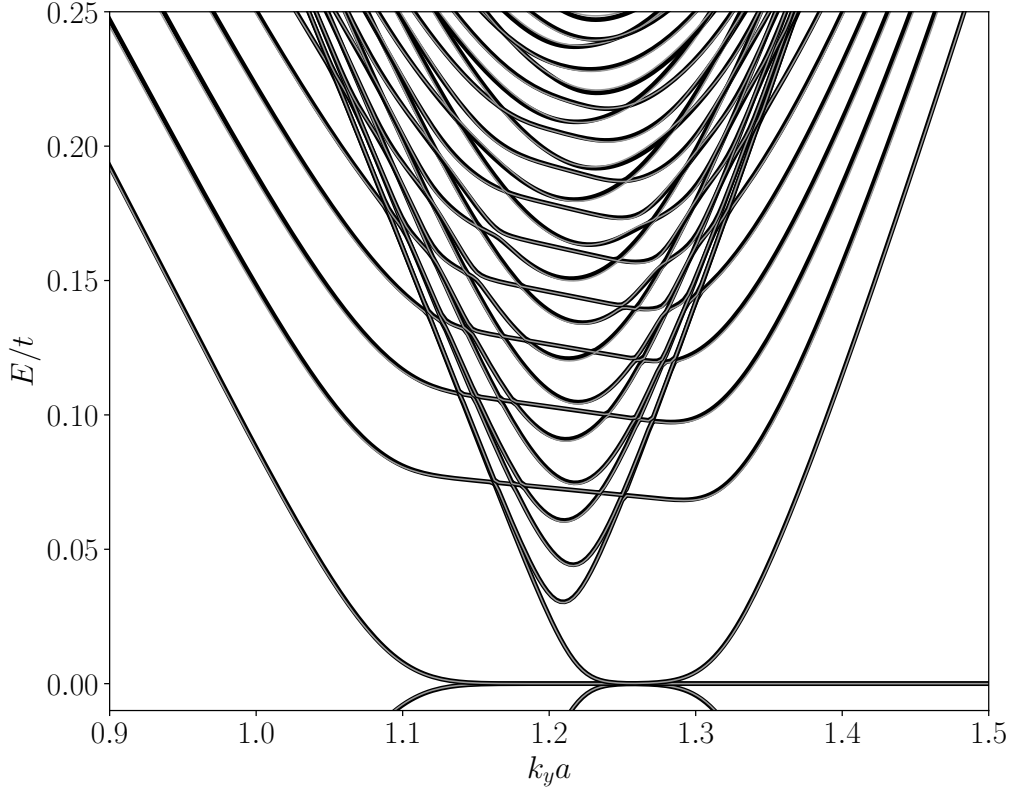


Figure 4.8: Spectrum of \hat{H}_f for $L_x = 601.5a, U = 10^{-3}, N = 10^5, V_0 = 3.5 \times 10^{-5}$. The spectra obtained with the numerical (black lines) and the TF (light gray) densities match perfectly. Two different spectra seem to be superimposed. The Landau levels are not deformed and are still in good accordance with the predictions (red lines).

By looking at figure 4.7 we see that the boson density does not cover all the system. To the left we have a zone whose length is about 160 sites that is not occupied by the bosons. By representing in figure 4.9 the spectrum of an unstrained system of size $L_x = 157.5a$ (dotted-dashed green line) and we note its perfect agreement with the light blue lines in the conical structure. Therefore, referring to the colour bar, the green lines predict very well the unstrained part to the left of the cloud. This reveals that, for these values of parameters, it looks like the system is a composition of three subsystems: fermions on an unstrained lattice to the left, a mixture in the middle (zone covered by the cloud) and again an unstrained lattice to the right. Furthermore we observe a shrinking of the Landau levels which is exhibited by the comparison with the spectrum computed for $L_x = 301.5a, U = 10^{-3}, V_0 = 3.5 \times 10^{-5}, N = 10^5, \alpha = 0.1$ indicated in dashed black line.

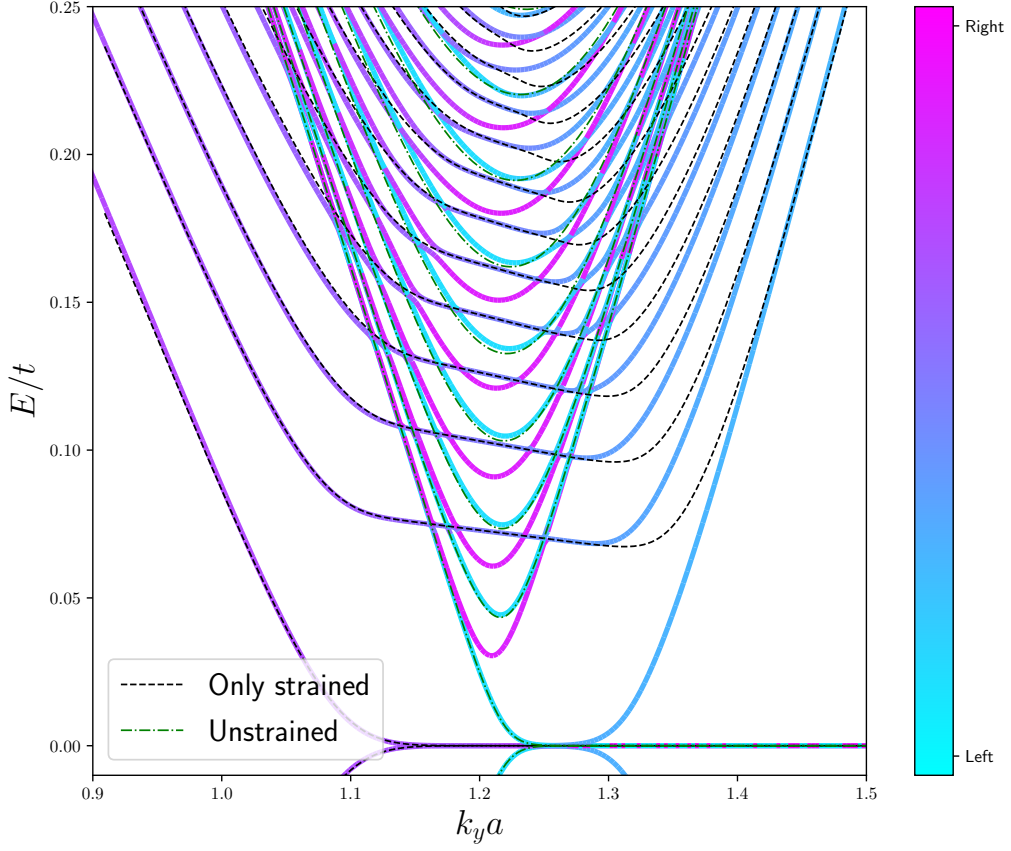


Figure 4.9: Spectrum of \hat{H}_f for $L_x = 601.5a$, $U = 10^{-3}$, $V_0 = 3.5 \times 10^{-5}$, $N = 10^5$, $\alpha = 0.1$.

From the figure 4.10 we deduce the presence of states localized at the edges of the cloud, as shown in the right subfigure in figure 4.11. This is expected from a system that displays Landau levels as we explained in section 1.1.2. The darker blue color of the Landau levels jointly with the blue color in figure 4.9 confirms that they are associated to bulk states – see subfigure in the lower left of figure 4.11 where we find the same result as in the left subfigure of the figure 2.9.

Noticeably when the size of the unstrained zone is large enough, what we will call *bumps* appear near the $E = 0$ energy visible for example in figure 4.10. The two bumps touch each other at $E = 0$ for values of $k_y a$ from around 1.2 to 1.3. By looking at the dashed lines which represent the spectrum of a system computed for $L_x = 301.5a$, $U = 10^{-3}$, $V_0 = 3.5 \times 10^{-5}$, $N = 10^5$, $\alpha = 0.1$, we see that the bump is not part of this spectrum meaning that this bump is not coming from the strained system, although the eigenvectors associated to the point that form the

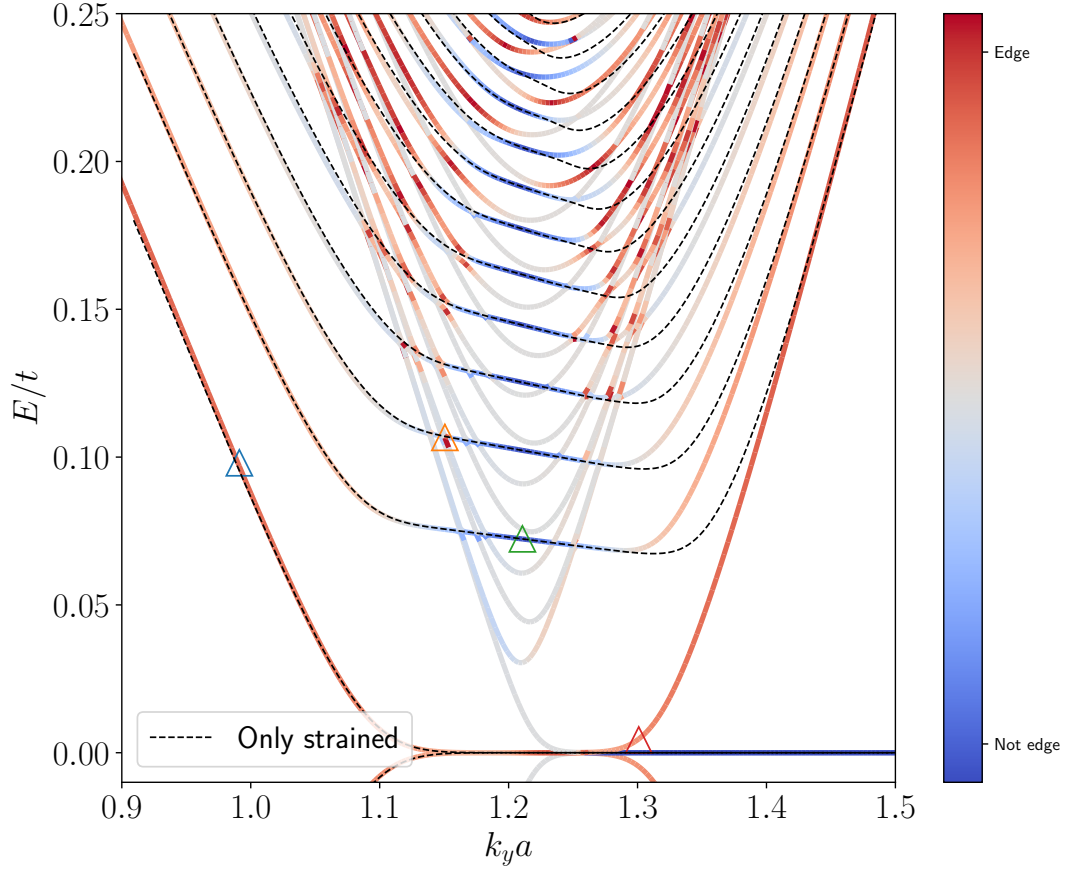


Figure 4.10: Spectrum of \hat{H}_f for $L_x = 601.5a$, $U = 10^{-3}$, $V_0 = 3.5 \times 10^{-5}$, $N = 10^5$, $\alpha = 0.1$. The color map indicates the values of the mean positions of the eigenvectors associated to each point of the spectrum. The warmer is the color the closer is the mean position to the edge. The eigenvectors corresponding to the triangles are presented in figure 4.11.

bumps are localized at the edge of the cloud – see lower-right subfigure in figure 4.11. Furthermore they do not come from the spectrum of the unstrained zones. This leads us to the conclusion that the bumps emerge from the reunion of these two type of subsystems. There must also be a hybridization that takes place.

Finally we look at the crossings between the Landau levels and the cones. Indicated by the blue triangle in figure 4.10 the corresponding eigenstate is presented in figure 4.11 in the upper-right subfigure. We don't see a clear localization but rather a composition of two states, one being out of the cloud (represented by the green line which is the density of the condensate) and another one almost entirely within the cloud. We suppose that a hybridization occurs at this crossing between two bulk

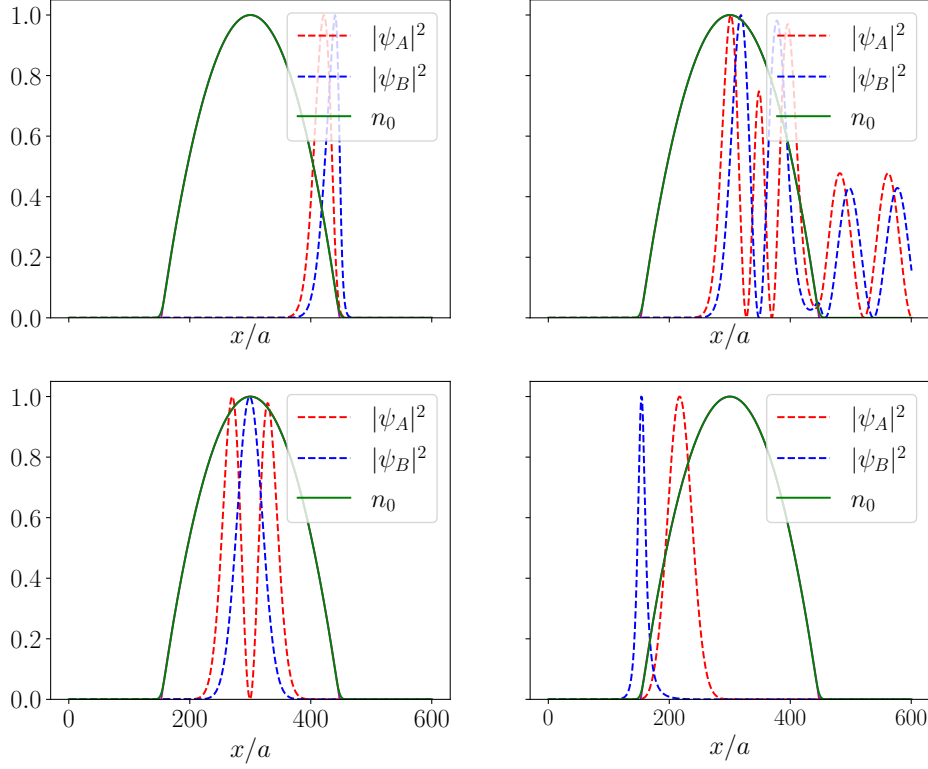


Figure 4.11: Eigenvectors of \hat{H}_f corresponding to the triangles in figure 4.10: upper-left: blue triangle, upper-right: orange triangle, lower-left: green triangle, lower right: red triangle.

states with two different origins: one comes from the Landau levels and the second one from the honeycomb lattice.

We end this discussion by noting the consequences of nonlinearities that take place if we start from the TF regime and we decrease U while keeping N and V_0 constant. Indeed the density profile n_0 is not properly fitted by the TF density anymore. This means that when U decreases, n_0 acquires a space-dependence different from a quadratic polynomial therefore the hopping coefficients do not vary linearly in space anymore. Hence the pseudo-magnetic field is not uniform anymore. For lower values of U the spectrum undergo deformations which are visible in figures 4.6 and 4.12. They are exhibited by the deviations of the spectrum computed for the real density n_0 (black lines) from the spectrum computed with the TF density – constructed with the values of parameters. We also note that the conical structures are deformed in the first figure – for which $E_{\text{kin}}/E_U \simeq 0.01$ – and destroyed in the second – for which $E_{\text{kin}}/E_U \simeq 0.05$. Besides the Landau levels are still present although they do not

properly superimpose the analytical prediction (4.14) anymore. Note that the value of parameters are different in this case. This is due to the condition on the maximal intensity of strain. In chapter 2 this condition read $\tau L_x/6a < 1$ while in our case it is

$$\eta = \frac{\alpha}{4} \frac{V_0}{U} \frac{L_x}{a} < 1. \quad (4.15)$$

Previously for $U = 10^{-5}$, $V_0 = 3.5 \times 10^{-5}$, $\alpha = 0.1$ and $L_x = 301.5a$, the coefficient reads $\eta = 32.5$ which forces us to change these values. For the present choice of parameters whose corresponding spectrum is shown in figure 4.12, we find $\eta = 0.75$ meaning that the condition is satisfied.

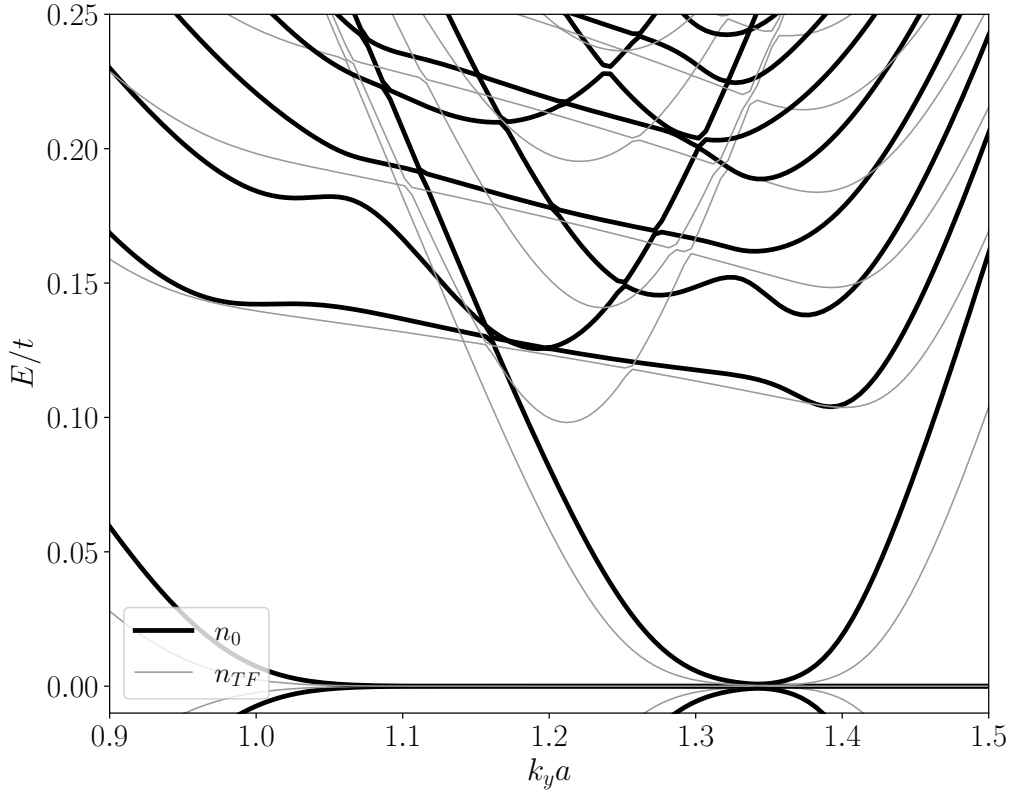


Figure 4.12: Spectrum of \hat{H}_f for $L_x = 301.5a$, $\alpha = 0.1$, $U = 10^{-5}$, $N = 10^5$, $V_0 = 10^{-6}$.

Chapter 5

Conclusions and perspectives

This thesis proposed and analyzed an original strategy to implement strain in cold atom systems, based on recent advances on correlated-hopping experiments such as those used to simulate dynamical gauge fields.

In our proposal, the effect of strain is mediated on the fermions by a second species (bosons) that forms a condensate through a species-dependent hopping. We have established that, combining a harmonic confinement in the Thomas-Fermi approximation together with a specific correlated-hopping effect, provides a suitable strategy to simulate linear strain. We calculated the resulting density profile using the Gross-Pitaevskii equation for the bosons and the corresponding Landau levels for the fermions.

As a continuation of this work, several aspects remain to be investigated. First we need to understand how to generate the correlated-hopping terms using time-dependent Floquet methods. We should further turn our attention to the deviation from the ideal Thomas-Fermi regime and investigate probing methods to observe the Landau levels in experiments. To complete the description we should examine the role of quantum fluctuations (for the bosons) on the Landau levels and the role of coupling between bosons and fermions in order to figure out how they modify the Gross-Pitaevskii results that are formulated in the mean-field approximation.

As a perspective of this project, it would be instructive to compare our results with the method proposed in [34]. We would use realistic experimental parameters for the obtained strain and the corresponding energy gaps of the Landau levels, the type of atoms and size of the clouds in order to clarify the possibility of the experimental realization. Moreover it would be interesting to study the effects of the generated dynamical gauge field (coming from the boson fluctuating density) with similar effects for strain in graphene (coming from phonons). These effects are

not possible in the scheme proposed by Pekker. Furthermore an open question is whether generalizations to other strain profiles, as trigonal strain, are also possible.

Appendix A

Enforcing y -periodicity

Here we show how to obtain the energy dispersion of a ribbon of a honeycomb lattice with zigzag edges on both sides as presented in [37]. For simplicity we consider a semi-infinite ribbon along the x -direction and infinite along the y -direction. We enforce periodic boundary conditions along y and keep the explicit dependence on the l index along the x -direction:

$$\begin{aligned}\hat{a}(l, m) &= \hat{a}(l) e^{im\mathbf{k} \cdot \mathbf{A}_y} \\ \hat{b}(l, m) &= \hat{b}(l) e^{im\mathbf{k} \cdot \mathbf{A}_y}\end{aligned}\tag{A.1}$$

For t_1, t_2 and t_3 arbitrary constants we find $\hat{H} = \bigoplus_{k_y} \hat{H}(k_y)$ with

$$\hat{H}(k_y) = \begin{pmatrix} \dots \\ \hat{b}(l-1) \\ \hat{a}(l) \\ \hat{b}(l) \\ \hat{a}(l+1) \\ \dots \end{pmatrix}^\dagger \begin{pmatrix} \dots & \dots & \dots & \dots \\ \dots & t_2 e^{ik_y \delta_{2,y}} + t_3 e^{ik_y \delta_{3,y}} & \dots & \dots \\ \dots & 0 & t_1 & \dots \\ \dots & t_1 & 0 & \dots \\ \dots & \dots & t_3 e^{-ik_y \delta_{3,y}} + t_2 e^{-ik_y \delta_{2,y}} & \ddots \\ \dots & \dots & \dots & \dots \end{pmatrix} \begin{pmatrix} \dots \\ \hat{b}(l-1) \\ \hat{a}(l) \\ \hat{b}(l) \\ \hat{a}(l+1) \\ \dots \end{pmatrix}\tag{A.2}$$

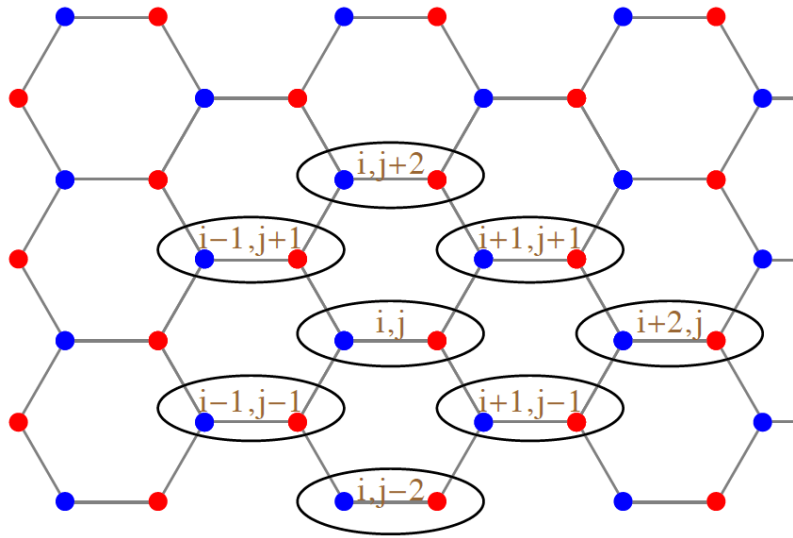


Figure A.1: (Picture taken from reference [37]).

Bibliography

- [1] JEAN DALIBARD. La matière topologique et son exploration avec les gaz quantiques. *Collège de France, chaire Atomes et rayonnement*, URL: http://www.phys.ens.fr/~dalibard/CdF/2018/notes_cours_total.pdf (see pp. 10, 11)
- [2] M ZAHID HASAN and CHARLES L KANE. Colloquium: topological insulators. *Reviews of modern physics*, **82**: 3045, 2010. (see p. 11)
- [3] TOMOKI OZAWA, HANNAH M PRICE, ALBERTO AMO, NATHAN GOLDMAN, MOHAMMAD HAFEZI, LING LU, MIKAEL C RECHTSMAN, DAVID SCHUSTER, JONATHAN SIMON, ODED ZILBERBERG, and IACOPO CARUSOTTO. Topological photonics. *Reviews of modern physics*, **91**: 2019. (see pp. 11, 18)
- [4] C. L KANE and E. J MELE. Size, Shape, and Low Energy Electronic Structure of Carbon Nanotubes. *Physical review letters*, **78**: 1932–1935, 1997. (see pp. 12, 24)
- [5] K. V. KLITZING, G. DORDA, and M. PEPPER. New Method for High-Accuracy Determination of the Fine-Structure Constant Based on Quantized Hall Resistance. *Phys. Rev. Lett.*, **45**: 494–497, 1980. DOI: [10.1103/PhysRevLett.45.494](https://doi.org/10.1103/PhysRevLett.45.494) URL: <https://link.aps.org/doi/10.1103/PhysRevLett.45.494> (see p. 12)
- [6] DAVID TONG. Lectures on the Quantum Hall Effect. 2016. (see pp. 12, 14, 16, 17)
- [7] D. J. THOULESS, M. KOHMOTO, M. P. NIGHTINGALE, and M. DEN NIJS. Quantized Hall Conductance in a Two-Dimensional Periodic Potential. *Phys. Rev. Lett.*, **49**: 405–408, 1982. DOI: [10.1103/PhysRevLett.49.405](https://doi.org/10.1103/PhysRevLett.49.405) URL: <https://link.aps.org/doi/10.1103/PhysRevLett.49.405> (see p. 15)
- [8] W_P SU, JR SCHRIEFFER, and AO J HEEGER. Solitons in polyacetylene. *Physical review letters*, **42**: 1698, 1979. (see p. 18)
- [9] ERIC J MEIER, FANGZHAO ALEX AN, and BRYCE GADWAY. Observation of the topological soliton state in the SuSchriefferHeeger model. *Nature communications*, **7**: 13986–, 2016. (see p. 18)

- [10] DOUGLAS R. HOFSTADTER. Energy levels and wave functions of Bloch electrons in rational and irrational magnetic fields. *Phys. Rev. B*, **14**: 2239–2249, 1976. DOI: [10.1103/PhysRevB.14.2239](https://doi.org/10.1103/PhysRevB.14.2239) URL: <https://link.aps.org/doi/10.1103/PhysRevB.14.2239>(see p. 18)
- [11] DP DiVINCENZO and EJ MELE. Self-consistent effective-mass theory for intralayer screening in graphite intercalation compounds. *Physical Review B*, **29**: 1685, 1984. (see p. 19)
- [12] KOSTYA S NOVOSELOV, ANDRE K GEIM, SERGEI VLADIMIROVICH MOROZOV, DA JIANG, MICHAEL I KATSNELSON, IVA GRIGORIEVA, SVB DUBONOS, FIRSOV, and AA. Two-dimensional gas of massless Dirac fermions in graphene. *nature*, **438**: 197–200, 2005. (see p. 19)
- [13] M. MILICEVIC, T. OZAWA, G. MONTAMBAUX, I. CARUSOTTO, E. GALOPIN, A. LEMAITRE, L. LE GRATIET, I. SAGNES, J. BLOCH, and A. AMO. Orbital Edge States in a Photonic Honeycomb Lattice. *Phys. Rev. Lett.*, **118**: 107403, 2017. DOI: [10.1103/PhysRevLett.118.107403](https://doi.org/10.1103/PhysRevLett.118.107403) URL: <https://link.aps.org/doi/10.1103/PhysRevLett.118.107403>(see p. 19)
- [14] F. D. M HALDANE. Model for a Quantum Hall Effect without Landau Levels: Condensed-Matter Realization of the "Parity Anomaly". *Physical review letters*, **61**: 2015–2018, 1988. (see p. 19)
- [15] MACIEJ LEWENSTEIN, ANNA SANPERA, and VERONICA AHUFINGER. *Ultracold Atoms in Optical Lattices: Simulating quantum many-body systems*. Oxford University Press, 2012. (see pp. 20, 21, 51)
- [16] CLAUDE N COHEN-TANNOUDJI. Nobel Lecture: Manipulating atoms with photons. *Reviews of Modern Physics*, **70**: 707, 1998. (see p. 20)
- [17] J STENGER, S INOUE, A. P CHIKKATUR, D. M STAMPER-KURN, D. E PRITCHARD, and W KETTERLE. Bragg Spectroscopy of a Bose-Einstein Condensate. *Physical review letters*, **82**: 4569–4573, 1999. (see p. 21)
- [18] ANDR ECKARDT, CHRISTOPH WEISS, and MARTIN HOLTHAUS. Superfluid-Insulator Transition in a Periodically Driven Optical Lattice. *Physical review letters*, **95**: 260404–, 2005. (see p. 21)
- [19] ALESSANDRO ZENESINI, HANS LIGNIER, DONATELLA CIAMPINI, OLIVER MORSCH, and ENNIO ARIMONDO. Coherent Control of Dressed Matter Waves. *Physical review letters*, **102**: 100403–, 2009. (see p. 21)
- [20] FREDERIK GRG, MICHAEL MESSER, KILIAN SANDHOLZER, GREGOR JOTZU, RMI DESBUQUOIS, and TILMAN ESSLINGER. Enhancement and sign change of magnetic correlations in a driven quantum many-body system. *Nature (London)*, **553**: 481–485, 2018. (see p. 21)

- [21] N GOLDMAN and J DALIBARD. Periodically Driven Quantum Systems: Effective Hamiltonians and Engineered Gauge Fields. *Physical review. X*, **4**: 031027–, 2014. (see p. 21)
- [22] MARKUS GREINER, OLAF MANDEL, TILMAN ESSLINGER, THEODOR W HNSCH, and IMMANUEL BLOCH. Quantum phase transition from a superfluid to a Mott insulator in a gas of ultracold atoms. *Nature (London)*, **415**: 39–44, 2002. (see p. 22)
- [23] OMJYOTI DUTTA, MARIUSZ GAJDA, PHILIPP HAUKE, MACIEJ LEWENSTEIN, DIRK-SREN LHMANN, BORIS A MALOMED, TOMASZ SOWISKI, and JAKUB ZAKRZEWSKI. Non-standard Hubbard models in optical lattices: a review. *Reports on progress in physics*, **78**: 066001–, 2015. (see p. 22)
- [24] JULIA STASISKA, RAVINDRA W CHHAJLAN, OMJYOTI DUTTA, and MACIEJ LEWENSTEIN. Effects of extended correlated hopping in a bose-bose mixture. 2019. (see p. 22)
- [25] KOS RAPP, XIAOLONG DENG, and LUIS SANTOS. Ultracold Lattice Gases with Periodically Modulated Interactions. *Physical review letters*, **109**: 203005–, 2012. (see p. 22)
- [26] MARCO DI LIBERTO, CHARLES E CREFFIELD, GI JAPARIDZE, and C MORAIS SMITH. Quantum simulation of correlated-hopping models with fermions in optical lattices. *Physical Review A*, **89**: 013624, 2014. (see pp. 22, 73)
- [27] JEAN DALIBARD, FABRICE GERBIER, GEDIMINAS JUZELINAS, and PATRIK HBERG. Colloquium : Artificial gauge potentials for neutral atoms. *Reviews of modern physics*, **83**: 1523–1543, 2011. (see p. 22)
- [28] N GOLDMAN, G JUZELINAS, P HBERG, and I B SPIELMAN. Light-induced gauge fields for ultracold atoms. *Reports on progress in physics*, **77**: 126401–, 2014. (see p. 22)
- [29] MONIKA AIDELSBURGER, SYLVAIN NASCIMBENE, and NATHAN GOLDMAN. Artificial gauge fields in materials and engineered systems. *Comptes rendus. Physique*, **19**: 394–432, 2018. (see p. 22)
- [30] M AIDELSBURGER, M ATALA, M LOHSE, J. T BARREIRO, B PAREDES, and I BLOCH. Realization of the Hofstadter Hamiltonian with Ultracold Atoms in Optical Lattices. *Physical review letters*, **111**: 185301–, 2013. (see p. 22)
- [31] GREGOR JOTZU, MICHAEL MESSER, RMI DESBUQUOIS, MARTIN LEBRAT, THOMAS UEHLINGER, DANIEL GREIF, and TILMAN ESSLINGER. Experimental realization of the topological Haldane model with ultracold fermions. *Nature (London)*, **515**: 237–240, 2014. (see p. 22)

- [32] DANIEL LEYKAM, M.C RECHTSMAN, and Y.D CHONG. Anomalous Topological Phases and Unpaired Dirac Cones in Photonic Floquet Topological Insulators. *Physical review letters*, **117**: 013902–, 2016. (see p. 22)
- [33] MIKAEL C RECHTSMAN, JULIA M ZEUNER, ANDREAS TNNERMANN, STEFAN NOLTE, MORDECHAI SEGEV, and ALEXANDER SZAMEIT. Strain-induced pseudomagnetic field and photonic Landau levels in dielectric structures. *Nature photonics*, **7**: 153–158, 2012. (see pp. 23, 42)
- [34] BINBIN TIAN, MANUEL ENDRES, and DAVID PEKKER. Landau Levels in Strained Optical Lattices. *arXiv.org*, **115**: 2015. URL: <http://search.proquest.com/docview/2084107692/>(see pp. 23, 44, 73, 92)
- [35] M GOERBIG. Electronic Properties of Graphene in a Strong Magnetic Field. *arXiv.org*, **83**: 2011. URL: <http://search.proquest.com/docview/2087008310/>(see pp. 28, 32)
- [36] B. ANDREI BERNEVIG and TAYLOR L. HUGHES. *Topological Insulators and Topological Superconductors*. STU - Student edition Princeton University Press, 2013. URL: <http://www.jstor.org/stable/j.ctt19cc2gc> (see pp. 29–32)
- [37] GRAZIA SALERNO. *Artificial gauge fields in photonics and mechanical systems*. PhD thesis. University of Trento, 2016. (see pp. 31, 32, 34, 35, 94, 95)
- [38] GRAZIA SALERNO, TOMOKI OZAWA, HANNAH PRICE, and IACOPO CARUSOTTO. How to directly observe Landau levels in driven-dissipative strained honeycomb lattices. *arXiv.org*, **2**: 2015. URL: <http://search.proquest.com/docview/2083513933/>(see pp. 37, 39, 40)
- [39] GRAZIA SALERNO, TOMOKI OZAWA, HANNAH PRICE, and IACOPO CARUSOTTO. Propagating edge states in strained honeycomb lattices. *arXiv.org*, **95**: 2017. URL: <http://search.proquest.com/docview/2075933174/>(see pp. 38, 39, 41)
- [40] LEV PITAEVSKII and SANDRO STRINGARI. *Bose-Einstein condensation and superfluidity*. vol. 164 Oxford University Press, 2016. (see pp. 47, 50–52, 54, 55, 60)
- [41] ALLAN GRIFFIN, DAVID W SNOKE, and SANDRO STRINGARI. *Bose-einstein condensation*. Cambridge University Press, 1996. (see p. 55)
- [42] CHRISTOPHER J PETHICK and HENRIK SMITH. *Bose-Einstein condensation in dilute gases*. Cambridge university press, 2008. (see p. 55)
- [43] F DALFOVO, S GIORGINI, L PITAEVSKII, and S STRINGARI. Theory of Bose-Einstein condensation in trapped gases. *arXiv.org*, **71**: 1998. URL: <http://search.proquest.com/docview/2088217029/>(see p. 57)

- [44] A. MINGUZZI, S. SUCCI, F. TOSCHI, M.P. TOSI, and P. VIGNOLO. Numerical methods for atomic quantum gases with applications to BoseEinstein condensates and to ultracold fermions. *Physics Reports*, **395**: 223 –355, 2004. DOI: <https://doi.org/10.1016/j.physrep.2004.02.001> URL: <http://www.sciencedirect.com/science/article/pii/S0370157304001097> (see p. 64)
- [45] TAO WANG, SHIJIE HU, SEBASTIAN EGGERT, MICHAEL FLEISCHHAUER, AXEL PELSTER, and XUE-FENG ZHANG. Floquet-induced superfluidity with periodically modulated interactions of two-species hardcore bosons in a one-dimensional optical lattice. *Physical Review Research*, **2**: 2020. (see p. 73)
- [46] JULIA STASISKA, RAVINDRA W CHHAJLANI, OMJYOTI DUTTA, and MACIEJ LEWENSTEIN. Effects of extended correlated hopping in a bose-bose mixture. 2019. (see p. 73)
- [47] OLE JRGENSEN, FLORIAN MEINERT, MANFRED J MARK, HANNS-CHRISTOPH NGERL, and DIRK-SREN LHMANN. Observation of density-induced tunneling. *Physical Review Letters*, **113**: 193003–, 2014. (see p. 73)